# COMPUTATIONAL TECHNIQUES FOR THE DIRECT DETECTION OF DARK MATTER

by
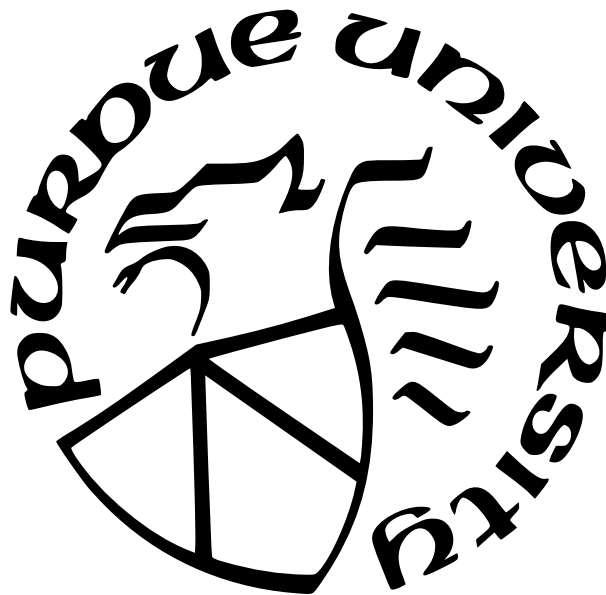
**Juehang Qin**

**A Dissertation**

*Submitted to the Faculty of Purdue University*

*In Partial Fulfillment of the Requirements for the degree of*

**Doctor of Philosophy**

Department of Physics and Astronomy

West Lafayette, Indiana

August 2023

# THE PURDUE UNIVERSITY GRADUATE SCHOOL
## STATEMENT OF COMMITTEE APPROVAL

**Dr. Rafael Lang, Chair**

Department of Physics and Astronomy

**Dr. David Koltick**

Department of Physics and Astronomy

**Dr. Nima Lashkari**

Department of Physics and Astronomy

**Dr. Daniel Carney**

Lawrence Berkeley National Laboratory

**Approved by:**

Dr. Gabor Csathy

*This work is dedicated to the love of my life, Rose, who has supported me unwaveringly through my graduate studies, and to my parents, who have always cultivated my love for science.*

# ACKNOWLEDGMENTS

# TABLE OF CONTENTS

# LIST OF TABLES

# LIST OF FIGURES

9

13

# ABSTRACT

Dark matter makes up a vast majority of the matter in the universe, however, the composition of dark matter is unknown. One approach to uncover the composition of dark matter is via the direct detection of dark matter. This thesis focuses on the use of computational techniques to enhance or enable the direct detection of dark matter by the XENON experiment and the Windchime project.

First, a software veto for radon chain backgrounds using measurements of the convective motion in XENON1T is detailed and demonstrated. It is shown that this can reduce the radon chain background in the XENON1T and XENONnT detectors, and with potential for improved performance in larger detectors with reduced convection. The design and operation of a $^{88}$Y-Be photo-neutron source is then discussed. It is shown that in the calibration data collected there is a significant population of neutron events that can be used to calibrate the detector response. Following that is a discussion of the methods to conduct analysis and make sensitivity projections for the Windchime project. A semi-analytical method for sensitivity projections that does not require a full simulation of the sensor array is shown, and both Bayesian and frequentist approaches to track-finding in sensor arrays are demonstrated. The latter includes an estimate of the look-elsewhere effect in such a dark matter search. This leads to an exploration of the use of Gaussian random fields for the estimation of the look-elsewhere effect, wherein it is shown that Gaussian random fields can be sampled quickly to compute the look-elsewhere effect corrections.

# 1. INTRODUCTION

*"The only way of discovering the limits of the possible is to venture a little way past them into the impossible."* - Arthur C. Clarke [1]

Dark matter is one of the greatest scientific mysteries of our time. Most of the mass in the universe is dark matter–and yet, the nature of dark matter is unknown [2]. The primary scientific goal of this thesis is to shed light on the nature of dark matter via direct detection experiments. Thus far, there has not been an unambiguous detection of a dark matter signal in direct detection experiments [3]. The work presented in this thesis therefore aims to push the boundaries of dark matter searches–to cover a wider range of models, and to increase the sensitivity of dark matter searches to lower cross sections. This is done with a focus on computational techniques, and will be expanded upon in detail in the following chapters.

In this introductory chapter, I briefly cover relevant background information regarding dark matter and the direct detection experiments that form the basis of this work. Following this, in chapter 2, I discuss my work regarding the use of algorithms to reduce radioactive backgrounds in liquid noble element detectors such as XENON1T. In chapter 3, I discuss the design and operation of a $^{88}$Y/Be photo-neutron calibration source for XENONnT. In chapter 4, I discuss data analysis and sensitivity projection methods developed for the Windchime project. In chapter 5, I discuss the use of Gaussian random fields to model the look-elsewhere effect efficiently. Finally, chapter 6 presents a conclusion to this thesis.

## 1.1 Dark matter

### 1.1.1 Evidence for Dark Matter

Dark matter accounts for 84.4% of the total matter density in the universe, and is a generally accepted in modern cosmology with many independent pieces of supporting evidence [2, 4–6]. This includes signatures from the early universe such as Big Bang nucleosynthesis, the cosmic microwave background, and evidence from later times, such as structure formation, galaxy cluster mergers, and galaxy rotation curves. These pieces of

evidence are independent and range from the largest scales to the universe to the scale of small galaxies. In this section, I will briefly overview some of the evidence for dark matter.

**Big Bang Nucleosynthesis**

In the early universe, protons and neutrons were in thermal equilibrium; however, at approximately $1\,\mathrm{s}$, the temperature of the universe dropped enough that neutrons and protons can no longer freely convert between each other. At this time, the neutron-proton ratio would be approximately $n/p \approx 1/6$ [2]. Shortly thereafter, the temperature of the universe drops low enough that nuclei can form without being immediately dissociated by photons. Because neutrons are allowed to beta decay, by this time, the proton-neutron ratio is $n/p \approx 1/7$. Almost all of the neutrons end up as part of $^4$He nuclei because it is the most stable light element; thus, the primordial mass fraction of $^4$He can be estimated by simply dividing the number of neutrons times two by the total number of nucleons [2]:

$$Y_p = \frac{2(n/p)}{1 + n/p} \approx 0.25 \tag{1.1}$$

This process and hence the abundance of light elements in the universe is sensitive to the baryon density in the early universe [2, 7]. Thus, while the existence of dark matter cannot directly be inferred from Big Bang nucleosynthesis, it is possible to determine the baryon density in the universe based on measurements of the light element abundances, such as the $^4$He primordial mass fraction. When combined with other measurements of cosmological parameters, such as from the cosmic microwave background, such constraints of the baryon density serve as both independent verification of the models, and as evidence that there is not enough baryonic matter to account for the matter density in the universe. It can be seen in Figure 1.1 that the baryon density inferred from Big Bang nucleosynthesis is in agreement with that from the cosmic microwave background, which is introduced next.
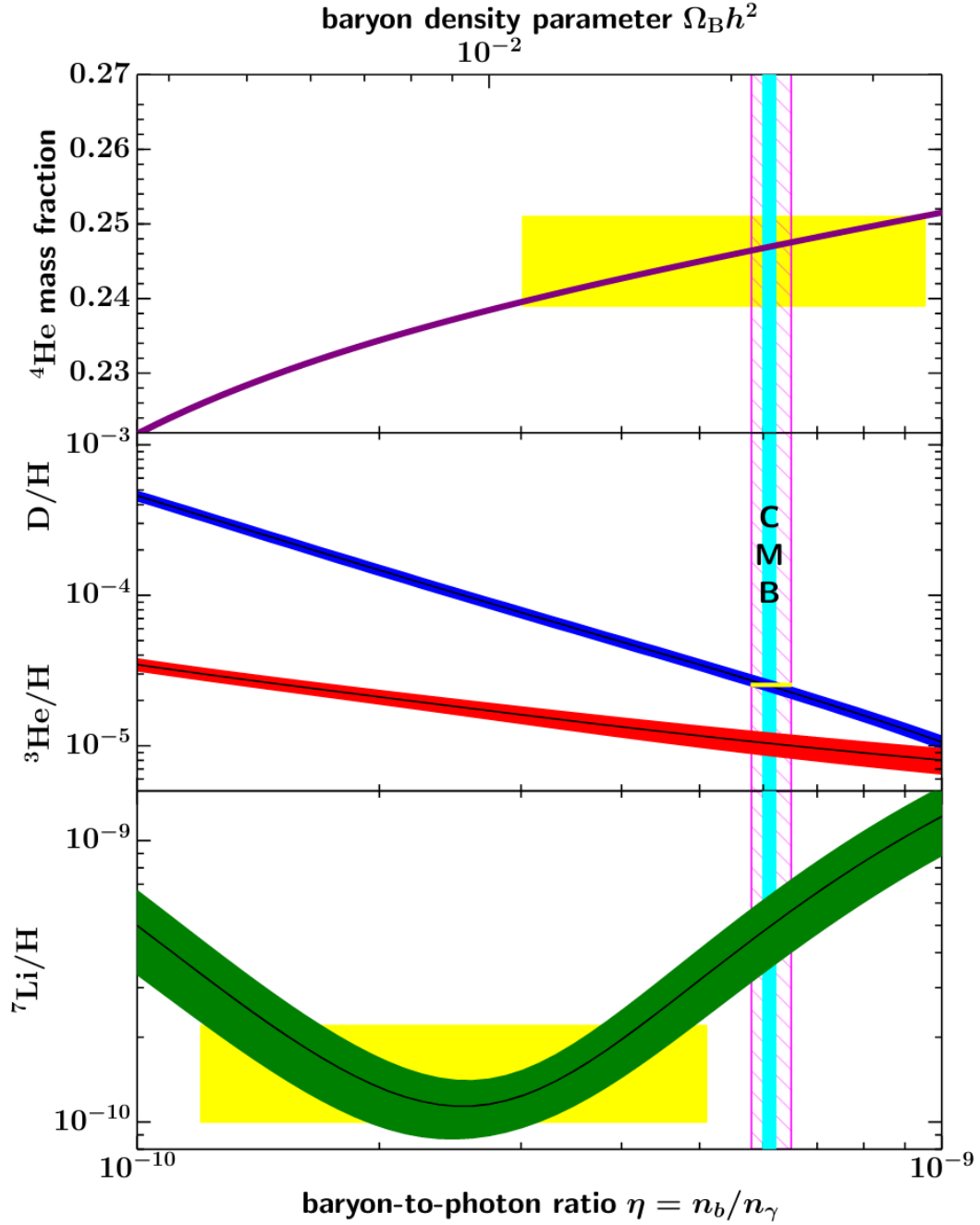
**Figure 1.1.** Abundances of $^4$He (purple), D (blue), $^3$He (red), and $^7$Li (green) as a fraction of $^1$H abundance. The 95% CL range of the model prediction is shown in coloured bands, and the observed abundances are indicated by yellow boxes. The baryon density as measured via the cosmic microwave background (CMB) is indicated by the cyan vertical band, whereas the BBN measurement using D and $^4$He is indicated by the purple hatched vertical band. Reproduced from [2].

## The Cosmic Microwave Background

The cosmic microwave background is a key piece of evidence for dark matter. When the universe was approximately 300,000 years old, the universe cooled enough for free electrons to be captured by atomic nuclei to form neutral atoms, in a process called recombination [8]. This caused the previously opaque universe to become transparent to light; thus, the cosmic background radiation from that recombination era is still visible today. This radiation, however, is now red-shifted to the microwave range, with a $2.7\,\mathrm{K}$ black-body spectrum [4]. While the cosmic microwave background radiation appears to be a nearly perfect black-body spectrum, there are small fluctuations on the order of $\Delta T/T \sim 10^{-5}$ caused by matter density fluctuations in the early universe at the time of recombination [2, 8]. Specifically, there are peaks in the power spectrum of the cosmic microwave background radiation caused by acoustic oscillations in the early universe. The amplitude and position of these peaks are sensitive to cosmological parameters, including the total matter density and the baryon density of the universe [8]. A measurement of these fluctuations in the cosmic microwave background radiation by the Planck Collaboration [9] can be seen in Figure 1.2.

The best fit in Figure 1.2 uses the $\Lambda$CDM model, otherwise known as the standard model of cosmology. It corresponds to a universe dominated by dark energy ($\Lambda$), cold dark matter (CDM), and baryonic matter [2, 4]. The dark energy, dark matter, and baryonic matter densities corresponding to Figure 1.2 are $\Omega_\Lambda \approx 0.68$, $\Omega_\chi \approx 0.26$, and $\Omega_b \approx 0.05$, indicating that $\approx 84\%$ of the matter in the universe is dark matter.
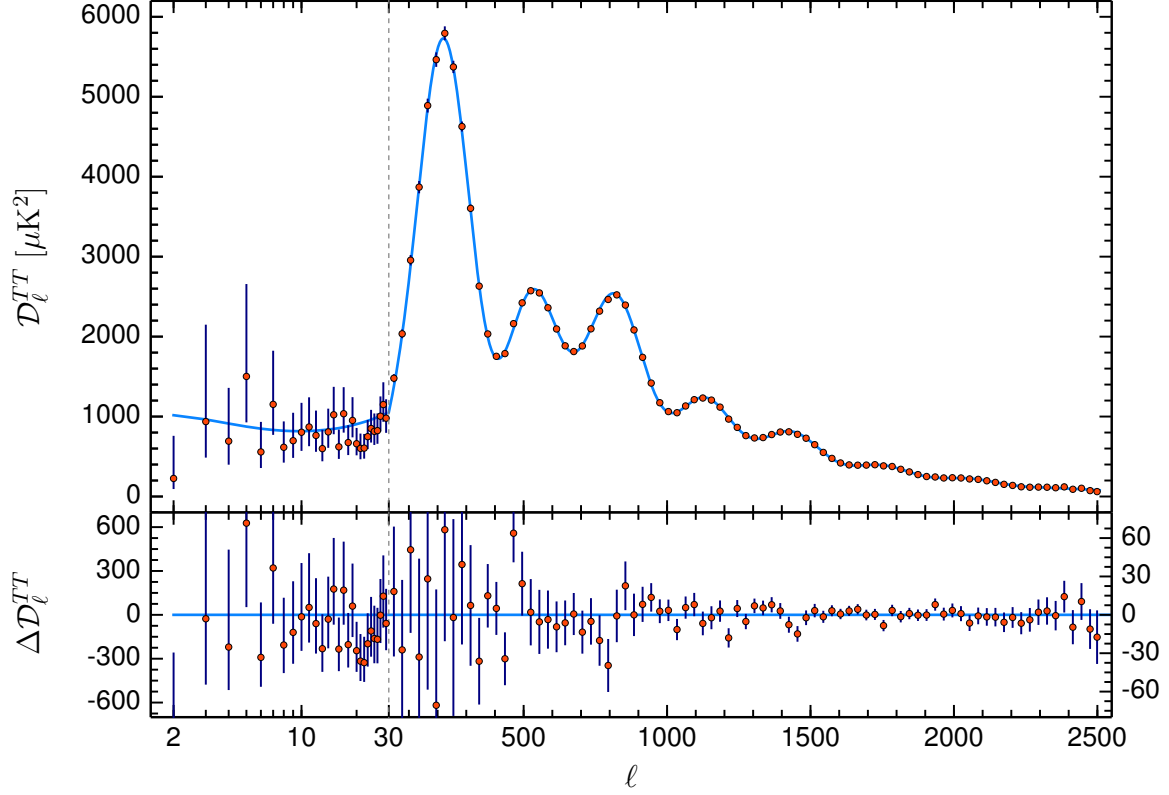
**Figure 1.2.** The power spectrum of the cosmic microwave background as measured by Planck Collaboration. The *TT* superscript in the y-axis refers to the fact that this is a power spectrum of temperature fluctuations. Different algorithms are used to compute the power spectrum for low and high values of the multipole $\ell$, with the $\ell = 30$ threshold for switching between the two algorithms indicated by the dotted vertical line. Reproduced from [4].

**Large Scale Structure of the Universe**

Density fluctuations in the early universe also impact the formation of structure and hence the distribution of matter in the universe [2]. Thus, we can compare observations of the matter distribution in the universe with models of structure formation based on $\Lambda$CDM to determine the cosmological parameters. This has been done by the Dark Energy Survey [10], leading to the following measurement of the cosmological matter density: $\Omega_m \approx 0.27$, agreeing with measurements by Planck with overlapping 95% confidence intervals. When combined with the constraints on baryonic matter density from Big Bang nucleosynthesis, this demonstrates that there is significantly more matter in the universe than there is baryonic matter.

The same acoustic oscillations that leave imprints in the cosmic microwave background radiation can also be observed in the matter power spectrum and the two-point correlation of galaxies. This is because the power spectrum and two-point correlation function forms a Fourier transform pair, a fact that serendipitously will be discussed again in a completely different context in chapter 5. The principal effect of acoustic oscillations is to create an acoustic peak in the correlation function at a specific distance scale, known as the sound horizon. This sound horizon is predicted by $\Lambda$CDM to be $r_s \approx 150\,\mathrm{Mpc}$; thus, measurements of this sound horizon can serve as both a cosmological distance ladder and a test of $\Lambda$CDM. This was measured by the Sloan Digital Sky Survey, and was found to agree with $\Lambda$CDM predictions made using cosmological parameters inferred from the cosmic microwave background [6].

**The Bullet Cluster**

At smaller scales than we have discussed thus far, cluster 1E0657-558, otherwise known as the Bullet Cluster, provides another key piece of evidence for the existence of dark matter. The Bullet Cluster, shown in Figure 1.3, is made up of two colliding galaxy clusters.

X-ray: NASA/CXC/CfA/ M.Markevitch et al.;
Lensing Map: NASA/STScI; ESO WFI; Magellan/U.Arizona/ D.Clowe et al.
Optical: NASA/STScI; Magellan/U.Arizona/D.Clowe et al.

**Figure 1.3.** The bullet cluster in visible light (true colour galaxies), and X-ray (pink), with a gravitational lensing map (blue) indicating the matter distribution. Reproduced from [11]. X-ray data from [12], optical and lensing data from [13].

As the clusters collided, the galaxies themselves largely did not interact due to the large distances between galaxies. The X-ray emitting plasma (shown in pink in Figure 1.3), however, behaves like a fluid, displaying a bow shock on the right side and being slowed down by interactions compared to the galaxies. In these galaxy clusters, the baryonic mass is dominated by X-ray emitting plasma as opposed to galaxies [13]; as such, without the existence of dark matter, one would expect the X-ray emission to line up with the matter distribution obtained via gravitational lensing shown in blue in Figure 1.3. However, we can see that this is not the case, indicating that the matter distribution is dominated by mass that we cannot yet detect–dark matter.

**Galaxy Rotation Curves**

Galaxy rotation curves are another key piece of evidence for the existence of dark matter. In a spiral galaxy, most of the luminous matter is concentrated in the centre. The orbital speed of matter around a central mass can be derived within the framework of classical mechanics as such:

$$
\frac{v^2}{r} = G\frac{M(r)}{r^2}
$$
$$
v = \sqrt{G\frac{M(r)}{r}}
\tag{1.2}
$$

where $M(r)$ is the amount of mass contained within radius $r$. Thus, where the central mass dominates and $M(r) \approx$ constant, we would expect the velocity of stars orbiting in the disc to decrease with increasing distance from the centre as $v \propto r^{-1/2}$ [14]. Observations of spiral galaxies, including our own, however, show a much flatter rotation curve [15, 16]. An example of this can be seen in Figure 1.4, where that the rotation curve of M33 is best fit by a model with a dominant dark matter halo. Such rotation curves have been observed in large surveys of galaxies [14, 17, 18], and is consistent with the existence of dark matter.
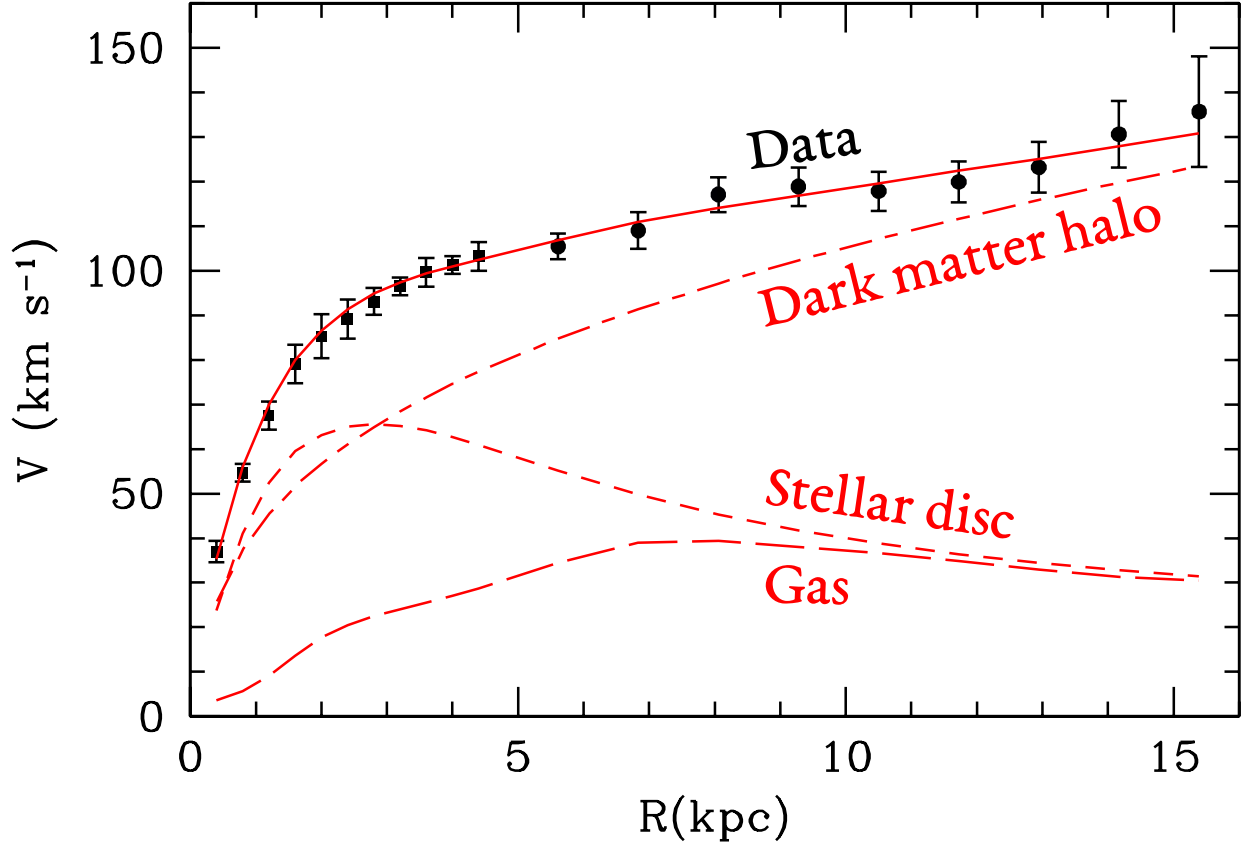
**Figure 1.4.** The rotation curve of M33. The best-fit mass model is indicated by the continuous red line, with individual components indicated by red dashed and dash-dotted lines. Parameters representing the stellar disc contribution and the shape of the dark matter distribution are used to fit the data. Reproduced from [19], with added labels for clarity.

It should be noted that galaxy rotation curves can also be fit using theories of modified gravity such as Modified Newtonian Dynamics using a relation between the Newtonian acceleration and the observed acceleration, known as a Radial Acceleration Relation. However, these models have not been shown to accommodate different galaxies with a simultaneous fit [20], or other pieces of evidence for dark matter highlighted in this section [2, 21].

### 1.1.2 Models of Dark Matter

The two dark matter candidates most relevant in this thesis are Weakly Interacting Massive Particles (WIMPs) and ultra-heavy dark matter. These two models are the primary focus of the XENON Experiment (see section 1.2) and the Windchime Project (see section 1.3), respectively.

**Weakly Interacting Massive Particles**

Freeze-out refers to the process where constituents of the universe decouples from the thermal bath representing the rest of the universe as the matter density drops. This happens as the rate of processes that change the particle species, such as annihilation ($\chi\bar{\chi} \rightarrow \gamma\gamma$), drops below the Hubble rate, which parameterises the expansion of the universe [2, 14]. Freeze-out is discussed in subsection 1.1.1 in the context of light elements and CMB photons, and can similarly be considered as a formation mechanism for dark matter.

With this freeze-out mechanism, the relation between dark matter density and cross section is given by [14, 22]:

$$\Omega_\chi \sim \frac{10^{-25}\,\mathrm{cm^3/s}}{\langle \sigma v \rangle} \tag{1.3}$$

where $\Omega_\chi$ is the dark matter density, $\sigma$ is the average dark matter annihilation cross section, and $v$ is the dark matter velocity. The $\chi$ subscript is used to denote the WIMP. The numerator in this relation does depend on mass logarithmically, and thus the order-of-magnitude estimate holds from $m_\chi \sim 1\,\mathrm{GeV}$ to $m_\chi \sim 1\,\mathrm{TeV}$[14, 22]. For typical velocities of $0.1c$, we can obtain a cross section of $\sigma \sim 10^{-35}\,\mathrm{cm^2}$ which is around the electroweak symmetry breaking scale [22]. This remarkable coincidence is known as the WIMP miracle, and has led WIMPs being one of the most favoured dark matter candidates.

**Ultra-heavy Dark Matter**

The goal of Windchime is to search for dark matter with masses of around the Planck mass ($m_\chi \approx 10^{19}\,\mathrm{GeV}$). The reason for the focus on the Planck mass is a confluence of theoretical motivations and experimental considerations. The mass range around the Planck mass is a natural region of parameter space to search for dark matter, as new physics is expected at that mass scale. More concretely, there are many theoretical models that predict dark matter particles in this mass range [23–26]. An overview of these can be found in [25].

Experimentally, the Planck mass is approximately an upper mass limit for dark matter that can be probed by direct detection experiments, and coincidentally also approximately the lower limit for gravitational detection of dark matter [23]. The former is due to the fact that given the known dark matter density [2], the flux of dark matter particles is approximately $(m_{Pl}/m_\chi)\,\mathrm{yr}^{-1}\,\mathrm{m}^{-2}$; thus, the flux of dark matter that is far heavier than the Planck mass would be too low for metre-scale direct detection experiments. The latter is due the fact that the gravitational attraction from a Planck mass dark matter particle is enough to rise above the thermal noise floor of large accelerometer arrays under certain circumstances [23].

### 1.1.3 Direct Detection of Dark Matter

In direct detection experiments, we attempt to detect galactic dark matter passing through our lab. Because galactic dark matter has to be gravitationally bound with an escape velocity of $v_{esc} = 528^{+24}_{-25}\,\mathrm{km/s}$, it is non-relativistic[2]. Because of this, the recoil energy between WIMP and detector nuclei tends to be in the tens-of-keV scale or smaller [2]. This highlights the importance of reducing systematic uncertainties near detector thresholds for WIMP experiments, such as the calibration discussed in chapter 3.

In direct detection experiments, there can exist events originating from processes unrelated to dark matter, such as cosmic rays or radiation. These events, termed backgrounds, mean that it is often not possible to attribute individual events to dark matter. There are thus two primary signatures of dark matter in direct detection experiments: an event excess above background, and an annual modulation signal. This annual modulation is due to the Earth's motion in the solar system going with the motion of the Sun in the Milky Way for part of

the year, and against for other parts of the year. This motion increases or decreases the flux of Dark Matter particles, respectively. However, due to the fact that the Earth's orbital velocity in the solar system is much lower than the Sun's orbital velocity in the Milky Way, the amplitude of the annual modulation is only about 5% [2]. Thus, in both XENON and Windchime, we opt to focus on looking for an event excess above background. To maximise the sensitivity of such an experiment, it is important to minimise the background, as a signal must rise above the statistical fluctuations in the background expectation to result in a statistically significant detection.

## 1.2   The XENON Experiment

The XENON1T experiment, located in Laboratori Nazionali del Gran Sasso (LNGS) underground laboratory in Italy, uses a dual-phase time-projection chamber (TPC) to search for dark matter. Liquid xenon is used as the active target [27]. Some of the strongest limits on the interaction cross section of dark matter and normal matter have come from WIMP searches with liquid xenon TPCs [28–30]. In addition, XENON1T, XENONnT, and other liquid xenon TPCs are sensitive to various other physics channels, such as searches for neutrinoless double-beta decay ($0\nu\beta\beta$) [31–33], measurements of double electron capture in $^{124}$Xe [34], solar axions, non-standard neutrino interactions, and bosonic dark matter [35, 36].

The siting of XENON1T underground in LNGS provides a 3600 m water-equivalent overburden [27, 37], greatly reducing backgrounds from cosmic-ray muons. The XENON1T TPC is housed in a double-walled vacuum cryostat, which is surrounded by a 740 m$^3$ water Cherenkov muon veto. This allows for active detection and veto of muons and muon-induced backgrounds, further reducing the cosmogenic background rate. A schematic of the XENON1T TPC is shown in Fig 1.5.
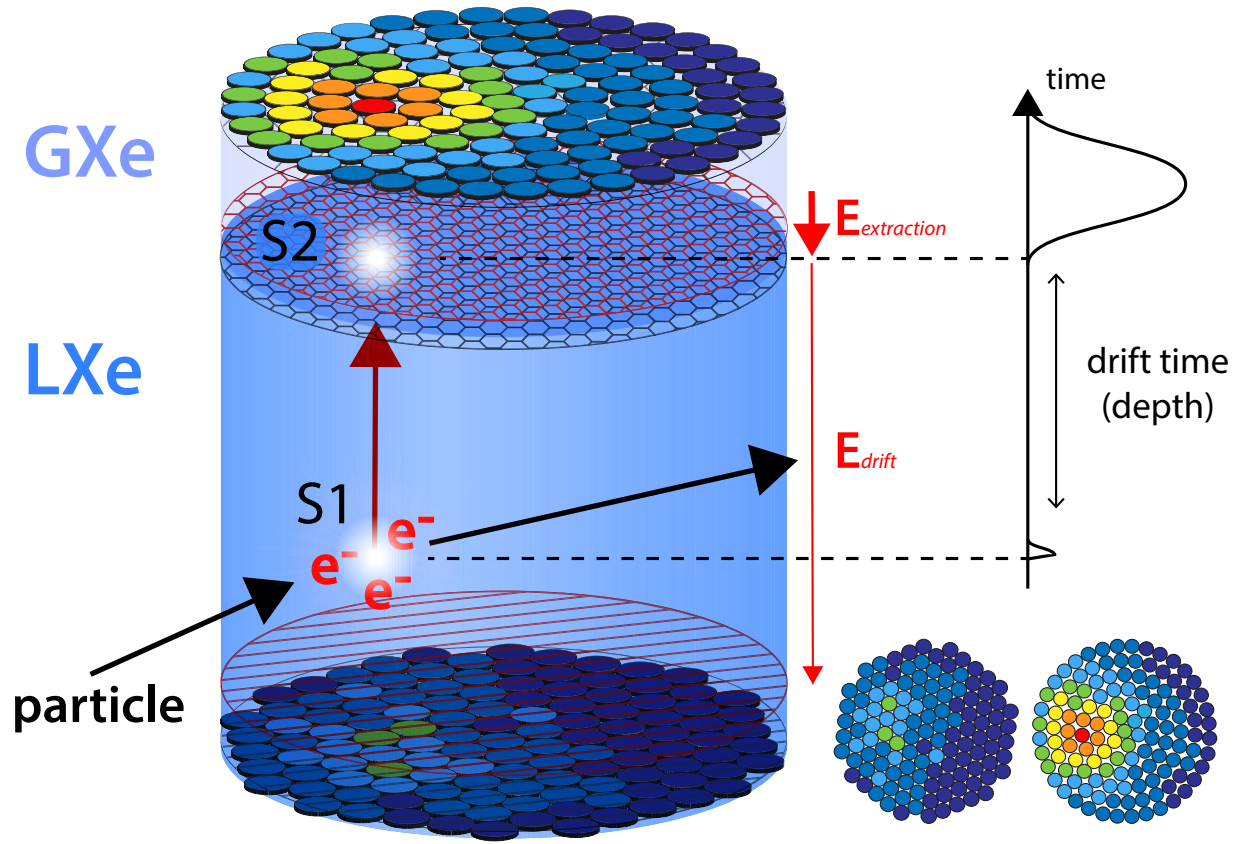
**Figure 1.5.** Schematic of the XENON1T TPC. When a particle enters the TPC and scatters, there is a scintillation signal produced, in addition to free electrons. The electrons are drifted up with an electric field and extracted into the xenon gas, where they are accelerated and produce a second signal when those electrons scatter off gaseous xenon atoms. Image credit: Lutz Althüser [38].

In XENON1T, there are two photomultiplier tube (PMT) arrays on the top and bottom. Electric fields are produced in the TPC using five electrodes. The extraction field is produced using the anode, near the top of the TPC in the gaseous xenon, and the gate, just below the liquid level, whereas the drift field is produced using the gate and the cathode, near the bottom of the TPC. In addition, there are two screening electrodes between the aforementioned three electrodes and the top and bottom PMT arrays to minimise the field near the PMTs [27]. The TPC diameter is 96 cm and the distance between the cathode and gate is 97 cm, resulting in a total active target mass of 2.0 tonnes. More details regarding the design of the XENON1T experiment can be found in [27].

The XENONnT experiment is an in-place upgrade of XENON1T. The TPC diameter and the separation between is increased to 1.3 m, and the distance between the cathode and gate is increased to 1.5 m, resulting in an increased active target mass of 5.9 tonnes. The muon veto itself is unchanged from XENON1T. However, there is now a neutron veto surrounding the main cryostat containing the TPC, which is optically separated from the muon veto. The neutron veto aims to reduce the radiogenic neutron background by detecting neutrons which scatter in the TPC volume and are then captured in the neutron veto [39]. More details regarding the design of the XENONnT experiment can be found in [39].

Xenon is a scintillator [40]; as such, when a particle enters the detector and scatters on a xenon atom, photons would be emitted, and we will observe a prompt scintillation signal, referred to as the S1 signal. In addition, some electrons would be freed [40]. If these electrons do not quickly re-combine with the atoms they were freed from before being carried away by Brownian motion or the drift field, they can be drifted up by the drift field. Once the electrons are above the gate electrode, the stronger extraction field extracts the electrons into the gaseous xenon and accelerates them. The accelerated electrons then generate proportional scintillation in gaseous xenon atoms, allowing the ionisation signal, known as the S2, to be detected by the PMTs [27]. There is three-dimensional position reconstruction for each event, with x/y positions being inferred using the PMT light patterns, while z positions are determined by the time between S1 and S2 signals. The position reconstruction allows for greater background rejection by excluding events near the surface of the detector, which are more likely to be due to radioactive backgrounds, from analysis. The ratio between S1 and

S2s can be used to discriminate between electronic recoil (ER) events, referring to interactions where more kinetic energy is deposited into electrons such as charged particles, gamma rays, and nuclear recoil (NR) events, referring to events where more kinetic energy is deposited into the nucleus typically by neutral particles, such as neutrons and WIMPs.

## 1.3   The Windchime Project

The Windchime project aims to use mechanical quantum-limited accelerometers to detect dark matter via the gravitational coupling alone [23, 41]. While the gravitational force is extremely weak, it has been shown theoretically that this might be possible with a large array of sensors [23]. The goal of this experiment is to detect heavy dark matter around the Planck mass using a large array of mechanical sensors [41]. For reference, the Planck mass is $22\,\mu$g–approximately $1/10^{\text{th}}$ the mass of a fruit fly [42]. At this mass, detection of momentum transferred due to gravitational interactions between dark matter particles and the test mass of sensors is still extremely challenging, but not necessarily impossible! In such an experiment, dark matter couples via a long-range force, such as gravity, producing tracks in a sensor array, and the signal on an individual sensor would look like an extremely fast impulse. A schematic of such an array with a dark matter track is shown in Figure 1.6.
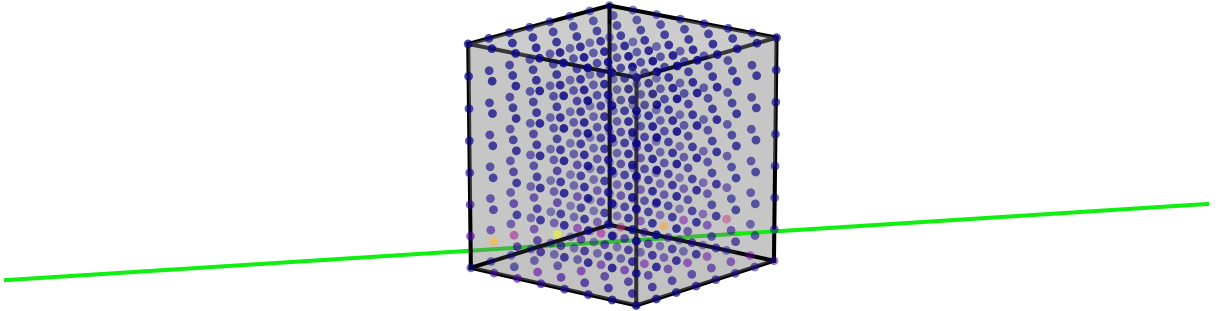


**Figure 1.6.** Plot of an example array, with sensors represented by coloured circles. The strength of an acceleration signal is indicated by the sensor colour. An example track going through the array is shown in green.

In a track through an array with sensor separation $\delta L$, one would expect the closest approach between the track and sensors in the array that are along the track to be the $\sim \delta L$ [23]. In the lab frame, the expected speed distribution of dark matter is expected to peak at $\approx 300\,\text{km/s}$ [43]. For a $\delta L \approx 1\,\text{cm}$ array, this would indicate that the typical time spanned by an impulse is $\sim 1\,\text{cm}/(300\,\text{km/s}) \approx 30\,\text{ns}$.

The reason for needing a sensor array is two-fold. First, due to how weak the gravitational coupling is, it is expected that any signal would be extremely hard to detect. With a large array of $N^3$ sensors, a track would pass by $\sim N$ sensors. If the noise is largely uncorrelated, as is the case for thermal or quantum noise, this would confer a $\sim \sqrt{N}$ improvement in the signal-to-noise ratio (SNR). Second, on an individual sensor, background processes such as cosmic rays or radioactive decays of atoms in a sensor test mass could mimic the fast impulses that we hope to detect. These backgrounds, however, are expected to be uncorrelated between sensors, thus searching for a track would provide effective rejection of many such backgrounds [23].

# 2. OFFLINE TAGGING OF RADON-INDUCED BACKGROUNDS IN LIQUID NOBLE ELEMENT DETECTORS

*This work is under internal review by the XENON Collaboration, and is intended to be published shortly after the submission of this thesis.*

## 2.1 Introduction

Liquid xenon time projection chambers (TPCs) such as XENON1T [27], XENONnT [39], and LZ [44] are constructed with the primary goal of searching for dark matter in the form of weakly-interacting massive particles (WIMPs) [27, 29]. These TPCs as well as the dedicated EXO TPC also search for neutrinoless double-beta decay ($0\nu\beta\beta$) [31–33]. Other physics channels include measurements of double electron capture in $^{124}$Xe [34], solar axions, non-standard neutrino interactions, and bosonic dark matter [35, 36].

Achieving low levels of radioactive backgrounds is critical to the aforementioned physics channels. In xenon-based dark matter experiments, $^{222}$Rn contamination is a major source of backgrounds in the ER channel, and is also important to the nuclear-recoil (NR) channel due to imperfect ER/NR discrimination [27, 39, 44–46]. This is because $^{222}$Rn is produced from the emanation of $^{226}$Ra which is present at low levels in almost all materials [47]. In addition, $^{222}$Rn is miscible with xenon, and the half-life of $t_{1/2} \approx 3.8$ days [48] allows it to mix throughout the detector. The isotope in the $^{222}$Rn decay chain that decays to produce the relevant low-energy background is $^{214}$Pb, see Figure 2.1. Because of this, substantial efforts address this background in hardware [47, 49–53]. The work described in this chapter aims to compliment such hardware-based methods to further reduce radon-induced backgrounds using offline analysis.

Efforts to tag $^{214}$Pb events in XENON1T based on other events in the same decay chain require a measurement of the convection velocity field. This in contrast to solid-state detectors, such as DAMIC [54], where decays from the same decay chain are expected to be spatially coincident even when events are separated by tens of days [55]. The measurement of convection in XENON1T and properties of the velocity field are detailed in section 2.2. The

algorithm to track isotopes along the measured velocity field and thus veto $^{214}$Pb events is detailed in section 2.3. Results, including demonstrations of the technique on XENON1T data, projections to XENONnT and future liquid xenon detectors, and application to cosmogenic $^{137}$Xe which is a background for the search for neutrinoless double-beta decay ($0\nu\beta\beta$), are discussed in section 2.4. Finally, the conclusion is presented in section 2.5.

### 2.1.1 The $^{222}$Rn Decay Chain

The decay chain of $^{222}$Rn is shown in Figure 2.1. $^{214}$Pb is responsible for the low-energy ER background. This is because the beta spectrum of $^{214}$Pb extends to low energies and is flat to the percent-level below 50 keV [35]. Alpha decays, on the other hand, are mono-energetic and have a different S1/S2 ratio from ER or NR events [56, 57], and hence are easy to select.

$^{214}$Bi decay does not represent an important background because it is quickly followed by $^{214}$Po, an isotope that undergoes alpha decay with a half-life of 164 $\mu$s [58]. Because this is much shorter than the drift time in XENON1T and XENONnT, the $^{214}$Bi and $^{214}$Po events are combined into a single event with two S1s, and two or more S2s. This is a unique event topology that is easy to select. Such events are termed BiPo events in this chapter.

## 2.2 Convection in the XENON1T Detector

### 2.2.1 Creating the Convection Field

Convection has been observed in earlier dual phase liquid xenon TPCs, such as XENON100 and LUX [62, 63]. While the exact boundary conditions driving the convection are not known, the convective flow is likely driven by the thermal flux into the TPC, possibly from both recirculation flows and from the cryostat. The relevant temperature gradient might be either horizontal or vertical.
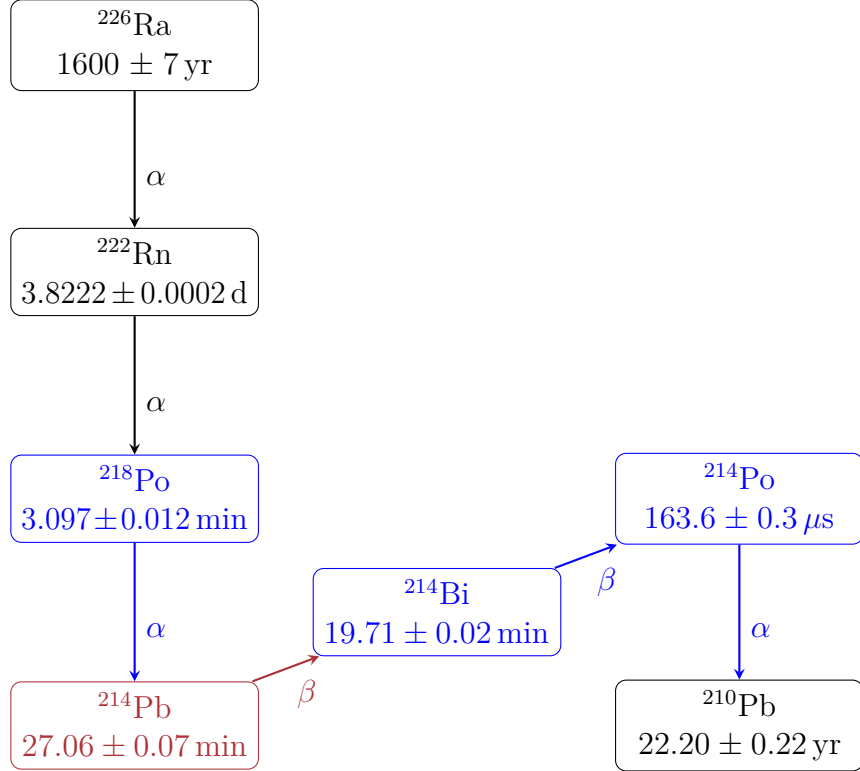
**Figure 2.1.** Decay chain of $^{222}$Rn, part of the uranium series. Only branches with branching fraction above 99.5% are shown. Data retrieved using the NNDC ENSDF, with the following Nuclear Data Sheets citations: [48, 58–61]. The isotope that decays to produce the background events being tagged in this work, $^{214}$Pb, is coloured red, whereas the isotopes with decays that are used for the tagging of $^{214}$Pb are coloured blue.

To measure the convective flow in the XENON1T detector, $^{222}$Rn and $^{218}$Po events are used. These events are selected using Gaussian Mixture clustering as implemented in `scikit-learn` [64] using the position-corrected S1, position-corrected S2, S2 width, radial coordinate, and z-coordinate of each event [65]. BiPo events, which will be used later, are selected by choosing events that have two interactions, corresponding to the $^{214}$Bi and $^{214}$Po decays. These interactions are required to be less than 5 cm apart in each of the x, y, and z directions, and the $\alpha$-event is further required to have appropriate position-corrected S1 and S2 values.

After event selection, $^{222}$Rn and $^{218}$Po events have to be paired to construct velocity vectors corresponding to the convective flow. However, the rate of $^{222}$Rn decays exceeds $10\,\mu$Bq/kg [66], corresponding to approximately two $^{222}$Rn events every 3 min in a 1 tonne fiducial mass. As the half-life of $^{218}$Po is $\sim 3$ min, the pairing of $^{222}$Rn and $^{218}$Po events cannot be done in a naive manner where every $^{218}$Po event is considered to be the daughter of the preceding $^{222}$Rn event. Instead, for each pair of $^{222}$Rn and $^{218}$Po events, the time difference ($\Delta t$) and displacement ($\Delta x$) are plotted on a histogram, see Figure 2.2. An excess of pairs where $\Delta x < 20$ cm and $0\,\text{s} < \Delta t < 40\,\text{s}$ becomes apparent. This is where correctly-paired events are expected. In addition, the distribution of $^{222}$Rn and $^{218}$Po events that are not correctly paired is independent of $\Delta t$, and can be determined using pairs where $\Delta t < 0$. One can then compute the purity of each histogram bin as $f_{\text{pure}} = 1 - N_{bg}/N_{bin}$, where $N_{bg}$ is the number of incorrect pairs in a bin at the given $\Delta t$ estimated using negative-time bins, and $N_{bin}$ is the total number pairs in a bin. With this, it is already possible to obtain a sample of pairs that can be used to measure the convection velocity simply by selecting all histogram bins with purities above a given threshold.

All permutations of $^{222}$Rn and $^{218}$Po pairs are used; hence one can improve on this method by iteratively selecting the bin with highest $f_{\text{pure}}$, and then removing all pairs which contain one of these $^{222}$Rn or $^{218}$Po events. The average purity of $^{222}$Rn-$^{218}$Po pairs as a function of the total number of pairs selected is shown in Figure 2.3 for both the naive and the iterative methods. It can be seen that the iterative method indeed provides a modest improvement.
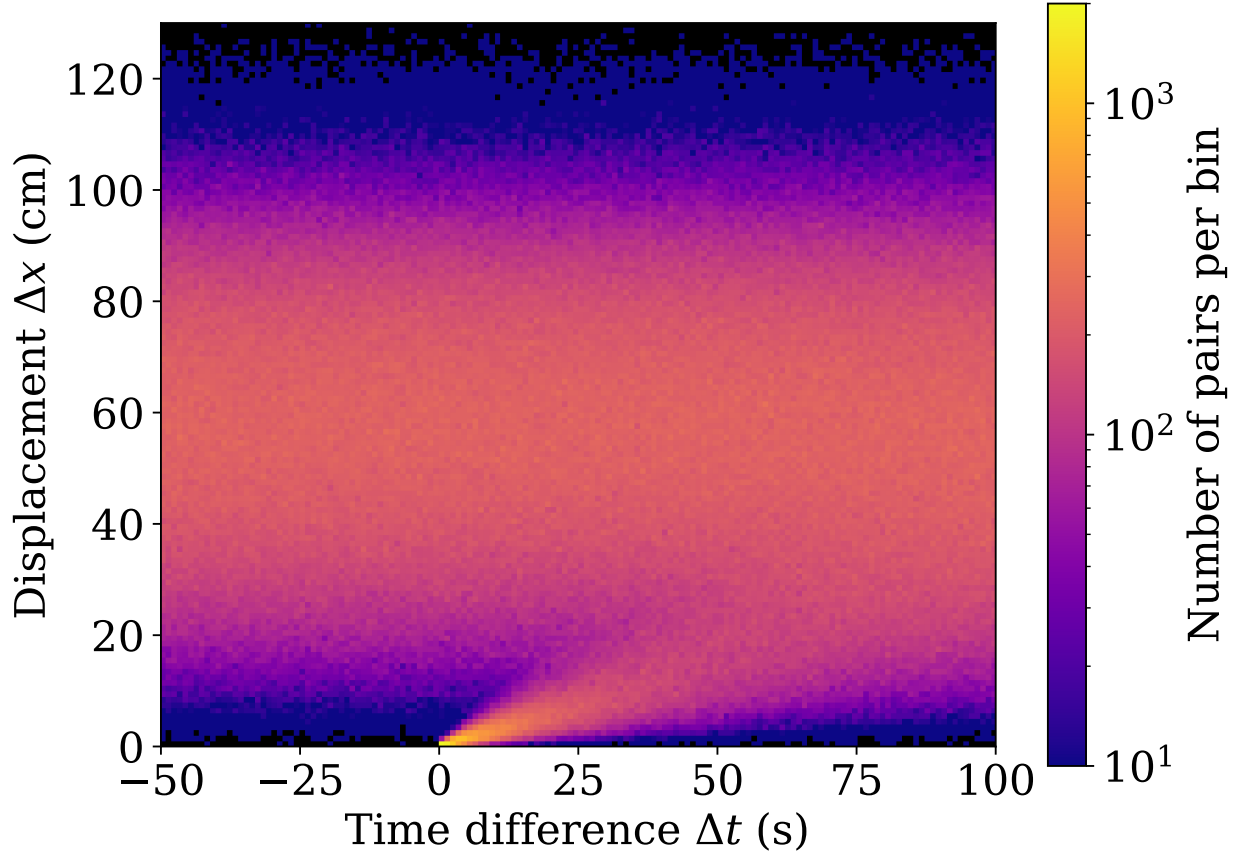
**Figure 2.2.** 2D histogram of the time difference ($\Delta t$) and displacement ($\Delta x$) of all permutations of $^{222}$Rn and $^{218}$Po pairs. The excess of pairs where $\Delta x < 20\,\mathrm{cm}$ and $0\,\mathrm{s} < \Delta t < 40\,\mathrm{s}$, is from correctly-paired events. At negative times, the pairs are unphysical and can be used to profile the distribution of incorrect pairs.
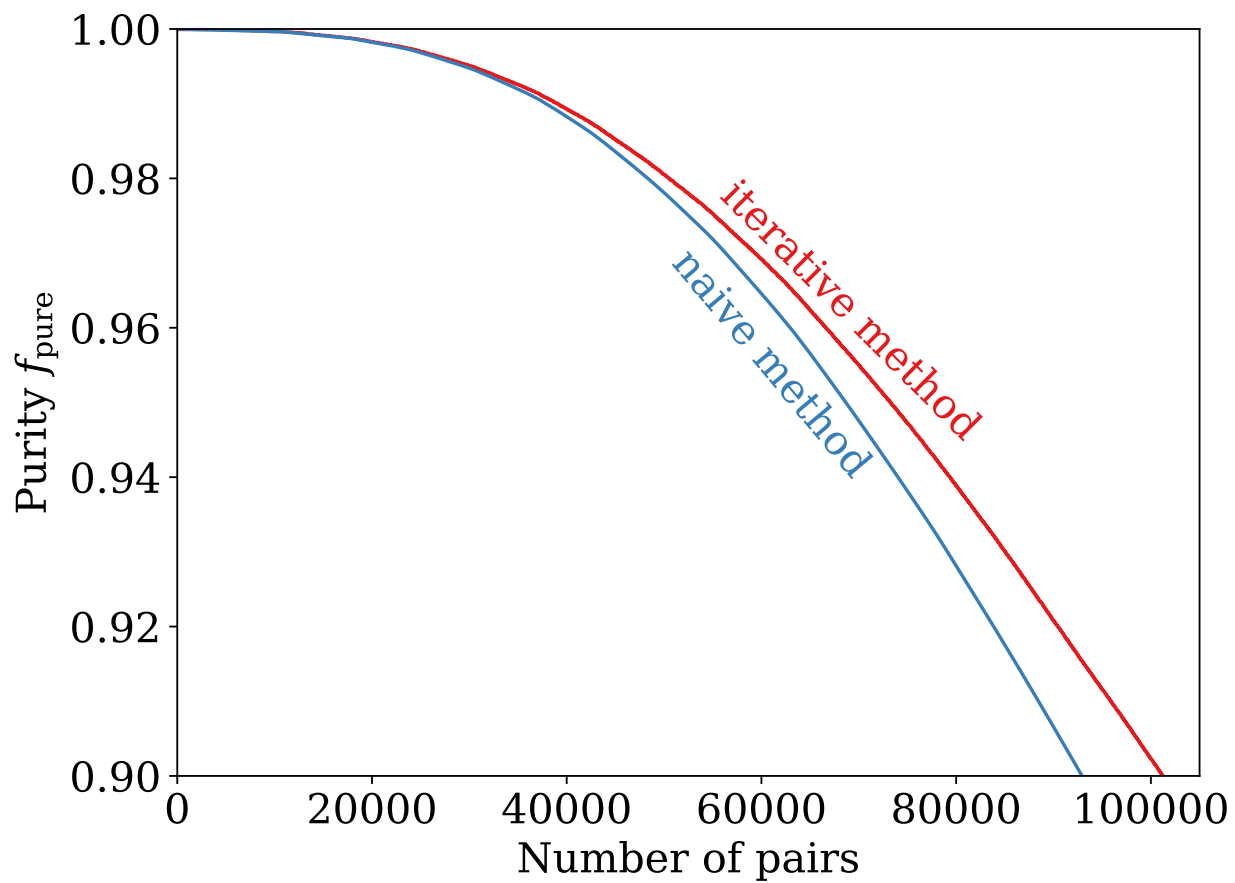
**Figure 2.3.** Plot of purity, $f_{\text{pure}}$ versus number of pairs for the iterative method, and for a naive method where one simply selects the histogram bins from Figure 2.2.

Vectors are constructed from selected pairs of events by computing the velocity from the $\Delta x$ and $\Delta t$ values of the pair. The velocity field obtained using the iterative method is shown in Figure 2.4. It can be seen that this velocity field is still noisy, and contains outliers that likely correspond to incorrectly-paired events.

It is notable that there appears to be a single large convection cell. While one might expect a toroidal convection flow due to cylindrical symmetry of the TPC, the observed asymmetric convection flow is expected for convection cells in a cylinder with an aspect ratio of close to 1 [67]. We have attempted to simulate this convection flow, but have been unsuccessful due to lack of knowledge of the boundary conditions driving this flow, and resultant inability to validate these simulations.

### 2.2.2   Filtering of the Velocity Field

The convection field shown in Figure 2.4 is then filtered and put on a grid. The purpose of this is to reduce noise and to speed up computation, as finding the nearest velocity vector to a given position is much faster with data on a regular grid. First, every vector of purity $f_{\text{pure}}$ is oversampled $25 \times f_{\text{pure}}$ times, rounded to the nearest integer. The x-y position reconstruction uncertainty of $\alpha$ events is estimated to be $\sigma_x = 0.3\,\text{cm}, \sigma_y = 0.3\,\text{cm}$, based on the spread observed in surface events [68], and the z-position uncertainty is estimated to be $\sigma_z = 0.17\,\text{cm}$ from the displacement of the two decays in BiPo events. During oversampling, each vector is perturbed randomly based on the position reconstruction uncertainty. The oversampled population of vectors are then put onto a grid with a grid spacing of $1/3\,\text{cm}$, by computing the geometric median [69] of the nearest 175 vectors at every grid point. The geometric median has been shown to be particularly robust for noisy datasets [70]. The result of this procedure is shown in Figure 2.5.
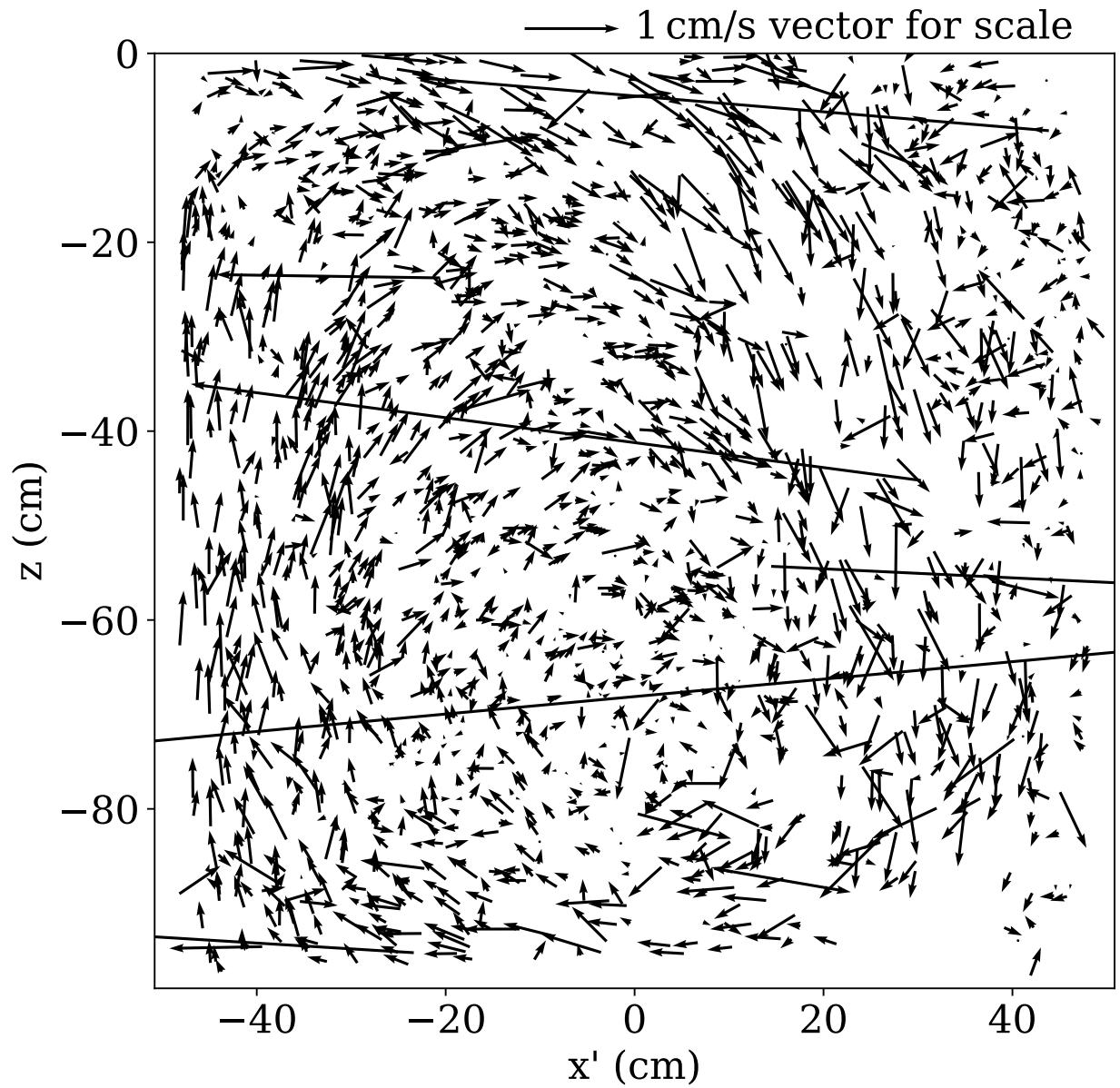
**Figure 2.4.** Slice of velocity field with 107804 vectors showing the convection cell. The $x'$ coordinate is perpendicular to the angular momentum vector. A 1 cm/s velocity vector is shown in the top right for scale.
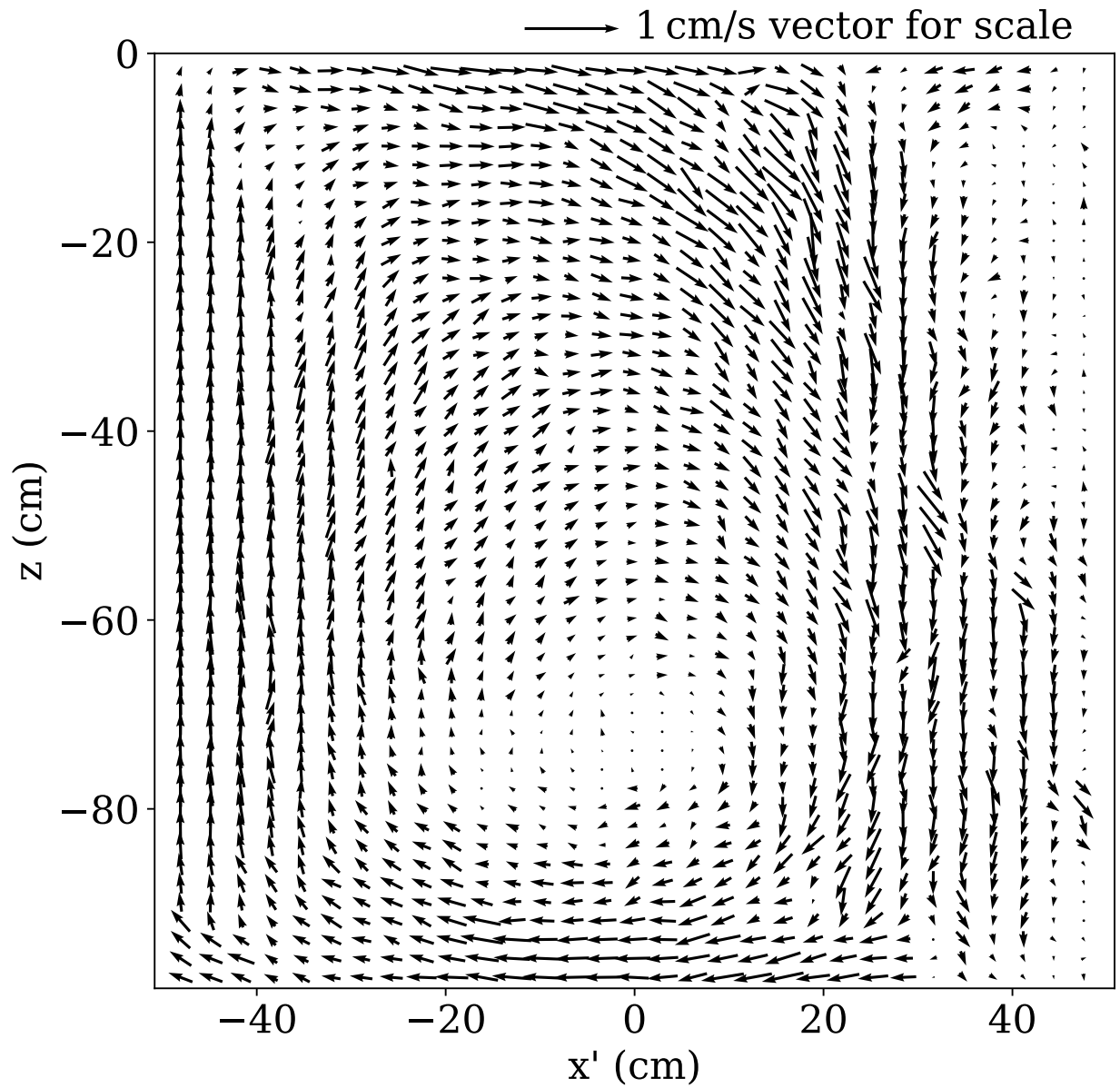
**Figure 2.5.** Slice of the velocity field after it was filtered and put on a grid. The $x'$ coordinate is defined as in Figure 2.4. For clarity, only every 6th vector is displayed. A 1 cm/s velocity vector is shown in the top right for scale.

### 2.2.3 Root-mean-square Convection Speed

The convection vectors obtained in subsection 2.2.1 allow a measurement of the bulk convection properties. To avoid biases due to uneven event densities, the detector is divided into 11 bins in $r^2 \in [0, 47.9^2]\text{cm}^2$, 10 bins in azimuth $\phi \in [-\pi, \pi]$, and 9 bins in $z \in [-96.9, 0]\text{cm}$. Every vector is then assigned to a bin, and given a weight $w_i$ equal to the reciprocal of the number of vectors in that bin. This procedure allows for the computation of a volume-averaged root-mean-square speed:

$$v_{\text{rms}} = \sqrt{\frac{\sum_{i=1}^{N} v_i^2 w_i}{\sum_{i=1}^{N} w_i}} \tag{2.1}$$

The uncertainty on each velocity vector can be estimated using the position reconstruction uncertainty as $\sigma_i = \sqrt{2\frac{\sigma_x^2 + \sigma_y^2 + \sigma_z^2}{\Delta t_i^2}}$. The total uncertainty is then given by

$$\sigma_{\text{rms}} = \sqrt{\frac{\sum_{i=1}^{N} v_i^2 \sigma_i^2 w_i}{\sum_{i=1}^{N} w_i}}. \tag{2.2}$$

The root-mean-square speed is thus found to be $0.30 \pm 0.01\,\text{cm/s}$. This is significantly slower than what was observed in XENON100 and LUX [62, 63]; however, it is significantly higher than EXO-200 and LZ where convection is sub-dominant to the mobility of charged ions [71, 72].

The heat flux into a TPC is likely proportional to the surface area, which is the square of linear dimension; when distributed over the entire target mass, which is related to the cube of linear dimension, one expects convection speed to vary linearly with linear dimension. The convection speeds for different liquid xenon TPCs is shown in Figure 2.6, plotted against the cube-root of the target mass, which is a proxy for linear dimension. It can be seen that convection speed decreases linearly with larger detectors, with the exception of EXO-200 [71]. EXO-200 is a single-phase liquid xenon TPC with a unique cooling solution where the liquid xenon vessel is immersed in a cryostat filled with a thermal-transfer fluid [73], and hence the heat flux into the TPC is much lower than in the other liquid xenon experiments which use vacuum-isolated cryostats.
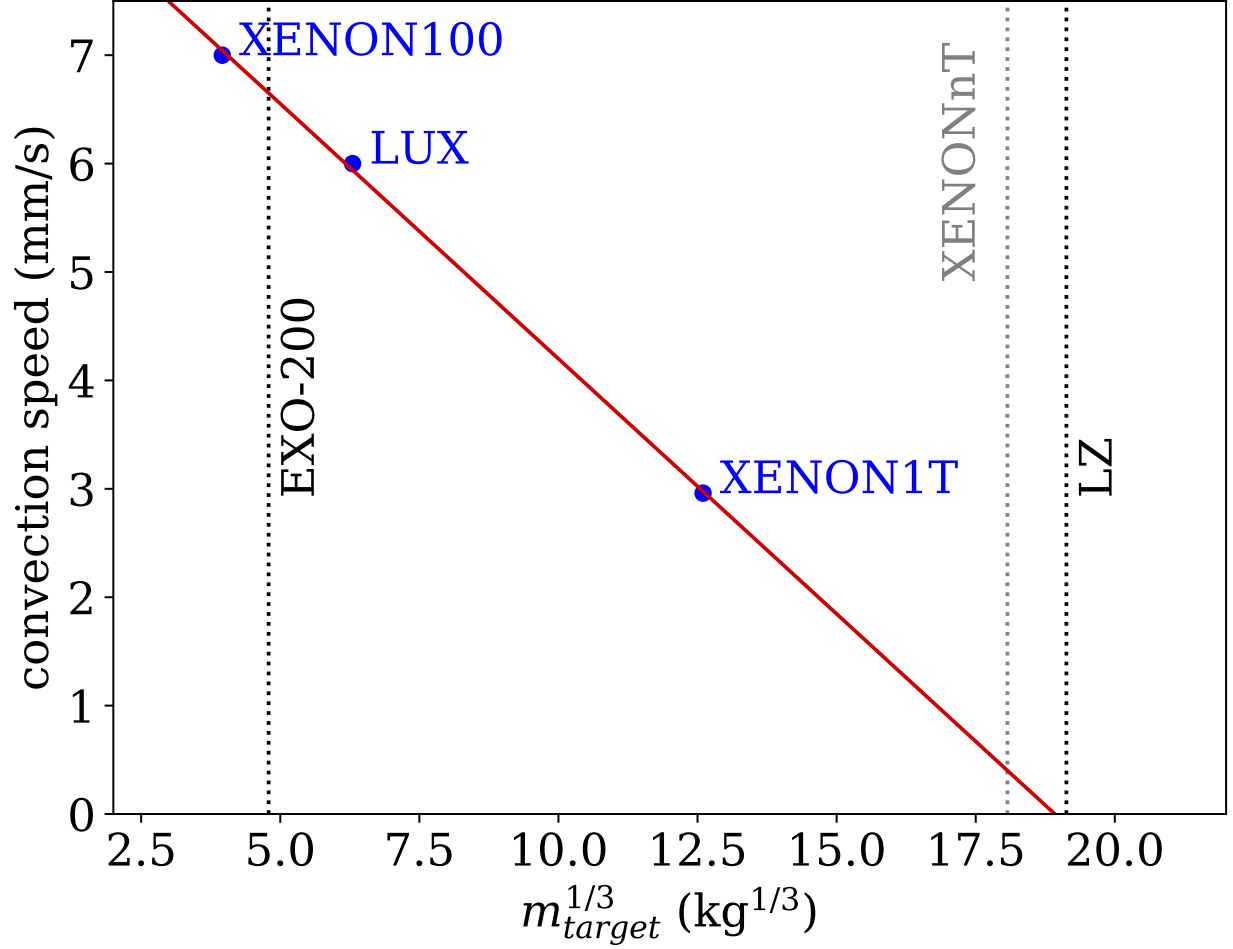
**Figure 2.6.** Convection speed versus (target mass)$^{1/3}$ for XENON100 [62], LUX [63], and XENON1T (this work), with a linear fit shown in red. It can be seen that convection speed decreases linearly. The target masses corresponding to EXO-200 and LZ are shown by the black dotted lines, as convection was not observed in EXO-200 [71], and was found to be subdominant to the drift of charged ions in LZ [72]. The target mass of XENONnT is indicated in grey as convection in XENONnT has not yet been analysed in detail.

## 2.3  $^{214}$Pb **Veto Algorithm**

### 2.3.1  Generation of Noise Fields

Uncertainty in the velocity field needs to be properly accounted for. Noise fields can be added to the velocity field to account for this uncertainty. However, the noise must be divergence-free to avoid introducing sources and sinks. Generation of the noise field starts with smoothed Gaussian noise with a $\sigma = 0.8$ cm kernel. After this, the curl is taken to ensure the noise is divergence free. 16 noise fields are generated, and then permuted by mirroring and rotating the fields, resulting in a total of 256 noise fields.

TPC surfaces must also be handled smoothly, and the velocity component perpendicular to the surfaces must approach zero at the surfaces. This is ensured by smoothly scaling the perpendicular component of the field to zero, starting 3 cm away from surfaces. This method of using the curl to generate divergence-free noise and handling boundaries is described in [74]. A section of the resultant noise field can be seen in Figure 2.7.

### 2.3.2  Point Cloud Propagation

A veto volume within which one looks for predecessor or daughter events is constructed using a point cloud. The predecessor and daughter events for $^{214}$Pb are $^{218}$Po and BiPo events (see Figure 2.1). A point cloud is first constructed around a $^{214}$Pb candidate event and then propagated using the convection and noise velocity fields, with every point in the point cloud exposed to a different randomly-assigned noise field to account for uncertainty in the velocity field (see subsection 2.3.1). As one only needs to consider $^{214}$Pb candidate events within the energy region of interest to a given analysis, propagating a point cloud from every $^{218}$Po and BiPo event is more computationally intensive than from the smaller number of low-energy $^{214}$Pb events. Point clouds from each $^{214}$Pb candidate event are thus propagated in the forward and backward directions to look for BiPo and $^{218}$Po events, respectively. These search directions are termed the BiPo and $^{218}$Po channels for the rest of this chapter. An illustration of a point cloud propagated along the velocity field can be seen in Figure 2.8.
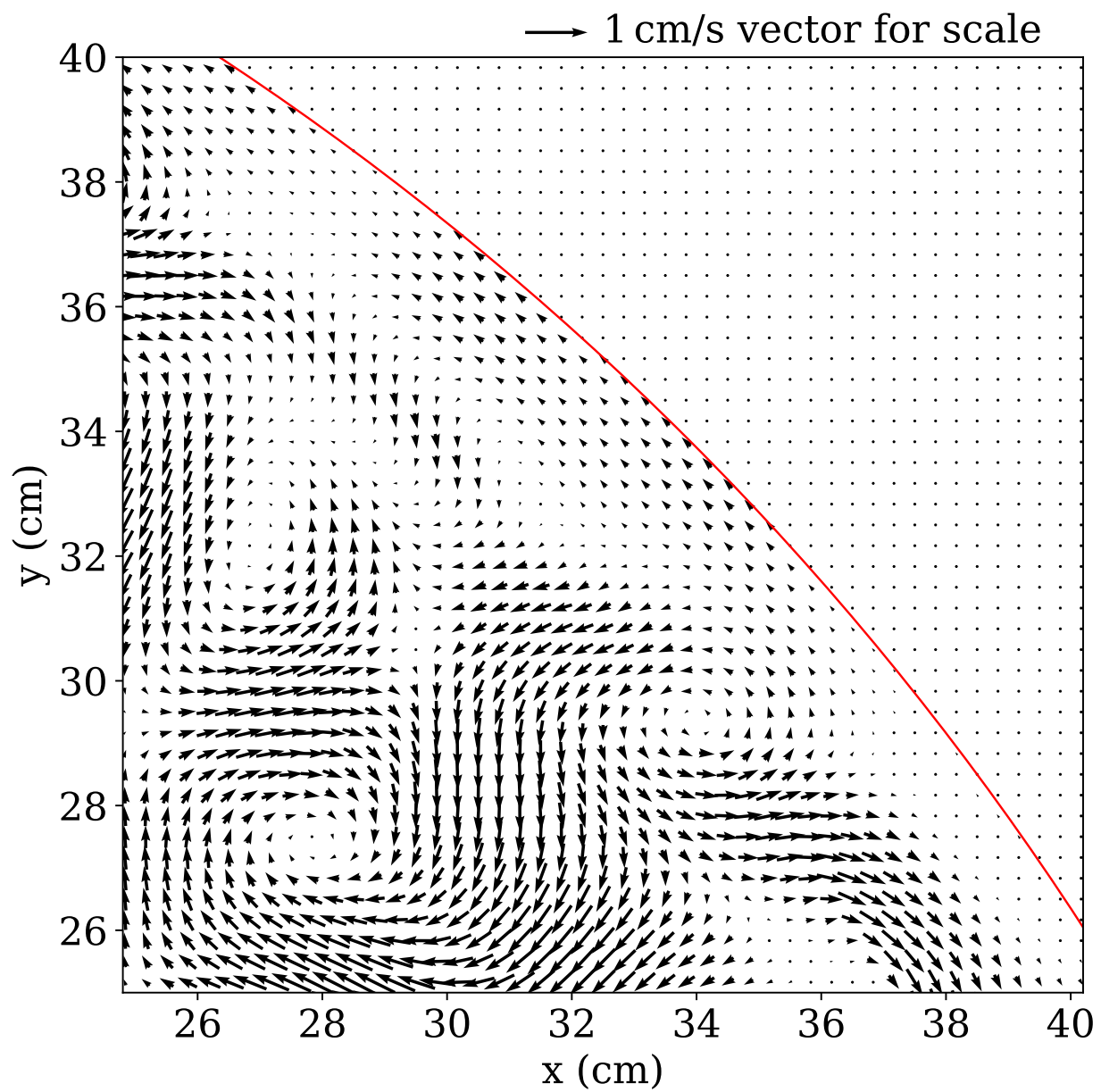
**Figure 2.7.** Zoomed-in sample of the noise field. The edge of the detector is shown in red. It can be seen that the boundaries are handled smoothly, and that the field has no sinks that can trap propagating points.
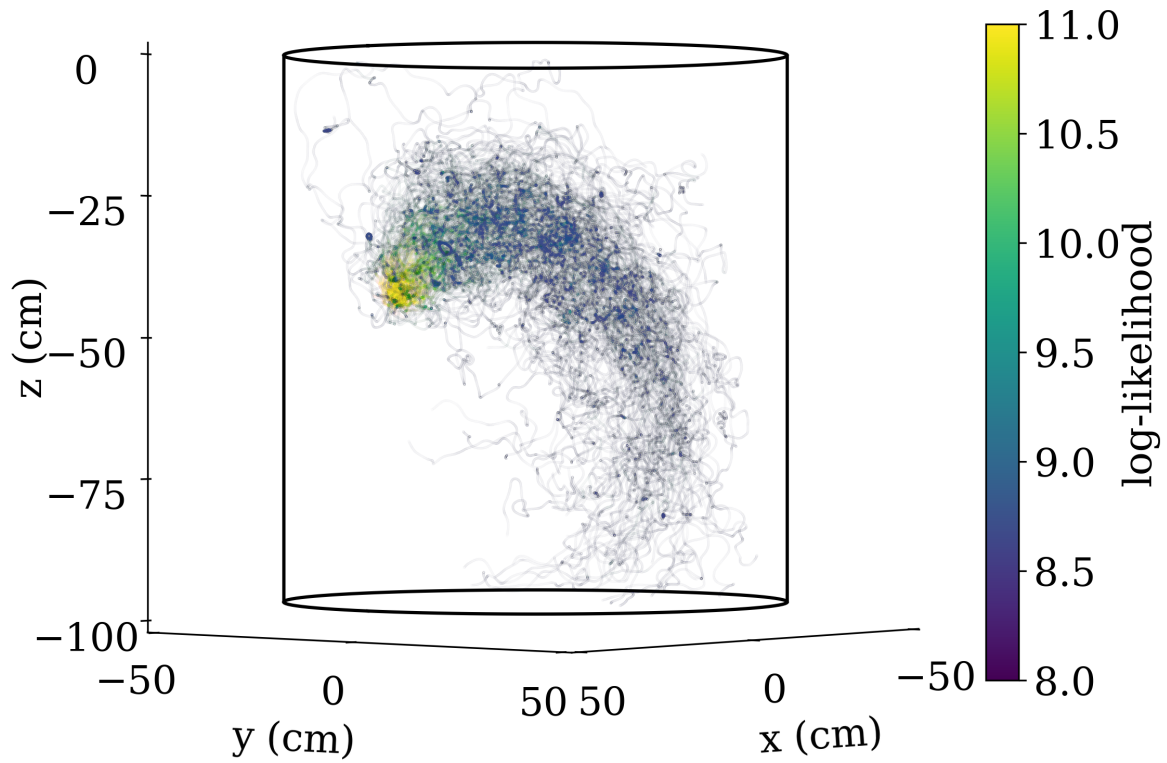
**Figure 2.8.** Plot of a point cloud and the associated log-likelihood at each point. For illustration, the likelihood threshold is relaxed to 8 show the convection flow. There are 192 points in the initial point cloud, and the timestep size is 0.05 s

There are four main steps involved in the generation and propagation of this point cloud:

1. A $^{214}$Pb candidate event is identified.

2. A point cloud is generated around the event, representing the position reconstruction uncertainty. The radial position uncertainty is $\sigma_R = 5.2\,\mathrm{cm} - (1.61\,\mathrm{cm})\log_{10}(S2/PE) + (0.019\,\mathrm{cm})\sqrt{S2/PE}$ [68], whereas the z-position uncertainty is estimated to be $\sigma_z = 0.17\,\mathrm{cm}$ from the displacement of the two decays in BiPo events.

3. Every 600 timesteps (30 s), a probability density function is built out of the point cloud produced in the past 600 timesteps. This is done using kernel density estimation (KDE) in 4-dimensions. To this end, a top-hat kernel of radius 3 cm, and 0.3 sec in the time-axis is used. Points that fall below a threshold of log-likelihood ($\xi$) are culled to speed up computation. This log likelihood threshold is a free parameter.

4. DBScan clustering [75] is used to remove outlier points.

5. The algorithm repeats from step 3, until all points have been removed.

A time-slice of a point cloud at every 594th (600-6, to avoid edge-effects from KDE) timestep is shown in Figure 2.9, with a log-likelihood constraint of 9.1, same as that used in the final analysis in the BiPo channel.
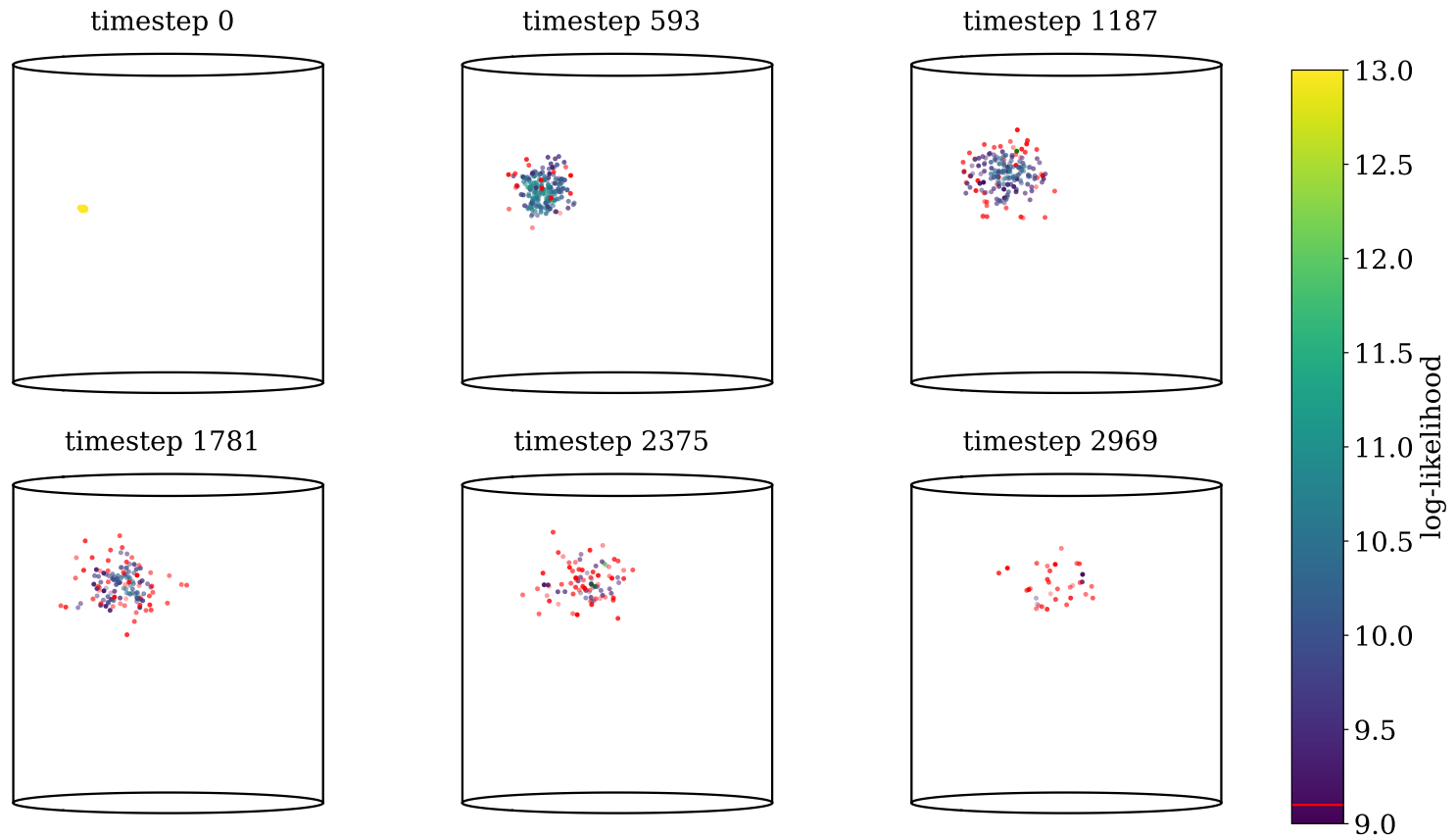
**Figure 2.9.** Plot of point cloud with associated likelihoods at 6 different timesteps (0 s, 29.65 s, 89.05 s, 118.75 s, and 148.45 s). Red points are culled by the log-likelihood limit and not propagated further to speed up computation.

### 2.3.3 Optimisation of Veto Volume

As the algorithm looks forward in time for BiPo events, and backwards in time for $^{218}$Po events, there are two free parameters representing the log-likelihood thresholds $(\xi_{BiPo}, \xi_{Po})$ that have to be optimised. To this end, electronic recoil data from science run 0 of XENON1T between 30 keV and 70 keV is used [35].

To find the optimal values for these two parameters, the software radon veto is run on the entire dataset twice. For one of the two runs, the velocity field and time directions are reversed, so that due to causality, the $^{214}$Pb candidate cannot be related to the $^{218}$Po or BiPo events. This creates a sample of events that are vetoed purely due to coincidence, allowing for the probability of vetoing an event purely due to coincidence ($p_{\text{coinc}}$) to be profiled. For the forward-direction run where one searches for BiPo and $^{218}$Po events in the correct directions, the fraction of events that is $^{214}$Pb ($p_{\text{Pb}}$) is determined from a spectral fit from the XENON1T low-energy electronic recoil analysis [35]. A likelihood function is then used to fit the probability of vetoing a $^{214}$Pb event ($p_{\text{true}}$) and the probability of vetoing an event purely due to coincidence ($p_{\text{coinc}}$). $p_{\text{true}}$ and $p_{\text{coinc}}$ can also be interpreted as the $^{214}$Pb background reduction and the exposure loss, respectively. The likelihood function for a vetoed event is:

$$
\begin{aligned}
\ell_{i,\text{veto}}\left(p_{\text{true}}, p_{\text{coinc}}\right) = & \, p_{\text{Pb}}(E_i) p_{\text{true}} + \\
& (1 - p_{\text{Pb}}(E_i)) p_{\text{coinc}}
\end{aligned}
\tag{2.3}
$$

where $\ell_{i,\text{veto}}\left(p_{\text{true}}, p_{\text{coinc}}\right)$ is the likelihood for the $i^{\text{th}}$ event to be vetoed, $E_i$ is the energy of the event, and $p_{\text{Pb}}(E_i)$ is the fraction of events resulting from the decay of $^{214}$Pb, as determined from the XENON1T low-energy electronic recoil analysis spectral fit.

The likelihood function for a candidate event that is not vetoed for the forward-direction runs is:

$$
\begin{aligned}
\ell_{j,\text{nveto}}\left(p_{\text{true}}, p_{\text{coinc}}\right) = & \, 1 - p_{\text{Pb}}(E_j) p_{\text{true}} - \\
& (1 - p_{\text{Pb}}(E_j)) p_{\text{coinc}}
\end{aligned}
\tag{2.4}
$$

where $\ell_{j,\text{nveto}}(p_{\text{true}}, p_{\text{coinc}})$ is the likelihood for the $j^{\text{th}}$ event not vetoed.

For the reversed runs, the likelihoods are the same, except that $p_{\text{Pb}}$ is set to zero, because the candidate event cannot be related to any $^{218}$Po or BiPo events found. The likelihood function that is used to fit the probabilities $p_{\text{true}}$ and $p_{\text{coinc}}$ is then the sum of the log-likelihoods from each individual candidate event. This is done separately for the $^{218}$Po and BiPo channels, to produce four probabilities: the probability of vetoing an event due to coincidence via the BiPo channel ($p_{\text{coinc,BiPo}}$), the probability of vetoing an event due to coincidence via the $^{218}$Po channel ($p_{\text{coinc,Po}}$), the probability of vetoing a $^{214}$Pb event via the BiPo channel ($p_{\text{true,BiPo}}$), and the probability of vetoing a $^{214}$Pb event via the $^{218}$Po channel ($p_{\text{true,Po}}$).

If a signal is much smaller than the background, the significance of a counting experiment scales as $\text{signal}/\sqrt{\text{background}}$ [76]. One can thus compute a normalised sensitivity for a dark matter search:

$$Z = \frac{\text{signal}}{\sqrt{\text{background}}} \tag{2.5}$$

where

$$\text{signal} = \hat{p}_{\text{coinc,BiPo}} \times \hat{p}_{\text{coinc,Po}},$$

$$\text{background} = 1 - (1-\alpha) \times$$

$$[1 - \hat{p}_{\text{coinc,BiPo}} \times \hat{p}_{\text{coinc,Po}}]$$

$$- \alpha \left[ 1 - (\hat{p}_{\text{coinc,BiPo}} \times \hat{p}_{\text{coinc,Po}}) \right]$$

$$\hat{p}_{\text{coinc,BiPo}} = 1 - p_{\text{coinc,BiPo}}(\xi_{BiPo})$$

$$\hat{p}_{\text{coinc,Po}} = 1 - p_{\text{coinc,Po}}(\xi_{Po})$$

$\xi_{Po}$ and $\xi_{BiPo}$ refer to the likelihood threshold parameters being optimised for the $^{218}$Po and BiPo channels, respectively, and $\alpha$ refers to the fraction of the background that can be attributed to $^{214}$Pb. This is energy dependent in principle, but is approximated to be a constant $\alpha = 0.8$ for the purposes of this optimisation, as given by the average between $0\,\text{keV}$ and $30\,\text{keV}$.

Finally, this process can be repeated for multiple values of the threshold parameters that govern the veto volume size in the $^{218}$Po and BiPo channels. The result of this can be seen

in Figure 2.10. It can be seen that the sensitivity improvement is modest in XENON1T. However, as this is an analysis technique, it can still be a cost-effective addition to hardware radon-mitigation efforts, such as the cryogenic distillation system in XENONnT [50]. In addition, as will be shown later in sections 2.4.3 and 2.4.4, much higher performance is possible in systems with lower background radon levels and which have slower convective flows.
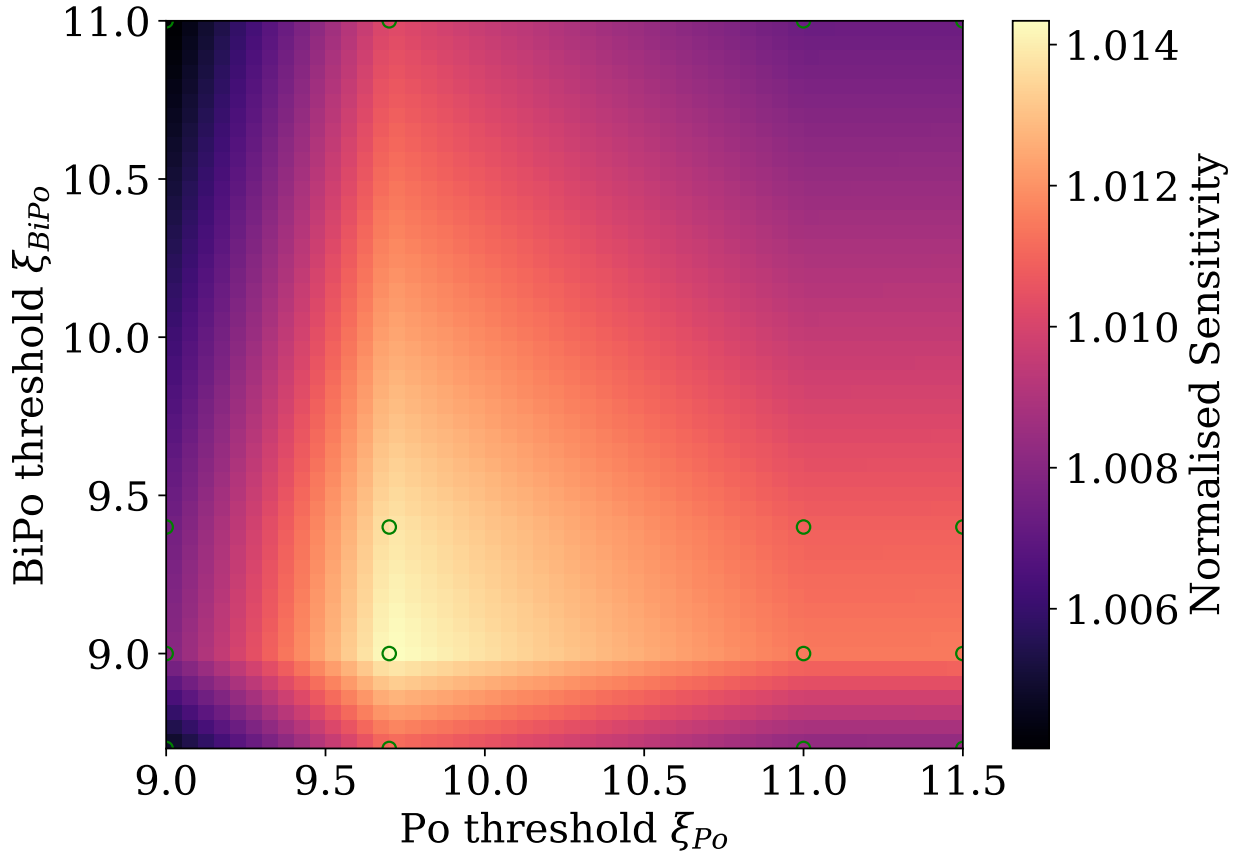


**Figure 2.10.** Plot of the improvement in sensitivity of XENON1T for a NR dark matter signal at various values of the BiPo and $^{218}$Po point cloud threshold parameters. The colour plot in the background shows the linearly interpolated sensitivity between data points, and the actual data points are indicated with green circles. 1 on the colour scale corresponds to the same sensitivity as what one would achieve without the software radon veto.

## 2.4   Results and discussion

### 2.4.1   Demonstration of software radon veto

The low-energy ER search dataset from XENON1T [35] is used to demonstrate how this software radon veto would work in practice. For this section, the same data used in subsection 2.3.3 is used, but with the energy range $[0\,\mathrm{keV}, 70\,\mathrm{keV}]$ instead. Similarly to subsection 2.3.3, both $^{218}$Po and BiPo channels are used to tag events as $^{214}$Pb. The thresholds used are $\xi_{Po} = 9.7$ and $\xi_{BiPo} = 9.0$.

Following this, the likelihoods shown in Equation 2.3 and Equation 2.4 are used to fit $p_{\mathrm{true}}$ and $p_{\mathrm{coinc}}$. This is shown in Figure 2.11. The fit corresponds to an exposure loss of $1.8 \pm 0.2\%$, and a $6.2^{+0.4}_{-0.9}\%$ reduction in the $^{214}$Pb background.
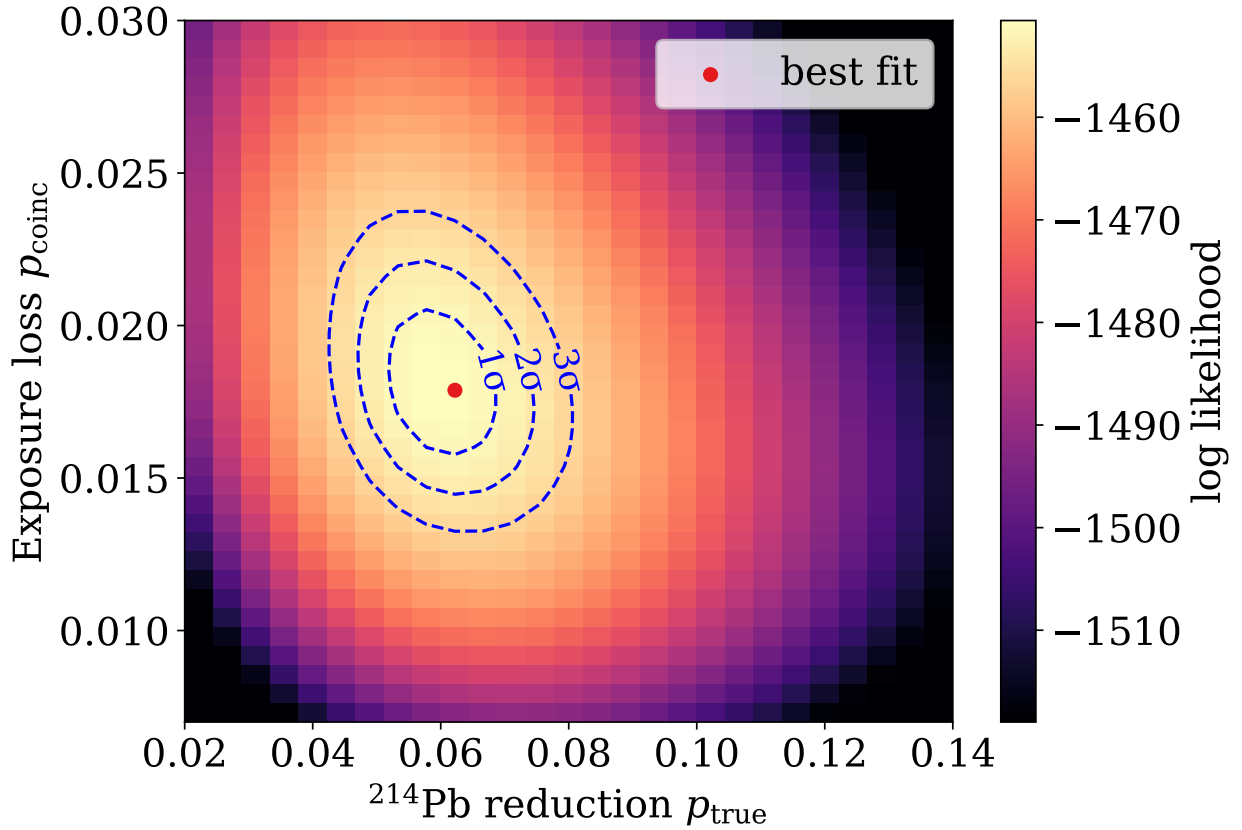


**Figure 2.11.** Likelihood fit using events from the low-energy ER search dataset and the likelihoods discussed in subsection 2.3.3. In this plot, the best fit values of the $^{214}$Pb background reduction ($p_{\mathrm{true}}$) and the exposure loss ($p_{\mathrm{coinc}}$) are marked in red, and the error ellipses are shown in blue.

The expected background spectrum is then computed by multiplying the components of the background fit from [35] that are not from $^{214}$Pb with $1 - p_\text{coinc}$, multiplying the $^{214}$Pb background with $1 - p_\text{true}$ and summing the two. This is shown in Figure 2.12. It can be seen that the red line is a good fit for the data.
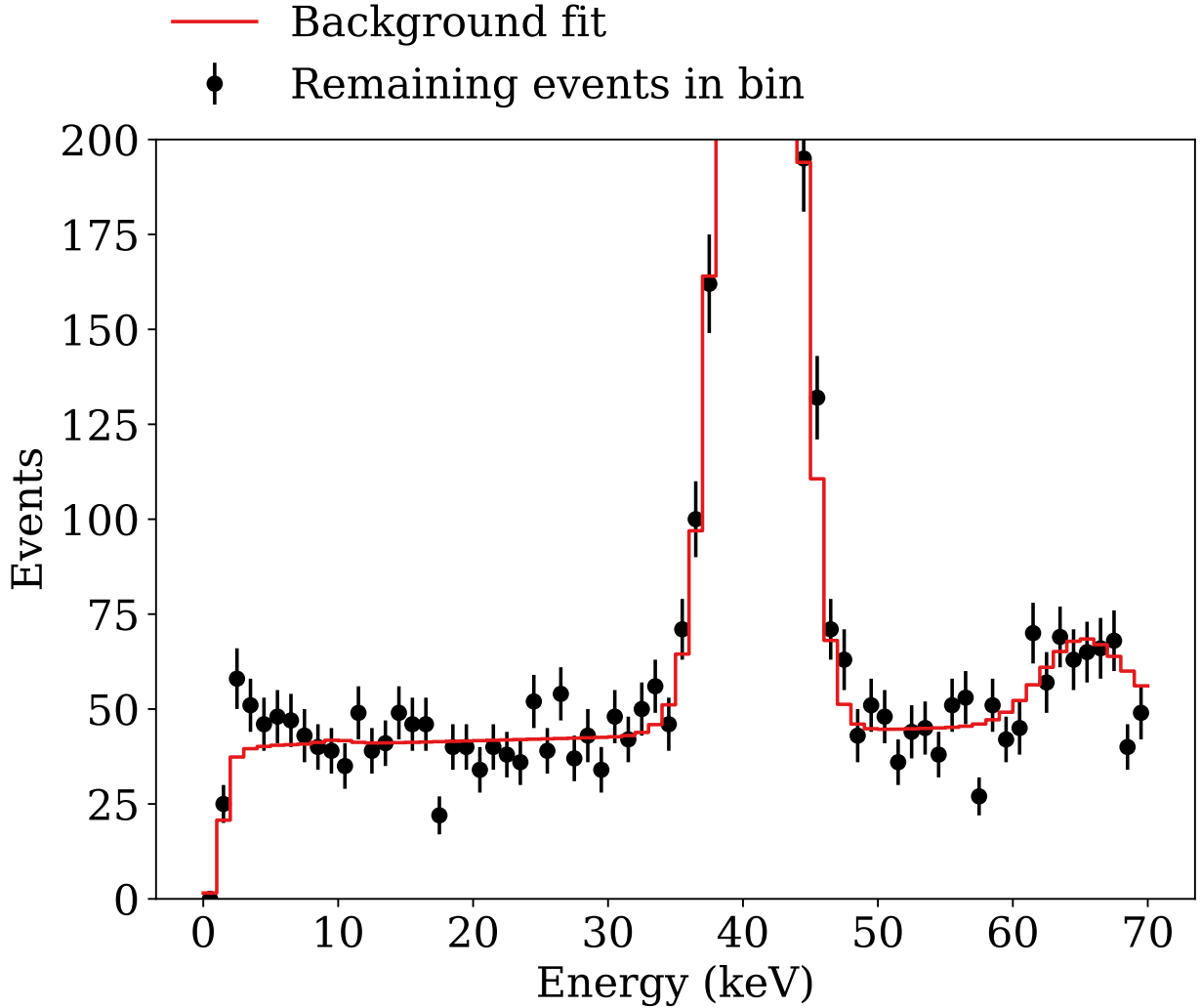


**Figure 2.12.** Spectrum of events remaining after the software radon veto with 1-sigma Poisson confidence intervals (black), compared with the expected background spectrum based on the signal-free spectral fit from [35] and the inferred values of $p_\text{true}$ and $p_\text{coinc}$ (red). The peaks at $42\,\text{keV}$ and 64 are due to $^{83m}$Kr and $^{124}$Xe decay, respectively [35].

In XENON1T, an ER excess was observed with 285 events between $1\,\text{keV}$ and $7\,\text{keV}$ [35], a $3.3\sigma$ Poisson fluctuation over the expectation of 232 events. In the unvetoed data and

scaled background fit, there are 275 events in the same energy range and an expectation of 220, corresponding to a $3.6\sigma$ excess according to Poisson statistics, demonstrating a small improvement as expected from subsection 2.3.3. This also affirms that the excess is not related to the $^{214}$Pb background, in agreement with the lack of an excess observed in the XENONnT low-energy electronic recoil search [36].

We can demonstrate that this software radon veto indeed selects $^{214}$Pb events by looking at the energy spectrum of vetoed events. To this end, a portion of the fiducialised data from the search for neutrinoless double-beta decays in XENON1T is used [31]. This data corresponds to 22.05 days of exposure with a fiducial mass of $741 \pm 9$ kg. A spectral fit between 270 keV and 2000 keV includes both spectral features due to $^{214}$Bi excited states at 295 keV and 352 keV, and the beta decay Q-value of 1018 keV [60], but avoids low-energy features in the spectrum from $^{83m}$Kr and $^{131m}$Xe. The selected data with a spectral fit is shown in Figure 2.13.

The software radon veto is run on the dataset shown in Figure 2.13 with thresholds of $\xi_{Po} = 9.7$ and $\xi_{BiPo} = 9.4$ in order to obtain a relatively clean sample of $^{214}$Pb decays. Following that, the same procedure used above for the low-energy ER search is used to fit $p_{\text{true}}$ and $p_{\text{coinc}}$; however, here events that are tagged as $^{214}$Pb are examined instead. Thus, the components of the spectral fit that are not from $^{214}$Pb are multiplied with $p_{\text{coinc}}$, and the $^{214}$Pb component is multiplied by $p_{\text{true}}$.

This result is shown in Figure 2.14. It can be seen that the tagged population is indeed dominated by the decay of $^{214}$Pb, and it is also possible to identify relevant spectral features at 295 keV and 352 keV, as well as the Q-value of 1018 keV [60]. In particular, the $^{214}$Pb decay endpoint can be clearly identified in the tagged population in Figure 2.14, but not in the full dataset shown in Figure 2.13.
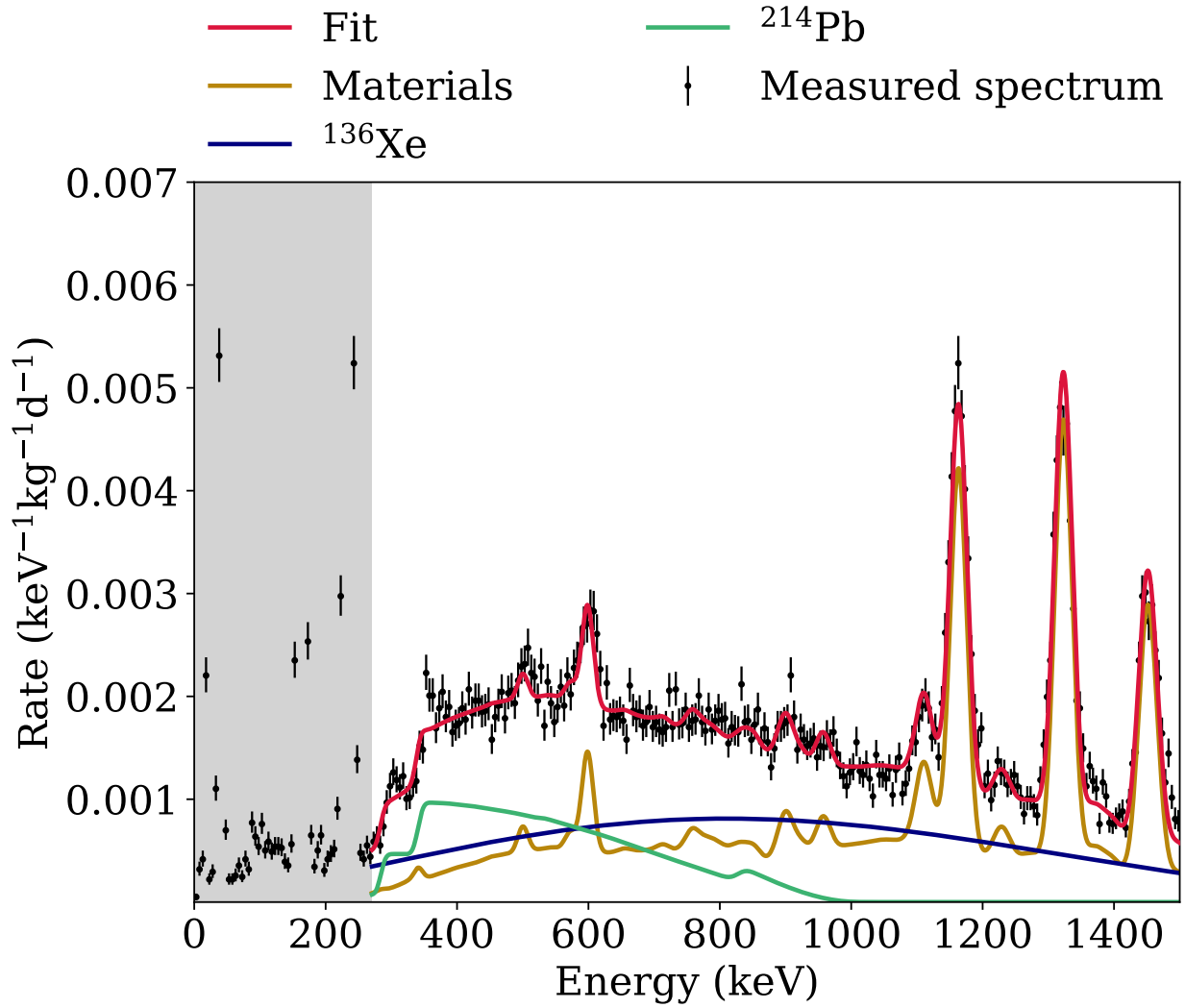
**Figure 2.13.** Spectrum of events in the XENON1T double beta decay dataset [31] corresponding to 22.01 days of exposure. Data points with 5 keV bins is shown in black. A spectral fit is shown in solid lines, with the summed fit in red. The grey shaded region indicates data that is not used for fitting.
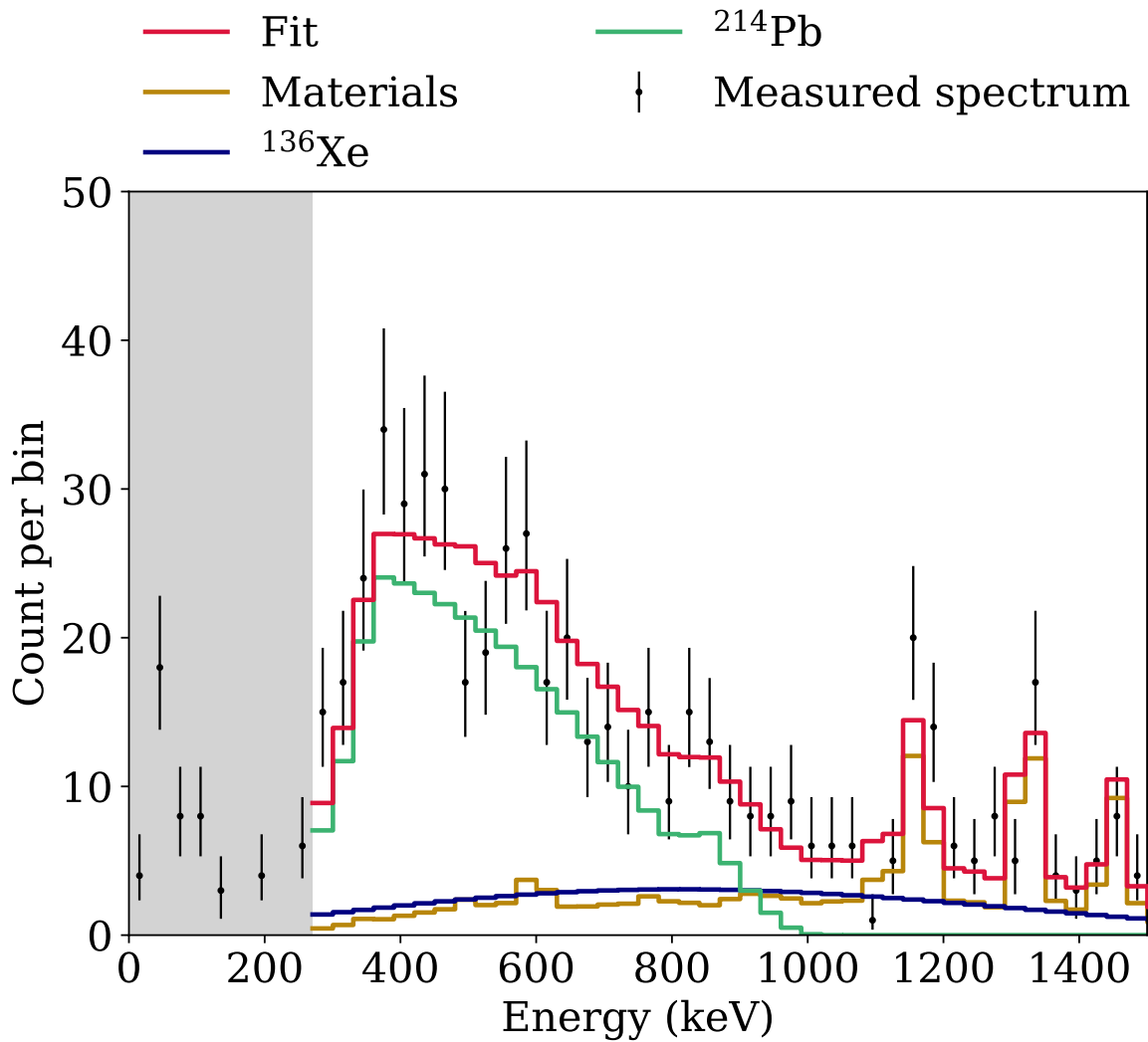
**Figure 2.14.** The spectrum of events in the population of events tagged as $^{214}$Pb. It can be seen both from the fit and from the shape of the spectrum that the $^{214}$Pb fraction is greatly enhanced in the vetoed sample. The grey shaded region indicates data that is not used for fitting.

### 2.4.2 Example of a recovered decay chain

A reconstructed example of the portion of the decay chain that is used for the software radon veto is shown in this section. (compare Figure 2.1) The software radon veto is used to find the $^{218}$Po and BiPo events from the $^{214}$Pb event. Tagging a $^{214}$Pb event only requires matching either a $^{218}$Po or BiPo event, however, in the chosen example, both $^{218}$Po and BiPo events were found. The $^{222}$Rn event related to the $^{218}$Po was then found via the matching procedure shown in subsection 2.2.1. The four identified events can be seen in Figure 2.15, laid over the same velocity field shown in subsection 2.2.2, with waveforms shown in Figure 2.16.

It can be seen that the events propagate along the velocity field. All the waveforms have a single large S1 and a single large S2, except for the BiPo event. The BiPo event is made up of two decays, thus has at least two S1s and S2s. In this case, there are more than two S2s because the beta decay of $^{214}$Bi has only a 19.2% chance of decaying directly to the ground state; more typically decaying to short-lived excited states and emitting one or more gamma rays in addition to the beta particle [60]. The large S1s and S2s, corresponding to the relevant events, are also followed by single and few-electron signals largely due to photoionisation within the time window shown [77]. These waveforms match our expectations for the respective event types.
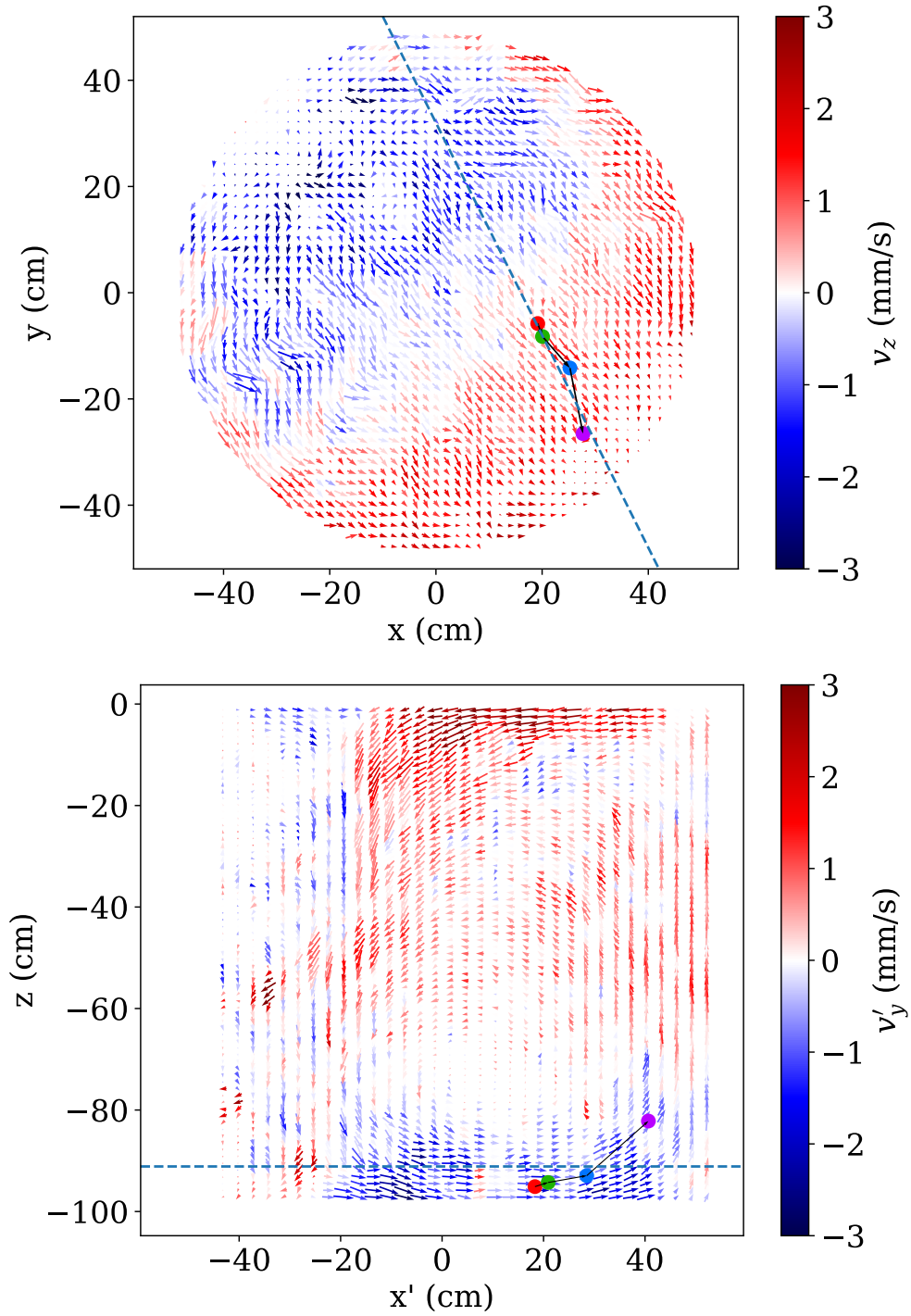
**Figure 2.15.** The positions of a $^{222}$Rn event (red), a $^{218}$Po event (green), a $^{214}$Pb event (blue), and a BiPo event (purple) are shown here, overlaid on top of the velocity field in the detector. The top view is shown above, and a side view is shown below. The blue dotted line on the top and side views are used to show the slices taken to create the side and top views, respectively.
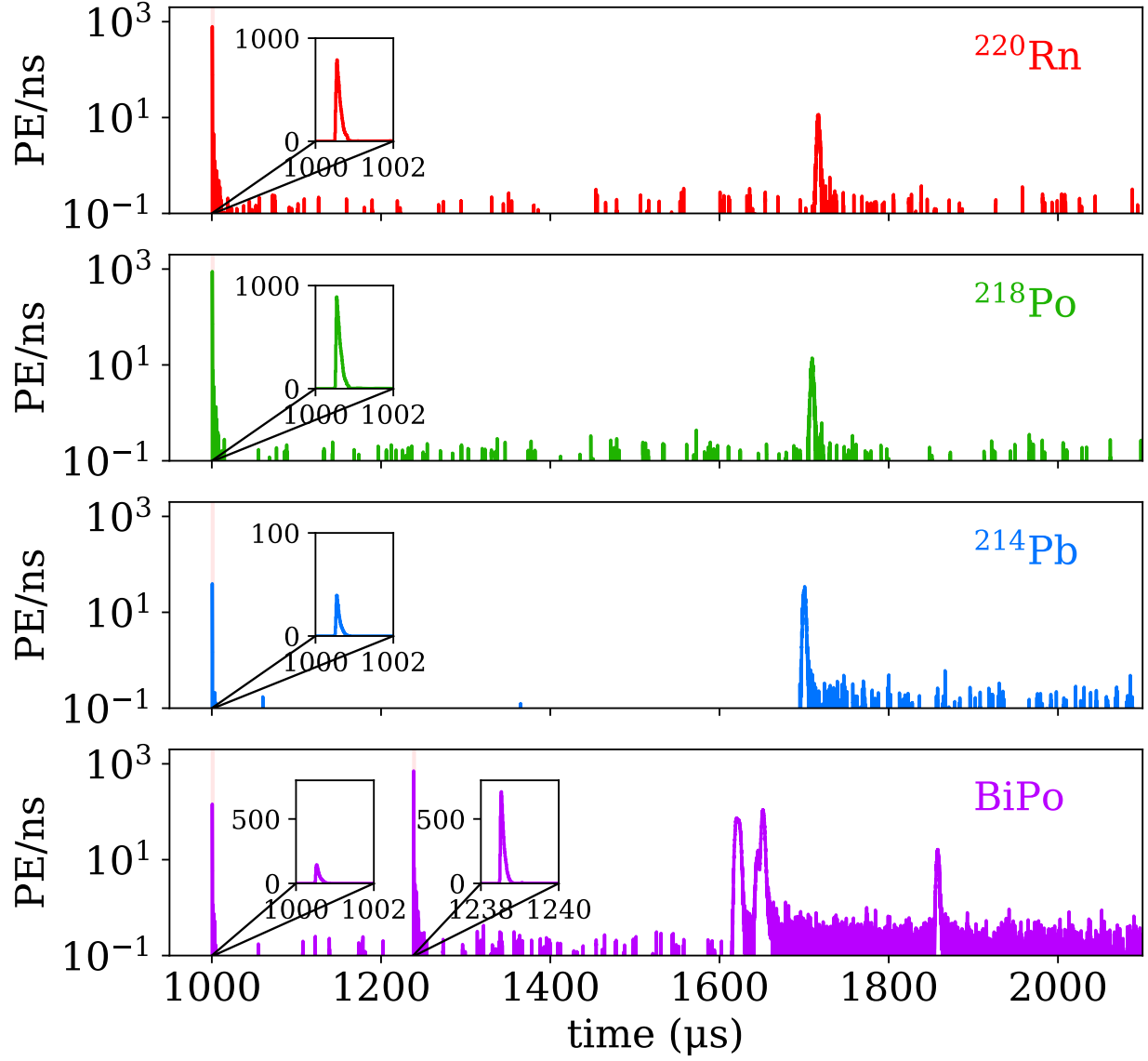
**Figure 2.16.** Waveforms of the events in Figure 2.15. From top to bottom, the waveforms correspond to the identified $^{222}$Rn (red), $^{218}$Po (green), $^{214}$Pb (blue), and BiPo (purple) events. Insets show the S1 waveforms with units identical to the main plots.

### 2.4.3   Projection of performance in XENONnT

To project the performance of this technique to XENONnT, a model of how the software radon veto performs under various conditions must be constructed. For each channel, the probability of incorrectly vetoing an event that is not $^{214}$Pb is simply given by the size of the point cloud used to construct the veto volume, multiplied by the rate of $^{218}$Po or BiPo events. When propagating particles along a 3-dimensional flow, chaotic mixing is expected to occur. This makes the point cloud size diverge exponentially with time [78]. As such, the growth of the point cloud volume can be modelled with a Lyapunov exponent – the characteristic exponential divergence of two close trajectories [79]. The probability of incorrectly vetoing an event that is not $^{214}$Pb as a function of the time the point cloud is propagated for is given by:

$$
\begin{aligned}
p_{\text{coinc}}(t) &= A \cdot C \int_0^t e^{v\lambda\tau} d\tau \\
&= A \cdot C \frac{e^{v\lambda t} - 1}{v\lambda}
\end{aligned}
\tag{2.6}
$$

where $A$ is the activity of $^{218}$Po or BiPo events, depending on the channel being modelled, $v$ is the convection speed, $t$ is the time the point cloud is being propagated, and $C$ and $\lambda$ are fitting constants.

The probability of correctly vetoing an event that is $^{214}$Pb, on the other hand, can be modelled with the exponential decay of the radioactive species, multiplied by the probability of there being a correctly reconstructed $^{218}$Po alpha or BiPo event in the detector, $p_{\text{branch}}$. As the efficiency of detecting alphas is high, the probability for the $^{218}$Po channel is approximated as $p_{\text{branch, Po}} = 1$. The probability for the BiPo channel has to account for the effect of plate-out onto surfaces in the detector [80] and less efficient selections, and as such is taken to be the ratio of the BiPo rate as measured using fully-reconstructed BiPo events in the XENON1T detector and the rate of $^{214}$Pb events from the search of dark matter in the electronic recoil channel [35] as $p_{\text{branch, BiPo}} = 0.25$. As this includes selection efficiencies and plate-out, this number might change between detectors, but is kept constant here to estimate the XENONnT performance. The probability of correctly vetoing an event that is $^{214}$Pb is thus given by:

$$p_{\text{true}}(t) = p_{\text{branch}}\lambda_{\text{decay}} \int_0^t e^{-\lambda_{\text{decay}}\tau} d\tau$$
$$= p_{\text{branch}} \left(1 - e^{-\lambda_{\text{decay}}t}\right) \tag{2.7}$$

where $\lambda_{\text{decay}}$ is the decay constant of the radioactive species relevant to the specific channel, $p_{\text{branch}}$ is the multiplicative factor stemming from selection efficiencies and plate out as detailed above, and $t$ is the time the point cloud is being propagated. Equations (2.6) and (2.7) can then be combined to produce

$$p_{\text{coinc}} = \frac{A \cdot C}{v\lambda} \left( \left(1 - \frac{p_{\text{true}}}{p_{\text{branch}}}\right)^{-\frac{v\lambda}{\lambda_{\text{decay}}}} - 1 \right). \tag{2.8}$$

With Equation 2.8, there are only two free parameters, $C$ and $\lambda$. These two free parameters can be fit by running the software radon veto with different veto volumes on the $^{218}$Po and BiPo channels. The result is shown in Figure 2.17.

The veto volume is parameterised by threshold parameters that attempt to find veto volumes with the highest probability content instead of using a simple time cut-off for how long to propagate the point cloud; that is, outlying points in a point cloud might be propagated for shorter amounts of time than points that are central to the point cloud. The extrapolation to XENONnT considers a constant integration time for each point cloud and is thus approximate. However, as can be seen in Figure 2.17, it fits XENON1T data quite well when fit simultaneously on both the $^{218}$Po and BiPo channels.
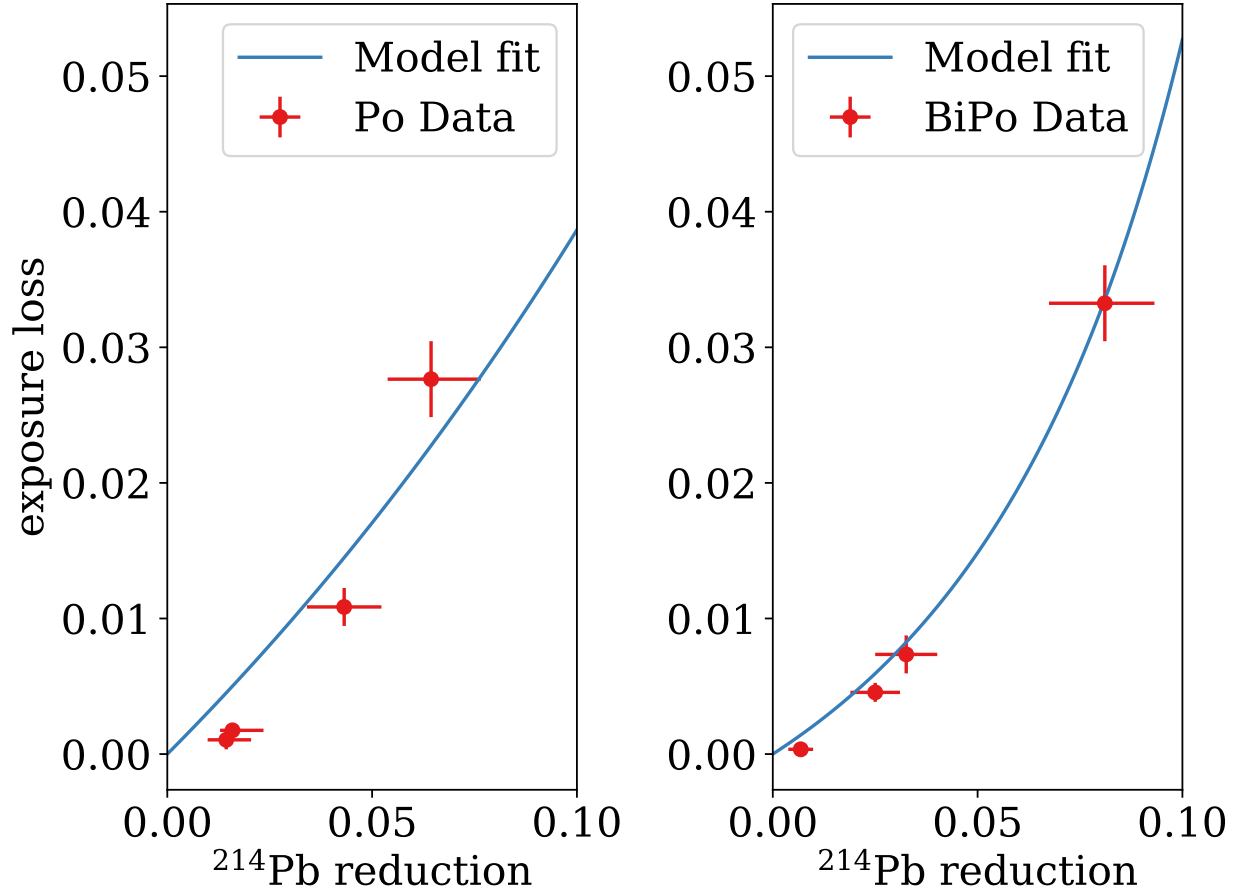
**Figure 2.17.** The exposure loss versus the $^{214}$Pb background reduction from the $^{218}$Po (left) and BiPo (right) channels. The left and right plots correspond to a simultaneous fit on both datasets; the reason why the curve looks different in the two plots is due to the different half lives, and the different probability of there being a correctly reconstructed $^{218}$Po alpha or BiPo event ($p_{\text{branch}}$).

To project the performance of the software radon veto in XENONnT, the fit parameters from above are kept the same, but the activities are scaled down. The $^{218}$Po activity in XENONnT is measured to be $1.691 \pm 0.006_{\text{stat}} \pm 0.072_{\text{sys}} \, \mu\text{Bq/kg}$, and the $^{214}$Pb activity is measured to be $1.31 \pm 0.17_{\text{stat}} \, \mu\text{Bq/kg}$ in XENONnT [81]. The ratio between $^{218}$Po and fully-reconstructed BiPo activities is kept the same from XENON1T. It should be noted that this is the XENONnT Science Run 0 radon level, and could be further lowered in future science runs depending on the mode of operation of the radon removal system [50]. Due to the lower $^{214}$Pb background, the fraction of the background attributed to $^{214}$Pb is estimated to be $\alpha = 0.5$ here. The projected performance for various convection speeds, optimised for normalised sensitivity as defined in Equation 2.5, is shown in Table 2.1. XENONnT is a larger detector than XENON1T; hence, due to considerations discussed in subsection 2.2.1 should be expected to have much lower convection speeds. However, we consider higher convection velocity conditions as well due to the introduction of liquid xenon recirculation, which may affect the convective flow in the TPC. As can be seen, due to the reduced radon level in XENONnT, the background reduction is improved greatly over XENON1T in all of the considered convection speed scenarios.

**Table 2.1.** Table showing the estimated optimal improvement in sensitivity $(Z_{\text{optim}} - 1)$, at various scenarios of convection speed $(v_{\text{convection}})$ in XENONnT, together with the reduction in $^{214}$Pb background $(1 - b_{Pb})$ and the exposure loss $(1 - s)$ at the stated optimal sensitivity improvement.

| $v_{\text{convection}}$ (cm/s) | $Z_{\text{optim}} - 1$ | $1 - b_{Pb}$ | $1 - s$ |
|---|---|---|---|
| 0.8 | 3.5% | 25% | 4.3% |
| 0.4 | 5.9% | 41% | 7.6% |
| 0.2 | 8.8% | 59% | 12% |
| 0.1 | 11% | 75% | 17% |

### 2.4.4 Projection of performance in diffusion-limited regime

As shown in subsection 2.2.3, for large dual-phase TPCs, such as LZ [72] and DARWIN/XLZD [37, 45], there might be insufficient heat flux to induce convection. In such a situation, the movement of daughter nuclides after a radioactive decay becomes dominated

by ion-drift [71]. It is noted in [71] that the measured diffusion constant is significantly larger than what one might expect from true diffusion of ions in liquid xenon, and that the measured diffusion likely represents the effect of small-scale fluid flow. It is thus unclear if a true diffusion-limited regime can be achieved in any planned noble-liquid TPCs. In this section, the performance of software tagging of radon-chain backgrounds under both scenarios is discussed. For simplicity, and because of the unknown effects of plate-out and BiPo reconstruction in future detectors, only the $^{218}$Po channel is considered here, resulting in a conservative estimate of the algorithm's performance.

A simple analytic model can be used to estimate the performance of software tagging in the true diffusion-limited regime. The probability density function of the displacement of a particle diffusing in one dimension is given by the 1D diffusion equation [82]

$$\frac{\partial \rho_x}{\partial t} = D \frac{\partial^2 \rho_x}{\partial x^2}. \tag{2.9}$$

Using the 1D diffusion equation leads to no loss of generality because the distribution of displacement of a diffusing point is independent in different orthogonal axes.

The solution to Equation 2.9 with an initial Dirac delta function, $\delta(x)$, corresponding to the known position of the original particle, is a normal distribution with $\mu = 0$ and $\sigma^2 = 2Dt$; in 3D, this corresponds to a spherical normal distribution with $\sigma_x = \sigma_y = \sigma_z = \sqrt{2Dt}$. It can be noted here that these are also the Green's function of the 1D and 3D heat equations, respectively, as the isotropic diffusion equation is the heat equation [83].

However, the veto volume cannot be directly determined from this normal distribution. This is because this distribution does not take into account the position reconstruction uncertainty. This has to be introduced twice, for both the candidate event that is being tagged, and for the alphas. The position reconstruction uncertainty will depend on the performance of future detectors. However, as the sum of normally-distributed random variables simply involves summing the variances, the expected performance can be expressed in terms of the position reconstruction uncertainties.

The veto volume $V(t)$, after time $t$, can then be given by the volume of an ellipsoid, where the semi-major axes are given by a multiple $n$ of the standard deviation:

$$V(t) \approx \frac{4}{3}\pi n^3 \left(\sigma_{\text{posrec,r}}^2 + 2Dt\right) \sqrt{\sigma_{\text{posrec,z}}^2 + 2Dt} \tag{2.10}$$

This multiple $n$ is a free parameter that determines the size of the veto volume, and hence controls the trade-off between background removal and exposure loss. A larger $n$ corresponds to a bigger veto volume, which would remove more background but also result in a greater loss of exposure.

The true diffusion constant can be estimated using Einstein's relation [84] and the mobility of $0.219 \pm 0.004 \,\text{cm}^2/(\text{kV s})$ as measured by EXO-200 [71]:

$$
\begin{aligned}
D &= \frac{\mu k_b T}{q} \\
&= \frac{k_b 0.219 \,\text{cm}^2/(\text{kV s}) 170 \,\text{K}}{q_e} \\
&\approx 3.2 \times 10^{-6} \,\text{cm}^2/\text{s}
\end{aligned}
\tag{2.11}
$$

With the diffusion constant shown in Equation 2.11, the daughter of a $^{218}$Po decay would diffuse approximately $\sqrt{3 \times 2 \times D \times (5 \times 27.06 \,\text{min})} \approx 0.4 \,\text{cm}$ in 5 half-lives. An activity of $1.7 \,\mu\text{Bq/kg}$ as achieved in XENONnT SR0 [81], and a liquid xenon density of $\sim 3 \,\text{g/cm}^3$ [40] corresponds to an activity per unit volume of $4.6 \times 10^{-9} \,\text{Bq/cm}^3$, or 0.4 decays per $10^3 \text{cm}^3$ per day. This implies that as long as the position reconstruction uncertainty remains significantly below $10 \,\text{cm}$, decays would be essentially spatially isolated without fluid flows, and hence one can reject radon-chain backgrounds with a tagging efficiency of near-unity.

The diffusion constant measured in EXO-200 was over 3 orders of magnitude larger. A more complex treatment is thus required. This can be done by first integrating the veto volume shown in Equation 2.10 as a function of time. The integrated veto volume and the $^{218}$Po activity can then be used to compute the false-positive rate of tagging ($p_{\text{coinc}}$) as a

function of time and $n$, the multiple of the standard deviation that scales the veto volume. This is shown in Equation 2.12 and Equation 2.13,

$$
\begin{aligned}
V_{ad}(t) =& \frac{4\pi n^3}{3D}(2Dt + \sigma_{\text{posrec,z}}^2)^{3/2} \times \\
& (6Dt + 5\sigma_{\text{posrec,r}}^2 - 2\sigma_{\text{posrec,z}}^2) \\
V_{int}(\tau) =& V_{ad}(\tau) - V_{ad}(0)
\end{aligned}
\tag{2.12}
$$

$$
p_{\text{coinc}}(\tau) = V_{int}(\tau)A_{vol}
\tag{2.13}
$$

where $V_{ad}(t)$ is the antiderivative of $V(t)$, $V_{int}(\tau) \equiv \int_0^\tau V(t)dt$, and $A_{vol}$ corresponds to the activity per unit volume. The true probability of matching $^{218}$Po and $^{214}$Pb is simply given by $n$ and $\tau$:

$$
p_{\text{true}}(\tau) = \chi_3^2\left(n^2\right)\left(1 - e^{-\lambda_{\text{decay}}\tau}\right)
\tag{2.14}
$$

where $\chi_3^2$ refers to the $\chi^2$-distribution with 3 degrees of freedom.

One can then use Equations (2.13) and (2.14), and the value of $D = 0.61 \pm 0.04\,\text{mm}^2/\text{s}$ measured in EXO-200 [71], to plot performance of a software radon veto for different values of the standard deviation multiple $n$ where the small-scale fluid motion is the same as EXO-200. The optimised performance is then defined by the best performance that can achieved by any $n$ at a given value of background reduction. These projections using $\sigma_{\text{posrec,z}} = 0.17\,\text{cm}$ and $\sigma_{\text{posrec,r}} = 1.5\,\text{cm}$, which is approximately the performance of the position reconstruction algorithms in XENON1T at $S2 \approx 500\,\text{PE}$, are shown in Figure 2.18.
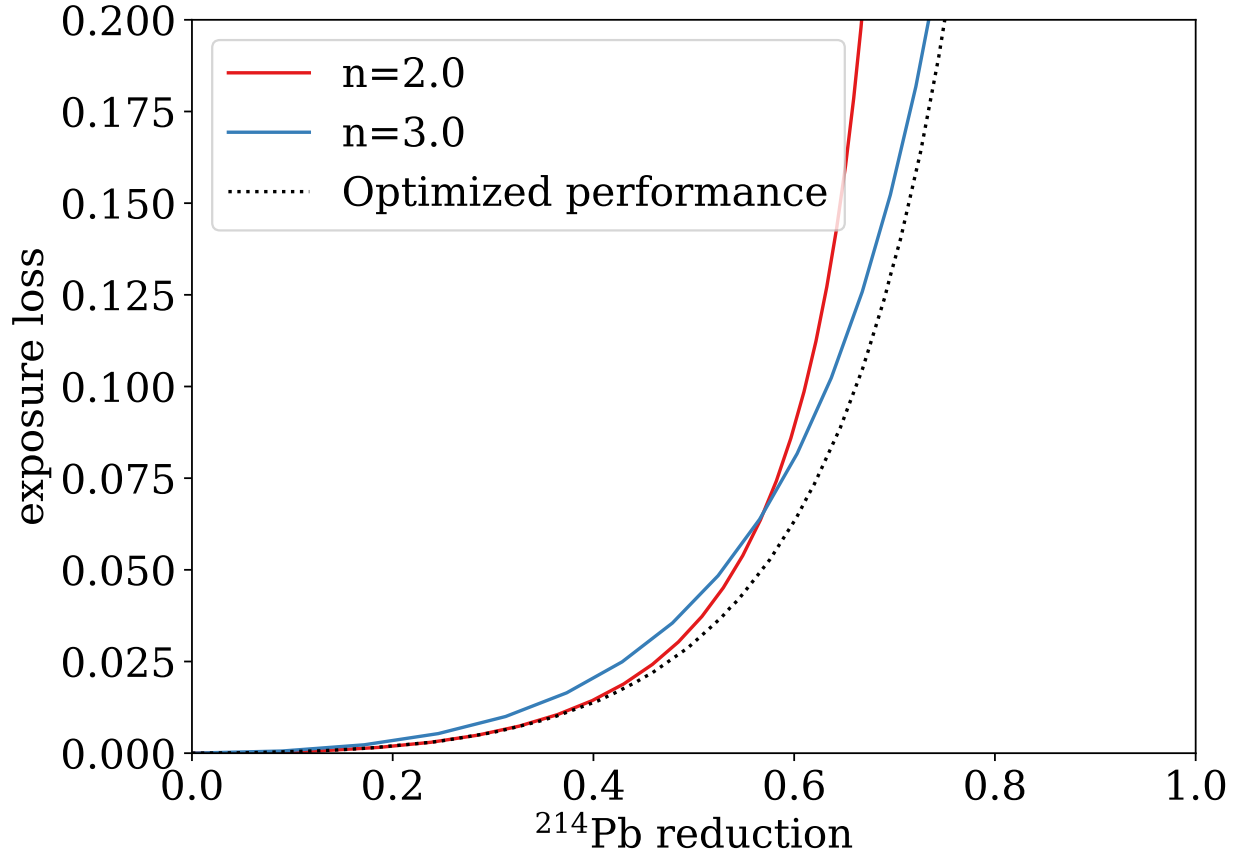
**Figure 2.18.** Exposure loss versus $^{214}$Pb background reduction, assuming motion can be modelled by diffusion with $D = 0.61\,\text{mm}^2/\text{s}$. The solid curves correspond to different values of standard deviation multiple $n$, which controls the size of the veto volume, and the optimised performance curve is obtained computing the curves for a large number of possible values of standard deviation multiple $n$ and then finding the lowest $p_{\text{coinc}}$ at a given $p_{\text{true}}$.

It can be seen that even in this regime, where the apparent diffusive motion is much larger than one expects for ions in liquid xenon, 75% of the radon-chain background can be removed with a 20% exposure reduction, even when only considering the $^{218}$Po channel. It should be noted that this estimate is based on a simplified model that does not take into account ion drift; though ion drift is deterministic, as not all radon daughters are charged [71], there may be some effect on the performance. In addition, this model assumes that small-scale fluid motion cannot be characterised and must be modelled diffusively. If this fluid motion is stable and a velocity field can be measured, higher performance can be achieved by propagating a point cloud through the velocity field, as described in section 2.3.

### 2.4.5    Application to $^{137}$Xe

The decay of cosmogenic $^{137}$Xe is expected to be a major background in the search for $0\nu\beta\beta$ decay in $^{136}$Xe in XENONnT [31], LZ [85], and next-generation liquid xenon TPCs [37]. $^{137}$Xe is largely produced due to the capture of muon-induced neutrons by $^{136}$Xe [31, 85], and subsequently undergoes beta-decay to $^{137}$Cs, as shown in Figure 2.19.
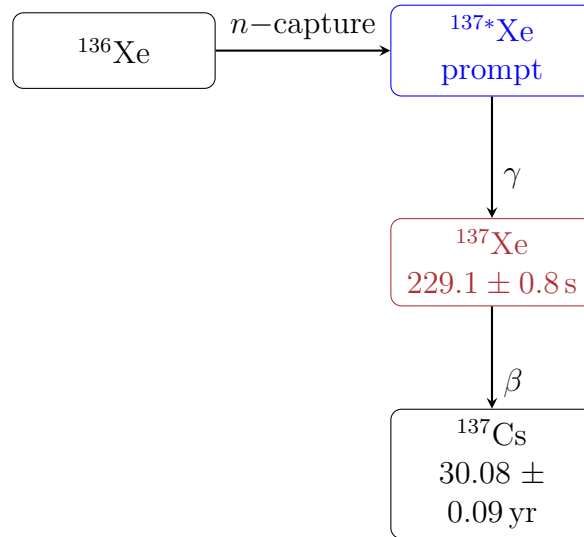


**Figure 2.19.** Neutron capture of $^{136}$Xe and subsequent decay of $^{137}$Xe. Data regarding the decay of $^{137}$Xe and $^{137}$Cs retrieved using the NNDC ENSDF, with original data from Nuclear Data Sheets [86]. The isotope the decays to produce the relevant background, $^{137}$Xe, is coloured red, whereas the excited state which produces the gamma events that are used for the tagging of the $^{137}$Xe background are coloured blue.

A similar methodology to subsection 2.4.3 can be used to estimate the performance of a $^{137}$Xe veto; however, this estimate is more speculative. This is because the performance of such a veto would rely on the reconstruction of neutron-capture gammas and a detailed analysis to search of these neutron-capture events has not been done in this study. These neutron-captures gammas represent the progenitor events. Point clouds generated at the position of $^{137}$Xe decay candidates are thus used to look for these neutron-capture events, which should appear as ER events that are coincident with muon veto triggers.

The relationship between $p_{\text{true}}$ and $p_{\text{coinc}}$ can be derived from Equation 2.8. However, the initial point cloud has to be much bigger, because the uncertainty on the true location of the neutron capture is not dominated by position reconstruction uncertainties, but by the mean-free-path of gammas. In the absence of a detailed analysis, the minimum attenuation between $10^{-2}$ MeV and $10^4$ MeV is conservatively applied. This is $0.036\,\text{cm}^2/\text{g}$ according to the XCOM database [87], corresponding to a maximum mean-free-path of $9.8\,\text{cm}$. Thus, to account for this, the fit parameter $C$ in Equation 2.8 which should scale with the initial point cloud size, is divided by the position reconstruction uncertainty volume, and multiplied by the volume of a sphere with a radius of $9.8\,\text{cm}$ in liquid xenon. Further, the half-life of $^{137}$Xe, which is $229.1 \pm 0.8\,\text{s}$ [86], is applied.

The activity rate $A$ is also different in this scenario. In XENONnT, the rate in the muon veto is observed to be $\approx 0.035\,\text{Hz}$. As the neutron capture time in liquid xenon is $\sim 100\,\mu\text{s}$ [88], a $1\,\text{ms}$ window after each muon trigger to search for neutron captures can be considered, leading to a livetime fraction of $3.5 \times 10^{-5}$ within which neutron captures would be searched for. The emitted gammas are expected to be of energies $\sim 1\,\text{MeV}$ [88] where $^{136}$Xe decay is the dominant background. Thus, the background rate can be approximated using the fraction found above, multiplied by the rate of $^{136}$Xe decays in natural xenon, $\approx 4.2\,\mu\text{Bq/kg}$ [31, 89], resulting in $A = 1.5 \times 10^{-4}\,\mu\text{Bq/kg}$. Using these values, the performance for different convection velocities is shown in Figure 2.20.

69
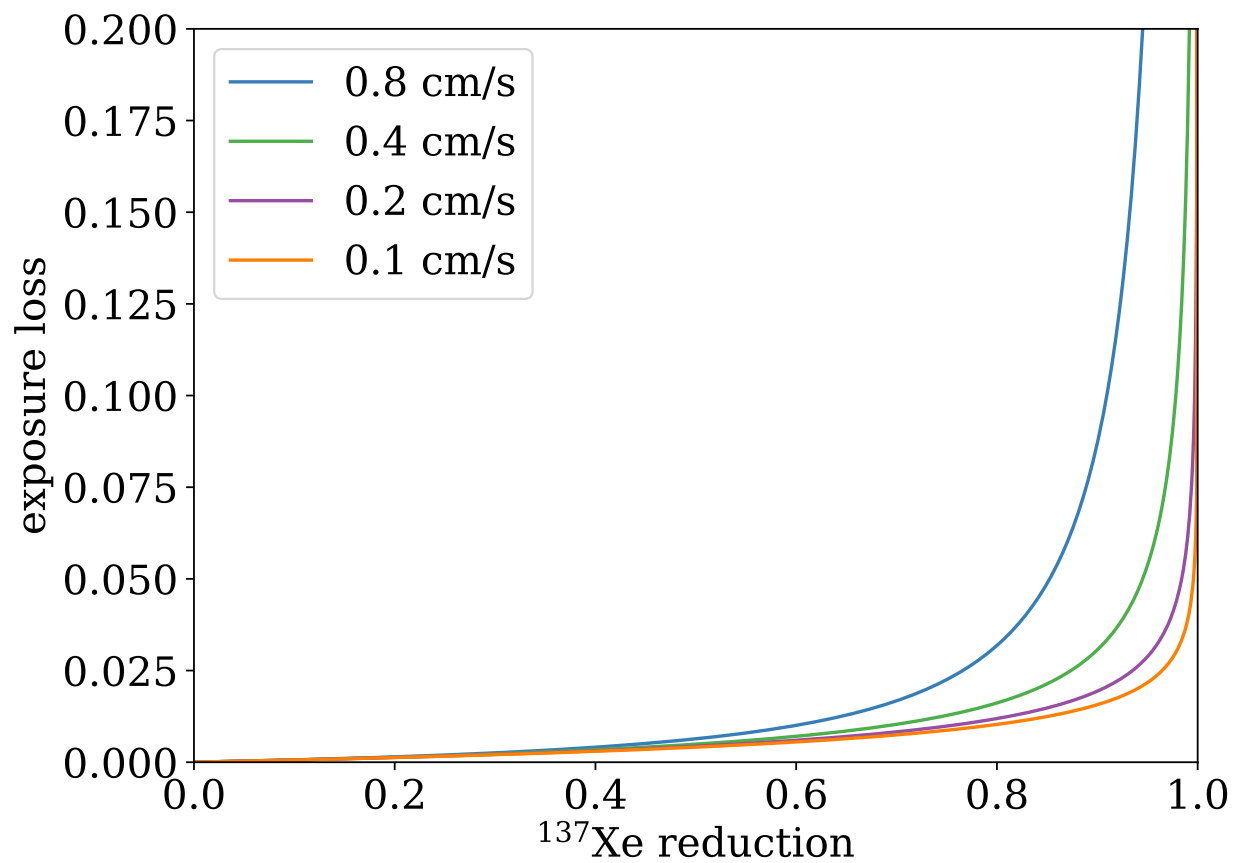
**Figure 2.20.** Projected exposure loss versus $^{137}$Xe background reduction when tagging $^{137}$Xe backgrounds for different scenarios of convection velocity.

It can be seen that for all of the velocity scenarios, almost all of the cosmogenic $^{137}$Xe background can be rejected. In particular, for convection velocities around or below $0.2\,\mathrm{cm/s}$, the reduction of the cosmogenic $^{137}$Xe background approaches unity for a 10% reduction in exposure. However, it should be noted that the selection efficiency of neutron-capture gammas has not been measured, and will proportionally reduce $p_\mathrm{true}$.

## 2.5   Conclusions

In this chapter, the design and performance of an algorithm for tagging radon-chain backgrounds in liquid noble element TPCs were presented. The presented algorithm performs tagging of the $^{214}$Pb background, which is part of the $^{222}$Rn decay chain. This was demonstrated on XENON1T datasets used for the low-energy ER search [35] and the search for neutrinoless double beta decay [31]. It was shown that for the low-energy ER search, an exposure loss of $1.8 \pm 0.2\%$ and a $6.2^{+0.4}_{-0.9}\%$ reduction in the $^{214}$Pb background can be expected. The neutrinoless double beta decay data set is used to produce a high-purity sample of $^{214}$Pb decay events, displaying relevant features in the spectrum such as the peak at $352\,\mathrm{keV}$ and falling off at the Q-value of approximately $1\,\mathrm{MeV}$.

While the demonstrated background reduction is small, the cost of such a software-based background-reduction technique can be minimal, making deployment cost-effective. In addition, much higher performance can be expected in larger detectors with lower intrinsic radon levels. In XENONnT due to the lower radon level, performance is expected to be significantly higher than in XENON1T, with an optimal $^{214}$Pb background reduction of between 25% and 75%, depending on the convection speed in the detector, with a corresponding exposure loss of between 3.5% and 11%. In future detectors where there is no significant convective motion, it was estimated that a 75% reduction in $^{214}$Pb background should be possible with a 20% exposure loss if there is small-scale fluid flow as measured in EXO-200 [71]. If the motion is dominated by diffusion, near-perfect tagging of radon chain backgrounds can be expected.

The fact that the performance of a software veto for $^{214}$Pb backgrounds improves with larger detectors and lower intrinsic radon levels makes it complementary to hardware-based

approaches such as the cryogenic distillation system used by XENONnT [50] or the charcoal trap used by LZ [53]. This is because as detector size increases, such hardware-based approaches require increasing mass flow rates to retain the same performance, whereas algorithmic approaches do not suffer from this scaling. In addition, software-based approaches perform better if the radon level is already low due to radiopurity controls or hardware-based radon removal methods; in the limiting case where there is on average much less than one $^{218}$Po in the TPC at any given time, there can simply be a veto on all data within a few half-lives of a $^{218}$Po alpha decay to remove almost all of the $^{214}$Pb background.

# 3. CALIBRATION OF LOW-ENERGY NUCLEAR RECOILS IN XENONNT USING A $^{88}$Y/BE PHOTO-NEUTRON SOURCE

## 3.1 Introduction

Searches for dark matter using liquid xenon TPCs are approaching exposures where one can observe coherent elastic neutrino-nuclear scattering (CE$\nu$NS), which mimic dark matter interactions. This 'neutrino fog' would present as a background for WIMP searches [90], and the neutrino fog due to $^8$B solar neutrinos is expected to be visible in XENONnT [39], whereas atmospheric neutrinos are expected to be visible in an even bigger issue in a next-generation liquid xenon experiment with exposures of $\sim 10^3$ tonne $\times$ year [37]. As neutrino and WIMP recoils are indistinguishable in direct detection experiments, searching for dark matter becomes much more challenging as one approaches the neutrino fog, requiring directional detectors or multiple target elements [91]. This does, however, present an opportunity to probe neutrino physics using dark matter detectors.

$^8$B solar neutrinos produce the neutrino signal that is dominant in the NR channel in XENONnT [39]. These neutrinos are produced due to positron emission of $^8$B. $^8$B forms from the proton capture of $^7$Be, itself a product of the fusion of $^3$He and $^4$He [92]. A measurement of $^8$B CE$\nu$NS events was attempted in XENON1T, however the resultant measurement was consistent with null (no-neutrinos) hypothesis. Due to the much larger exposure in XENONnT, a measurement of $^8$B CE$\nu$NS events is expected to be possible. Even if the exposure is large enough to enable a measurement, however, the large uncertainty in the light yield ($L_y$) and charge yield ($Q_y$) of liquid xenon would reduce the sensitivity to new physics such as non-standard neutrino interactions [93]. In this chapter, I outline work that aims to reduce the uncertainty in $L_y$ and $Q_y$ by calibrating the XENONnT TPC using a $^{88}$Y/Be photo-neutron source that produces 152 keV neutrons. In addition to enhancing the neutrino physics potential of XENONnT, this work also helps reduce systematic uncertainties for WIMP dark matter searches at low masses. This can be seen from fact that the $^8$B solar neutrino recoil spectrum is similar to that of a 6 GeV WIMP in liquid xenon [93].

### 3.1.1 Coherent Elastic Neutrino-nucleus Scattering

CE$\nu$NS refers to the coherent scattering of a neutrino off an atomic nucleus, as opposed to scattering with individual nucleons. This results in a coherence enhancement as the scattering amplitudes add constructively. The cross section thus scales approximately as the square of the number of neutrons in an atom [94]. This results in a cross-section that is enhanced by almost two orders of magnitude in heavy elements such as xenon compared to incoherent scattering where the cross section would simply scale linearly with target number. As such, much smaller xenon Dark Matter detectors can double as neutrino detectors despite having ton-scale targets, in contrast with dedicated experiments such as Borexino which has a 278 tonne target [95]. This effect was first proposed in the 1970s [96], however the first detection only occurred recently in 2017 [97]. This is due to the fact that the coherent scattering cross section depends on the form factor [94], which drops off rapidly as momentum transfer exceeds 30 MeV for heavy nuclei such as xenon [98]. To detect coherent scattering of neutrinos, then, a detector has to be able to detect events with recoil energies on the order of keVs. As with WIMP detection, a low detector threshold is required for the observation of CE$\nu$NS events; in addition, the threshold needs to be well-characterised so as to enable an accurate measurement of neutrino rates. The detection of solar $^8$B neutrinos is particularly sensitive to the threshold of the xenon detector because the recoil spectrum rolls off close to the energy threshold of detectors such as XENON1T [29, 99]. This makes calibration even more crucial, as any mismodelling of the detector near the threshold would have a large impact on a measurement of the neutrino rate.

In addition, the 152 keV neutron recoil spectrum has a similar endpoint as the spectrum from $^8$B solar neutrinos. This can be seen by noting the reduced mass of the neutron-xenon-nucleus system is approximately $131 m_N/(1 + 131) \approx m_N$. Because of this, the maximum

recoil momentum transfer can be estimated to be approximately twice the momentum of an incoming neutron, and the maximum recoil energy is thus:

$$
\begin{aligned}
E_{\text{max}} &= \frac{(2p_N)^2}{2m_{\text{Xe}}} \\
&\approx \frac{2p_N^2}{131m_N} \\
&\approx \frac{4 \times 152 \, \text{keV} \, m_N}{131m_N} \\
&\approx 4.6 \, \text{keV}
\end{aligned}
\tag{3.1}
$$

This is comparable to the $\approx 4 \, \text{keV}$ endpoint of the $^8$B solar neutrino recoil spectrum in xenon-based detectors [99]. Thus, a $^{88}$Y/Be photo-neutron is uniquely suitable for the calibration of a liquid xenon TPC for the detection of $^8$B solar neutrinos. A comparison of the recoil spectrum from 6 GeV WIMPs, $^8$B solar neutrinos, and $^{88}$Y/Be photo-neutrons is shown in Figure 3.1.

## 3.2 Simulation-driven Optimisation of the $^{88}$Y/Be Photo-neutron Source

The $^{88}$Y/Be photo-neutron source calibration uses the 1.84 MeV $\gamma$-emission from $^{88}$Y produce nearly-mono-energetic 152 keV neutrons via photo-disintegration of $^9$Be [101, 102]. This calibration is very challenging as the recoil spectrum is very close to the threshold of XENONnT, and there is a high gamma rate due to the photo-disintegration cross section of around 0.65 mb. The neutron rate is approximately $\sim (0.65 \, \text{mb}) \times (1 \, \text{cm}) \times (1.2 \times 10^{23} \, \text{cm}^{-3}) \approx 10^{-4}$ times that of the gamma rate for a centimetre-scale source, where $1.2 \times 10^{23} \, \text{cm}^{-3}$ is the atomic number density of $^9$Be. This poses a problem for liquid xenon TPCs, both because these detectors are relatively slow due to the drift time of electrons in liquid xenon making pileup an issue with high rates [103], and because discrimination between gammas and nuclear recoils (NRs) is imperfect [28, 29]. The solution is thus to use a high-Z material to construct a gamma shield. Due to scattering kinematics, neutrons scattering off of such a heavy nucleus, such as tungsten or lead, loses very little energy, whereas the high density of electrons would make for an effective gamma shield.
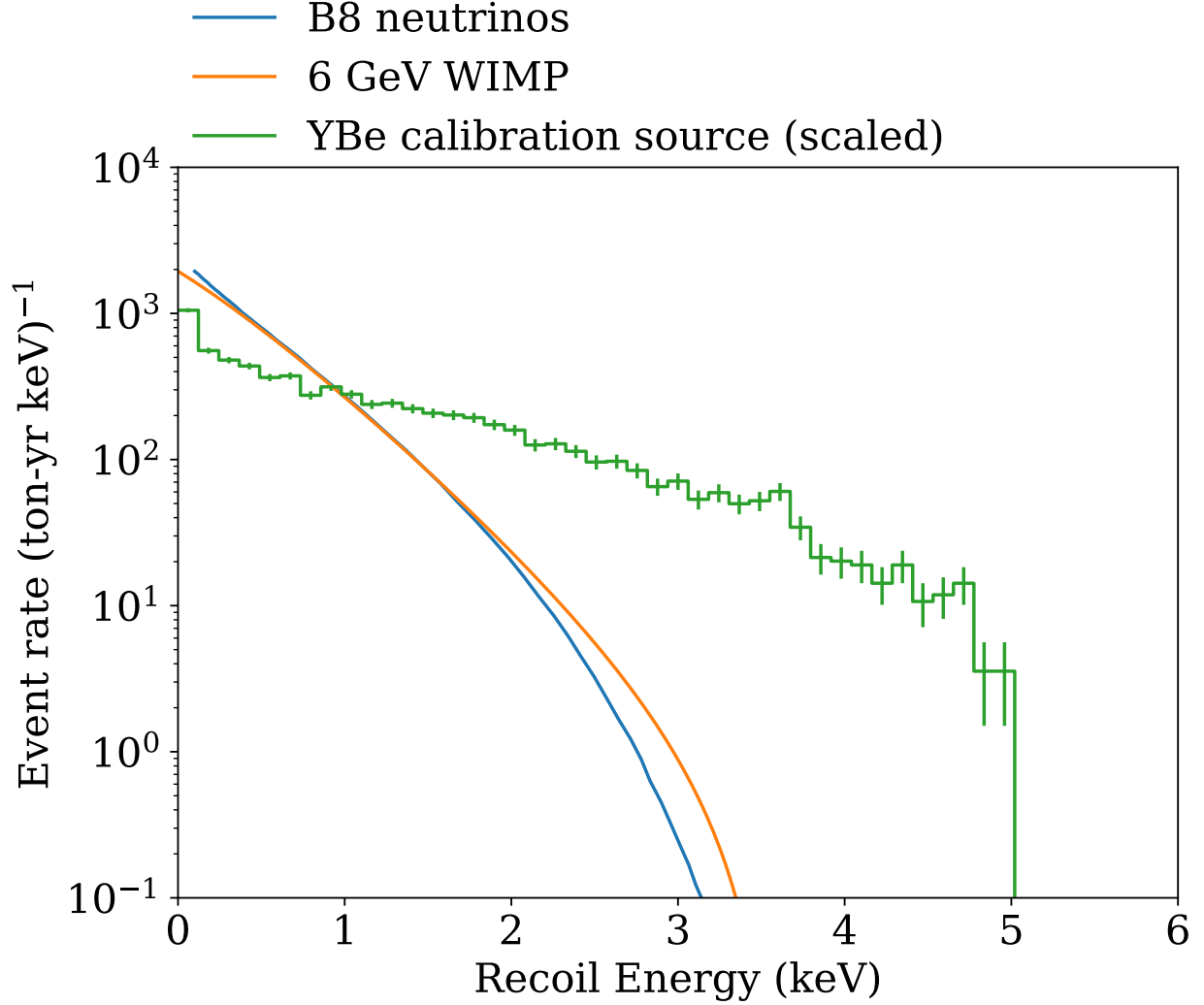
**Figure 3.1.** The recoil spectrum from $6\,\text{GeV}$ WIMPs [100] (orange), $^8$B solar neutrinos [99] (blue), and $152\,\text{keV}$ neutrons from the $^{88}$Y/Be neutron source (green). The neutron spectrum is scaled to be comparable on the same y-axis. The WIMP spectrum corresponds to the spectrum from WIMPs scattering via spin-independent interactions with a cross section of $5 \times 10^{-45}\,\text{cm}^2$. The neutron recoil spectrum is produced using GEANT4 simulations, corresponding to the $50\,\text{mm}$ curve in Figure 3.4, and will be described in more detail in section 3.2.

As XENONnT inherits many sub-systems from the XENON1T detector, the physical size of the shield is restricted by the existing I-Belt system, described in [27], to a $16\,\text{cm}^3$ cube. This I-Belt system uses a timing belt to lower a calibration source into place when needed, and allows for the calibration source to be lifted out of the water tank remotely via the SCADA system [27], and was constructed at Purdue before my involvement in the group. The XENONnT cryostat and I-Belt assembly can be seen in Figure 3.2. As the cryostat and calibration systems are in the water-filled neutron veto, a stainless steel box that displaces water between the cryostat and the calibration source was manufactured and installed for this calibration to reduce scattering of the neutrons from the calibration source. With the water displacement box installed, there is $\approx 1\,\text{cm}$ of water remaining between the front of the tungsten shield and the box to ensure mechanical clearance of the tungsten shield when passing in front of the TPC.
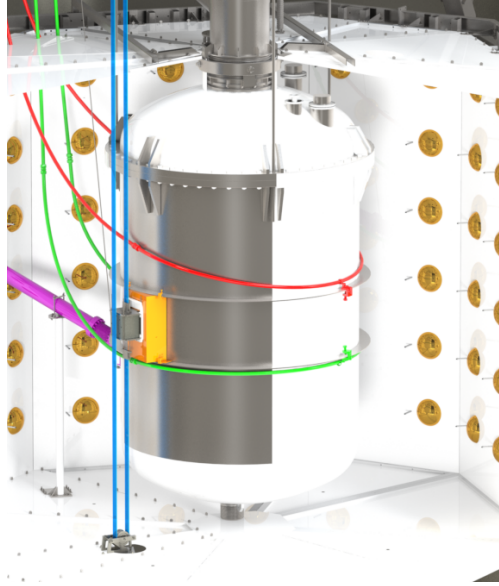


**Figure 3.2.** Render of the XENONnT cryostat and external calibration systems. The relevant I-Belt assembly is visible as a grey block suspended by the I-Belt (blue). In yellow is a stainless steel box that displaces water between the calibration source and the cryostat. Image credit: Jacques Pienaar

Because of the aforementioned constraints on the physical size, the calibration system needs to be designed to make optimal use of the compact space. First, the shield is constructed out of tungsten alloy, instead of lead which was used in [101]. Second, beryllium metal is

used as opposed to beryllium oxide to make the source assembly more compact. Finally, the geometry of the source assembly containing the gamma source and the beryllium is optimised by simulating the calibration using the GEANT4 toolkit [104] while varying the geometry parametrically to find the optimal shape. This is done using the XENON1T MC framework [105], updated with XENONnT geometry. A top-down view of the GEANT4 geometry to be optimised is shown in Figure 3.3.

Due to the $\approx 10^4$ ratio between gamma rays and neutrons, simulating the $^{88}$Y/Be directly in GEANT4 is extremely computationally intensive. Instead, separate simulations are done to characterise the rate of events in the XENONnT TPC due to gamma rays and neutrons. The gamma rate is characterised using a GEANT4 simulation where the active element, indicated in orange in Figure 3.3, generates $1.84\,\mathrm{MeV}$ $\gamma$-emission. To characterise the neutron rate, on the other hand, the beryllium, indicated in red in Figure 3.3, is used as a monoenergetic $152\,\mathrm{keV}$ neutron source. It should be noted that this assumes that the $^9\mathrm{Be}(\gamma, n)$ reaction is isotropic, which is not true in general but is indeed observed to be the case for gamma energies of $\approx 1.8\,\mathrm{MeV}$ [106].

I then converted the GEANT4 output, which is a list of individual scatters, into detected events in the TPC using the `nSort` framework developed by the XENON collaboration. The `nSort` framework first computes the energy deposited in the active liquid xenon volume into photons and electrons, and then into S1 and S2 signals, taking into account the light and charge yields and detector efficiencies [105]. S1s and S2s that are close in time and position are then clustered, as they will not be distinguishable in the TPC [107].

The figure-of-merit used for geometry optimisation is the ratio of the nuclear recoil single-scatter (NRSS) event rate under $5\,\mathrm{keV}$ within a fiducial volume to the total rate of events in the TPC. The fiducial volume contains $\approx 4\,\mathrm{tonnes}$ of liquid xenon, and is defined by the following superellipse:

$$\left|\frac{z + 739}{629}\right|^3 + \left|\frac{x^2 + y^2}{630^2}\right|^3 < 1 \tag{3.2}$$

78
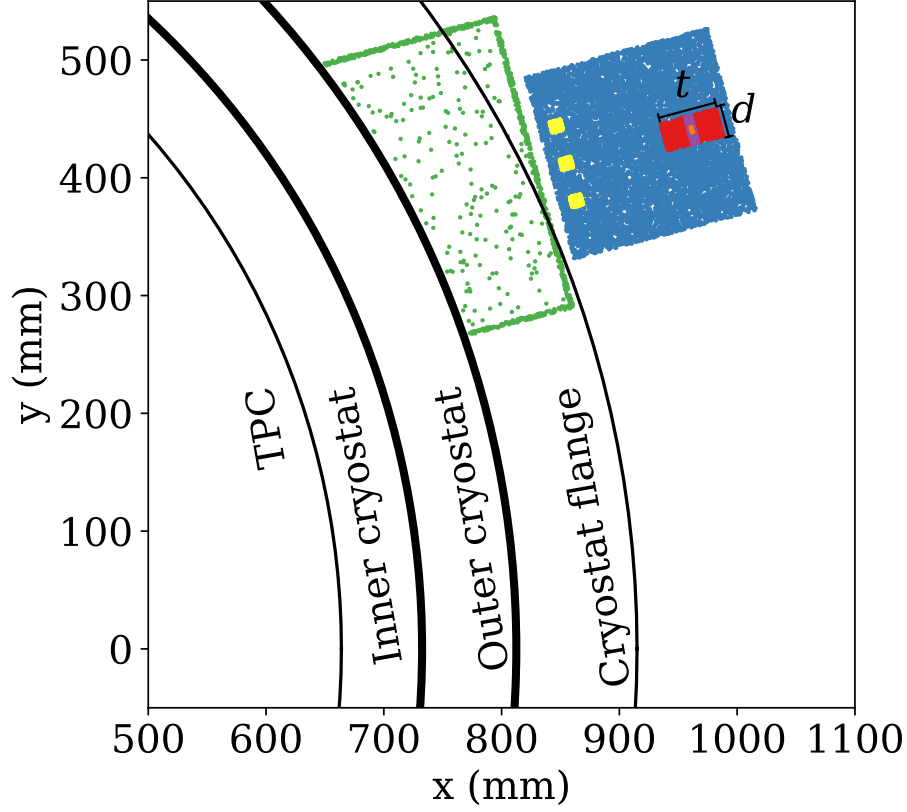
**Figure 3.3.** Calibration source and detector geometry indicated in GEANT4 model. The black lines indicate the position of the calibration system relative to the TPC and cryostat as indicated, and the thickness of the cryostat hulls (5 mm) is indicated by the width of the lines. The cryostat flange has to be cleared by the calibration source as it is lowered down into position, and can be seen near the top of the cryostat in Figure 3.2. Green indicates the stainless steel displacement box. Blue represents tungsten, yellow indicates air holes that exist due to the manufacturing process of the tungsten shield, red represents beryllium, purple indicates the acrylic disc that the gamma source is made of, and the small orange point indicates the gamma point source. The geometric parameters being optimised are the diameter ($d$) and thickness ($t$) of the cavity in the tungsten block that houses the beryllium target and $^{88}$Y source.

This ratio is chosen because the absolute NRSS rate can be increased by simply using a hotter gamma source; instead, the total rate of the TPC is limited by the XENONnT data acquisition system [108], and hence the proportion of events that are NRSS would determine the final rate of useful calibration events in the TPC. In addition, no lower energy threshold is used for this optimisation, because I found that varying the geometry of the source assembly did not affect the spectral shape significantly. This can be seen from Figure 3.4.
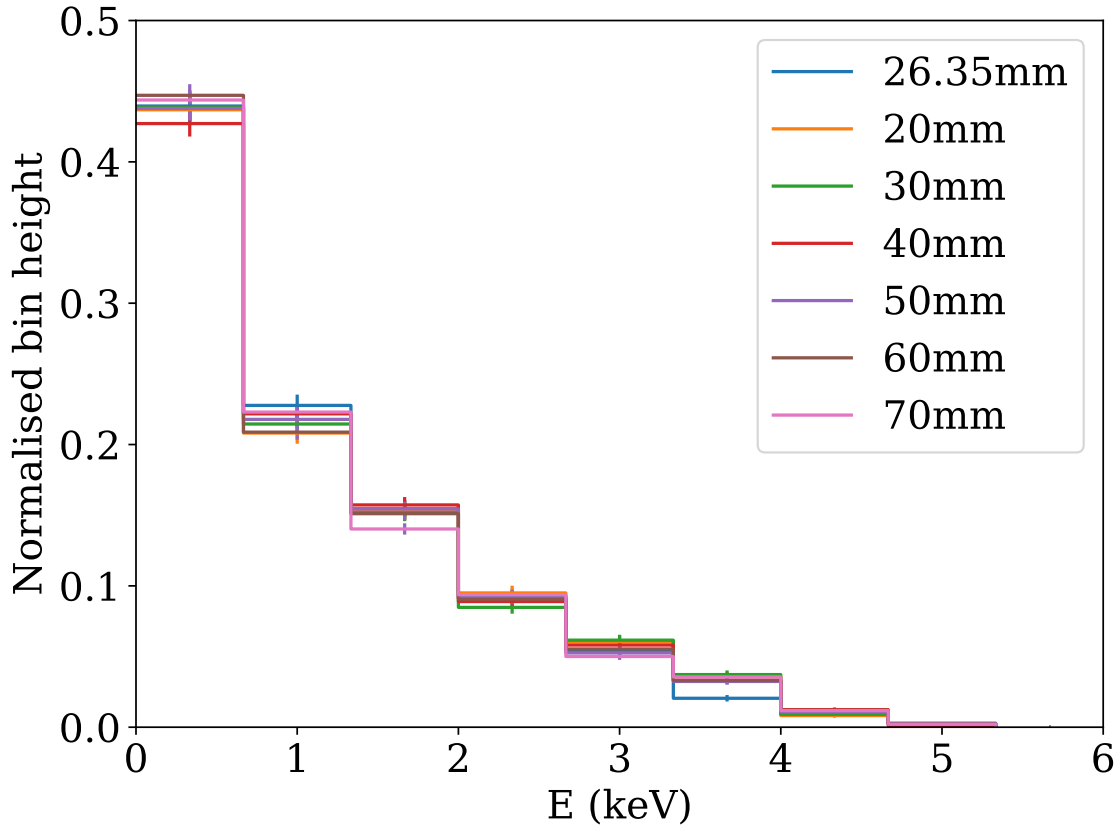


**Figure 3.4.** Spectrum of nuclear recoil single scatter events from GEANT4 simulation for various values of thickness. It can be seen that the spectrum for different thicknesses agree within statistical uncertainty.

To compute this figure of merit from the simulated events, the ratio between the neutron and gamma activities $p_{\gamma,n}$ is needed. This is computed using a separate Monte Carlo simulation in Python, where $10^5$ rays are simulated from a small cylindrical active source, and the probability of a ${}^9\mathrm{Be}(\gamma, n)$ interaction for each ray is computed based on the length

of the ray in the beryllium target. The random direction of the gamma rays is generated by sampling from a unit 3D Gaussian distribution, then normalising the vector to 1; this works because the unit Gaussian distribution is symmetric. The total expected number of interactions is then computed by simply adding all the probabilities, and from that, the average probability of a $^9\mathrm{Be}(\gamma, n)$ interaction can be computed by dividing the total expected number of interactions by $10^5$. This is done for each geometric configuration considered, as this ratio varies based on the size of the beryllium targets. The geometry of one such simulation is shown in Figure 3.5.
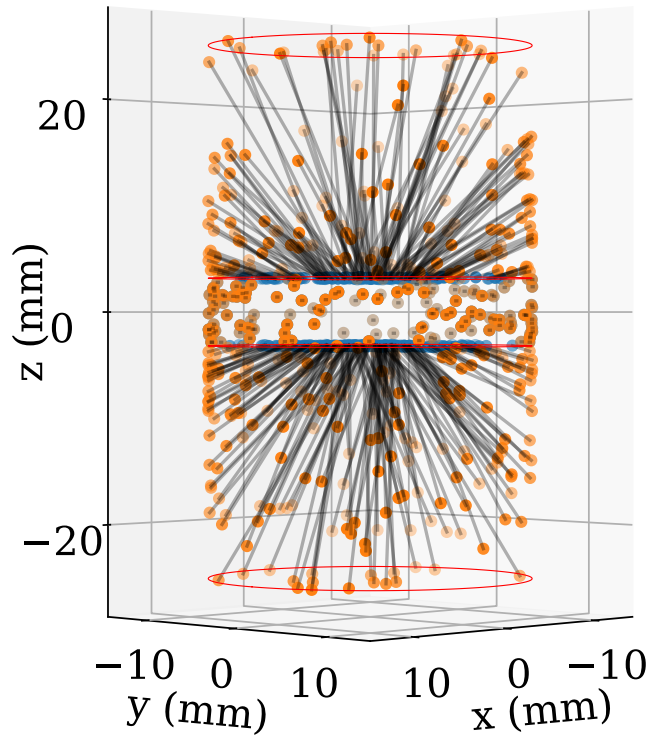


**Figure 3.5.** Geometry of the Monte Carlo simulation used to compute the ratio of the neutron to gamma activities. The individual rays are indicated by black lines, and the start and end point of each ray in the beryllium target is indicated by the blue and orange points respectively. The positions of the cylindrical beryllium targets are indicated by red lines.

Naively, the figure of merit is then simply the rate of NRSS events divided by the total event rate in the TPC. However, this does not account for that fact that the gamma flux is higher closer to the active element of the $^{88}$Y source due to the inverse-square law, making $^{9}$Be$(\gamma, n)$ interactions more likely to be close to the source. To address this, instead of computing the rate from neutron primaries simply by counting the number of events in the TPC, a weight based on the inverse-square law is applied to each event. This assumes beryllium is transparent to gamma radiation, which is a good approximation as the radiation length is 35 cm [2], much larger than the geometries being considered. The active element of the $^{88}$Y source is also approximated as a point source here, which is a good approximation as we were modelling this design based on a disc source with an active element of 5 mm diameter and 3 mm height, much smaller than the beryllium assembly. The weight is computed as follows:

$$w_i = \frac{\mathcal{N}}{r_i^2} \tag{3.3}$$

where $r_i$ is the distance from the source to the location in the beryllium at which the event originated, and $\mathcal{N}$ is a normalisation constant. It is defined based on the average $\frac{1}{r^2}$ value for a set of uniformly distributed points in the beryllium target, and is hence simply a function of the beryllium target geometry:

$$\mathcal{N} = \left\langle \frac{1}{r_j^2} \right\rangle^{-1} \tag{3.4}$$

The weighted total number of events thus:

$$N_{\mathrm{NRSS}} = \sum_i^N w_i \tag{3.5}$$

The uncertainty on the weighted total number of events is computed using the standard error of a weighted sum, using the Gaussian approximation:

$$
\begin{aligned}
\sigma_{\mathrm{NRSS}} &= \sqrt{\sum_i^N w_i^2 \sigma_i^2} \\
&\approx \sqrt{\sum_i^N w_i^2}
\end{aligned}
\tag{3.6}
$$

The reason Equation 3.6 works is because each weight represents a single event, thus under the Gaussian approximation, $\sigma_i = 1$. The figure-of-merit can then be computed by dividing the weighted total number of NRSS events and the total number of events by the effective exposure, computed using the number of simulated neutrons ($S_n$) and gammas ($S_\gamma$) in GEANT4 and the ratio between the neutron and gamma activities. This is given by:

$$\text{FOM} = \frac{p_{\gamma,n} N_{\text{NRSS}}/S_n}{p_{\gamma,n} N_n/S_n + N_\gamma/S_\gamma} \tag{3.7}$$

The figure of merit shown in Equation 3.7 can then be used to determine the performance of the $^{88}$Y/Be photo-neutron source. Because of the computational expense of GEANT4 simulations, a full 2D optimisation is not explored; instead, the thickness of the source assembly is optimised while setting $d = 40$ mm first. Following that, the diameter is optimised while setting $t = 50$ mm. This is shown in Figure 3.6.

It can be seen that the figure of merit is maximised at a thickness of $t = 60$ mm and $d = 25.4$ mm. There are no data points with diameter below 25.4 mm or 1 inch, because that is the diameter of the disc source. The final geometry is chosen to be $t = 50$ mm and $d = 25.4$ mm. This is because the performance only changes minimally between $t = 50$ mm and $t = 60$ mm; as additional material needs to be removed in the tungsten to accommodate machining tolerances and a capsule to contain the source assembly, a slightly smaller than optimal design was chosen to be conservative in terms of material removal in the tungsten shield. A final GEANT4 simulation was performed with the final geometry. The figure of merit is FOM $= (6.3\pm0.1)\times10^{-4}$, higher than all other considered designs shown in Figure 3.6. After this optimisation process, a stainless steel capsule of approximately 2 mm thickness on all sides, and with a screw-on cap of approximately 3 mm was machined to contain the $t = 50$ mm by $d = 25.4$ mm neutron source. The source assembly including the stainless steel capsule has dimensions of $t = 55.5$ mm by $d = 29.4$ mm.
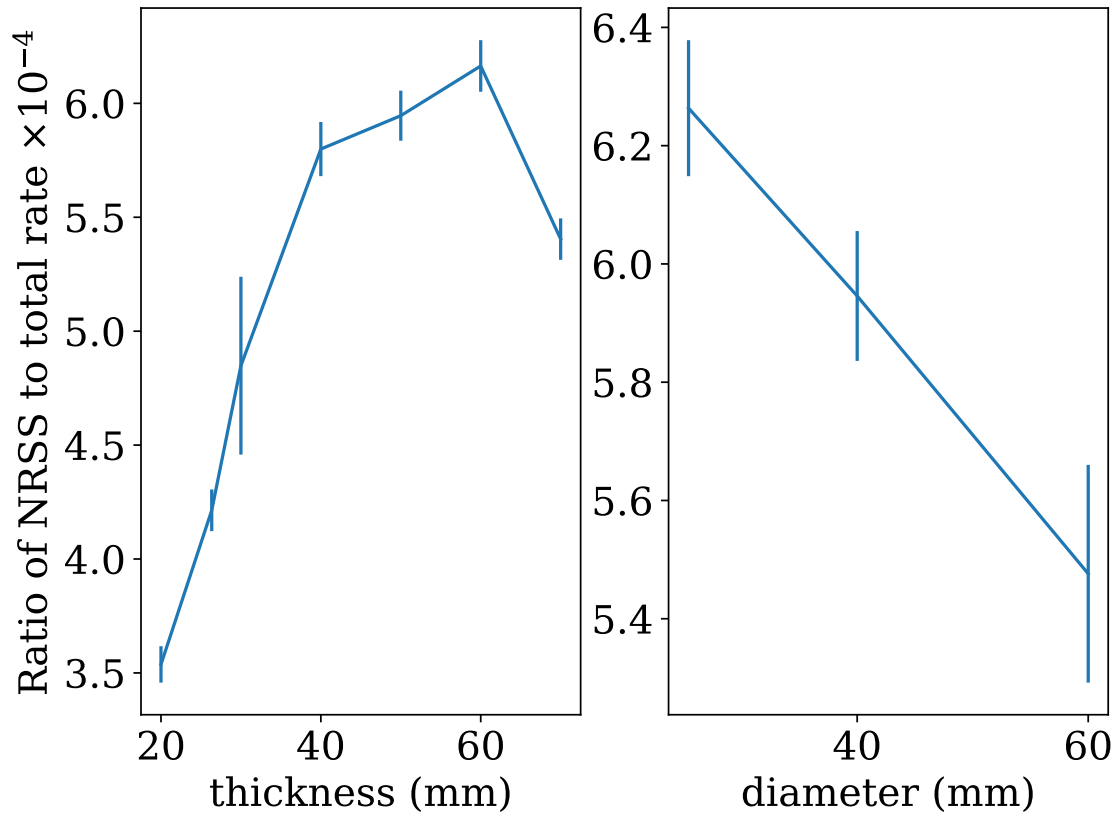
**Figure 3.6.** Figure of merit for the $^{88}$Y/Be photo-neutron source. The thickness of the source assembly is varied at constant $40\,\mathrm{mm}$ diameter to produce the plot of the figure of merit versus thickness (left), and the diameter is varied at constant $50\,\mathrm{mm}$ thickness to produce the plot of the figure of merit versus diameter (right).

## 3.3 XENONnT Calibration Using the $^{88}$Y/Be Photo-neutron Source

XENONnT calibration data using the $^{88}$Y/Be source was acquired in late 2022. In addition to using the $^{88}$Y/Be source in the configuration described in section 3.2, another configuration where the beryllium elements are removed and swapped out for PVC. This $^{88}$Y/PVC data is used to measure the background in the TPC coming from the $^{88}$Y gamma source in the absence of neutrons produced by the beryllium target. In total, 183.78 hours of data was taken in the $^{88}$Y/Be configuration, and 142.21 hours of data was taken in the $^{88}$Y/PVC configuration. Data-analysis is still ongoing, but a preliminary view of the data is shown in Figure 3.7.

In addition to the increased rate in the $^{88}$Y/Be data compared to the $^{88}$Y/PVC data, a difference in the corrected S2 spectra can be clearly seen. This clearly demonstrates the presence of neutron events in the acquired data. The remaining analysis work will be carried out by collaborators in the XENON collaboration, and will focus on measuring the light and charge yields of the XENONnT detector at these low energies.

## 3.4 Conclusion

The $^{88}$Y/Be photo-neutron source was designed and constructed for the calibration of the XENONnT detector. The source was designed to maximise ratio of neutron events to overall rate in the PC as much as possible given the physical constraints of the I-Belt system. This source was then used to take calibration data for the XENONnT detector. Compared with a run where the neutron-generating beryllium targets are removed, it can be clearly observed that there is an excess in the TPC caused by neutron events. The goal of this calibration is to measure the NR light and charge yields of the XENONnT detector, and the results of this calibration are still being analysed. I expect this measurement to strongly constrain our detector response to nuclear recoils below 5 keV and hence to help enable a measurement of $^8$B solar neutrinos via CE$\nu$NS. In addition, such a calibration of the detector response close to the threshold will also aid in the search for WIMP dark matter.
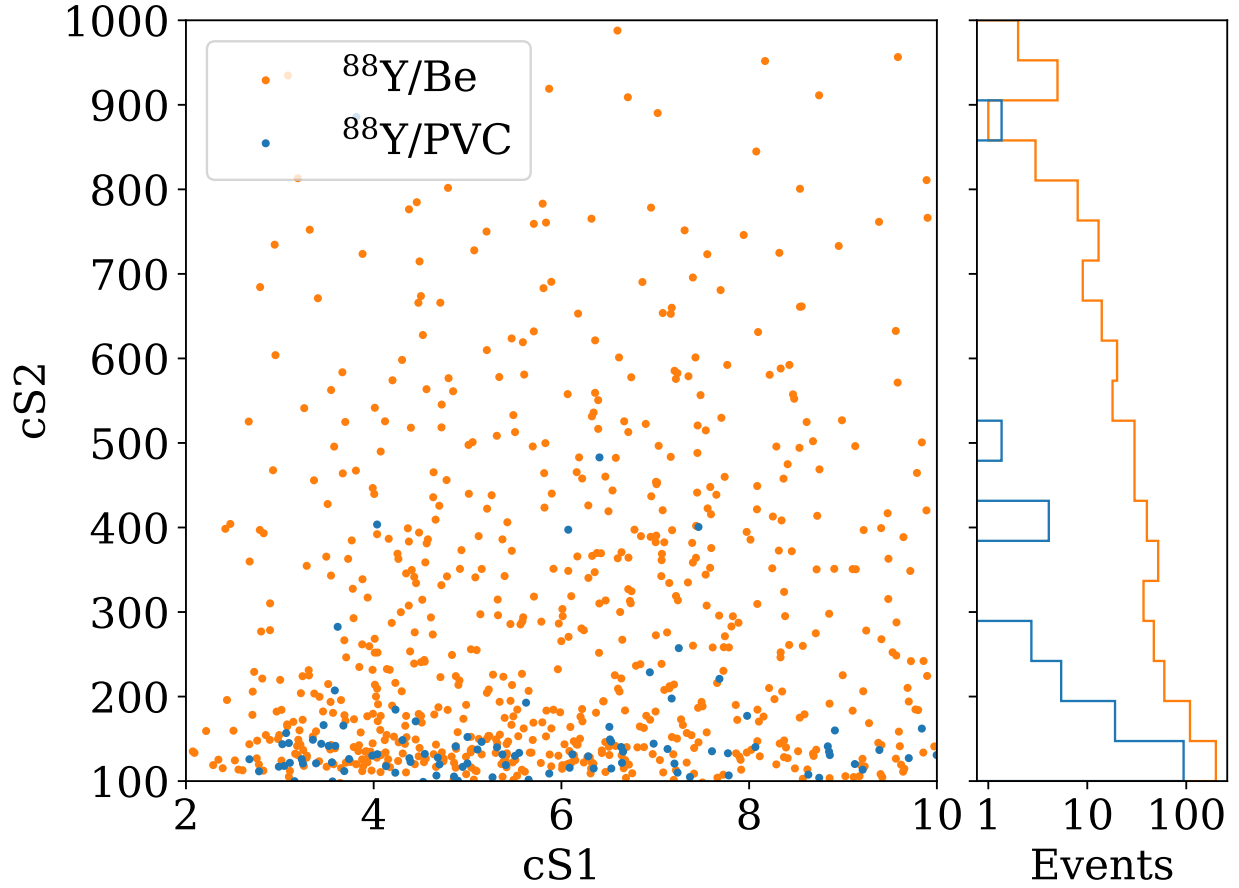
**Figure 3.7.** Preliminary view of the [88]Y/Be and [88]Y/PVC data shown in corrected S1 (cS1) versus corrected S2 (cS2) space. The [88]Y/Be data is shown in orange, and the [88]Y/PVC data is shown in blue. It can be seen clearly that there is an excess of events in the [88]Y/Be data corresponding to the neutrons from this calibration. In the histogram on the right, the [88]Y/PVC data is normalised to account for the reduced data-taking time and 8 days of decay of the [88]Y source.

# 4. METHODS FOR DATA ANALYSIS AND SENSITIVITY PROJECTIONS FOR THE WINDCHIME PROJECT

## 4.1 Introduction

An accelerometer array that has sensitivity to the gravitational interactions of ultra-heavy dark matter might comprise up to $\sim 10^9$ sensors [23]. This corresponds to an array that is 1 order of magnitude larger than the CMS Phase-1 pixel detector [109], and hence will likely necessitate a hardware trigger system to reduce the data rate. Some options for such a trigger system include template matching on individual sensors, where data is read out when a there is a coincident signal between multiple co-linear sensors. While this is a major technical challenge, detailed discussion of such a trigger is not the focus of this thesis.

One key issue of such a large sensor array is that sensitivity projections for the Windchime project are computationally challenging, and direct simulation of the sensitivity to dark matter tracks is not possible without dedicated hardware infrastructure. In addition, unlike in typical tracking detectors, such as ATLAS [110] and CMS [111] where tracks are reconstructed using sensor hits, our tracks are likely to lie below the noise floor for individual sensors, and the signal from multiple sensors would have to be combined to obtain statistically significant impulses. As we are interested in long-range forces, including sensors that do not exactly intersect the track would also boost the statistical significance. This complicates sensitivity projections for future experiments that have to be made before the existence of such dedicated hardware infrastructure, because the sensitivity of an array is higher than the sensitivity of a single sensor with increased dark matter flux. As such, in section 4.2, I will discuss some computationally tractable methods for sensitivity projections of such large sensor arrays. That dark matter tracks are likely to lie below the noise floor for individual sensors is also a key issue for the analysis of data from such a sensor array, necessitating statistical track-finding methods that can combine the signal from multiple sensors.

Given the above considerations, data from a Windchime array can be analysed either using template matching or Bayesian inference. In the context of rare-event searches, estimating the

false alarm rate for a given detection threshold is crucial. While estimating the look-elsewhere effect correction needed to determine the false alarm rate can be computationally challenging, it is conceptually simple when a frequentist method such as template matching is used. Thus, frequentist approaches are often used when dealing with rare events, such as by LIGO [112] and SNEWS 2.0 [113]. The look-elsewhere effect will be considered separately in chapter 5, where it will be shown that for many statistical problems, computation of the look-elsewhere effect correction can be simplified using the formalism of random fields.

Even though the look-elsewhere effect has frequentist conceptual roots, it is indeed possible to estimate the look-elsewhere effect correction using Bayesian methods by considering the frequentist properties of Bayesian estimators [114], and this will also be explored to produce an independent estimate of the threshold needed for a reasonable false alarm rate. Bayesian methods are also conceptually easier to understand for parameter inference. As such, we believe that frequentist and Bayesian methods are complementary for Windchime, and these strategies will be explored in section 4.3 and section 4.4, respectively.

### 4.1.1 The Natural Parameter Space for Ultra-heavy Dark Matter Searches

Template matching, or matched filtering, is a natural and well-established way to find signals in time-series data, and is used successfully in experiments such LIGO [112, 115] and CDMSlite [116]. However, for the Windchime project, template matching in individual sensors is not optimal. There can be improved noise rejection from considering specific track-like correlations in the whole array. One simple approach could be the use of an X-ray transform, an integral transform closely related to the radon transform with applications in X-ray tomography [117]. This integral transform considers the space of all lines on a manifold, in our case simply the volume given by the sensor array. This still presents some issues, however. One major issue is that the speed distribution of dark matter is expected to peak at approximately $300\,\text{km/s}$ [43]. This means our tracks would be relatively slow–$\sim 10^{-6}\,\text{s}$ long for a metre-scale experiment. This is much longer than the required integration time for sensors to be capable of detecting ultra-heavy dark matter gravitationally, which is $\sim 10^{-8}\,\text{s}$ [23]. This means that a simple X-ray transform for each set of data-points at a

given time would not be sufficient, for tracks would span numerous time bins. The signal strength for a given track also varies even among sensors that are co-linear, as the signal strength varies depending on closest approach of a track to the sensor; an X-ray transform that weighs all data points along a line equally would thus be suboptimal.

Instead, we can consider template matching in the space of all tracks. This space can be parameterised by considering a sphere that bounds the sensor array. Every track can then be parameterised by considering the position and time of two points of a track that intersects this sphere. The parameter space is thus 6-dimensional, with one time dimension and two spatial dimensions for each of the two points. The spatial dimensions can be concretely parameterised using spherical coordinates.

## 4.2   Fast Sensitivity Projections for the Windchime Project

To reduce the computational burden of estimating the sensitivity of a large sensor array to ultra-heavy dark matter, we can use a semi-analytical method where the signal from a single sensor is expressed as a function of impact parameter, and the individual signals are summed up in code. The procedure is as follows:

1. A sensor array is generated based on configuration parameters. In this work, all sensors are assumed to be pointing in the same direction, though in the future we would like to evaluate the impact of various sensor orientations.

2. $N_{\text{tracks}}$ are tracks are sampled from the standard halo model velocity distribution [100]. These tracks are assumed to be isotropically distributed, and are parameterised based on where the tracks enter and exit a spherical surface as described in subsection 4.1.1. The assumption of an isotropic distribution is an approximation that does not take into account the modulation of the dark matter velocity distribution and flux due to the relative motion of the lab frame and the galactic frame.

3. For a given track, the vector describing the closest approach to every sensor is computed. The length of this vector is the impact parameter of the track, given a sensor. The

signal strength for each sensor can then be computed analytically. This is described in detail in subsection 4.2.1.

4. The signal strength is divided by the noise, as calculated based on sensor parameters, and summed in quadrature.

5. Steps 3-4 are repeated for each track. Based on this and a chosen SNR threshold, the detection probability of a track is computed.

6. Using the detection probability and the dark matter flux based on the standard halo model, the sensitivity of the array can be computed.

In this work, the generated sensor arrays are all cubic. However, this fast sensitivity projection method can also be used to evaluate sensor geometry optimisation, and this is something we are interested in exploring in the future.

### 4.2.1 Analytic Calculation of Signal-to-noise Ratio for a Single Sensor
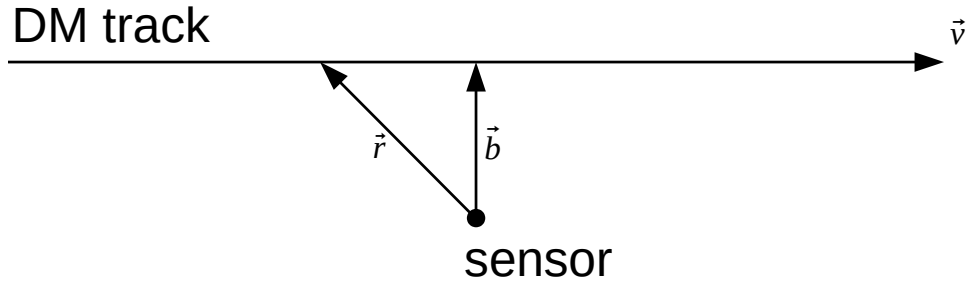


**Figure 4.1.** Schematic of a dark matter particle passing by a sensor, with the vector convention to be used in the rest of the note. $\vec{b}$ refers to the vector that denotes the minimum distance between the sensor and the track, the length of which is the impact parameter. $\vec{v}$ refers to the velocity vector of the dark matter particle.

The vector notation to be used in the rest of this section is shown in Fig. 4.1. While the impact parameter is typically not the same as distance of closest approach, in our case, we

expect tracks to be linear due to how weak interactions are expected to be and how heavy the particles we are considering are $\sim M_{\text{Planck}} \approx 20\,\mu\text{g}$. Each sensor is considered to be sensitive to forces in only one direction, denoted by the unit vector $\hat{n}$, as opposed to being 3-axis accelerometers. The detected acceleration as a function of time is then given by:

$$a(t) = \frac{Gm_\chi}{(b^2 + v^2 t^2)^{3/2}} \left( b\hat{b} + vt\hat{v} \right) \cdot \hat{n} \tag{4.1}$$

where $m_\chi$ is the mass of the dark matter particle, $G$ is the gravitational constant, and $\hat{b}$ and $\hat{v}$ are unit vectors in the directions of $\vec{b}$ and $\vec{v}$, respectively. If template matching is used, and we assume that the signal template is modelled perfectly, then the template is simply given by the same function as the signal, $a(t)$. In such a situation, the matched signal is given by

$$S = \int_{-\infty}^{\infty} a(t)^2 dt, \tag{4.2}$$

because the product of the template $f(t) = a(t)$ and the signal $a(t)$ is $a(t)^2$.

This assumes the template is normalised to have the same units as the signal. However, as the same template will be used to derive the noise, the normalisation of the template does not affect the SNR. The noise from template matching is given by:

$$N^2 = \text{Var}\left[ \int_{-\infty}^{\infty} a(t)w(t)dt \right] \tag{4.3}$$

where $w(t)$ refers to the noise time series. The mean of noise can be measured and subtracted in data analysis, thus the variance is the relevant parameter.

The complete expression for the integrated signal can be found by substituting the expression for $a(t)$, given in Equation 4.1, into Equation 4.2. The result is:

$$
\begin{aligned}
S &= G^2 m_\chi^2 \int_{-\infty}^{\infty} \frac{b^2 \left(\hat{b} \cdot \hat{n}\right)^2 + v^2 t^2 \left(\hat{v} \cdot \hat{n}\right)^2 + 2bvt \left(\hat{b} \cdot \hat{n}\right)\left(\hat{v} \cdot \hat{n}\right)}{\left(b^2 + v^2 t^2\right)^3} dt \\
&= G^2 m_\chi^2 \left( \frac{3\pi \left(\hat{b} \cdot \hat{n}\right)^2}{8 b^3 v} + \frac{\pi \left(\hat{v} \cdot \hat{n}\right)^2}{8 b^3 v} + 0 \right) \\
&= \frac{G^2 m_\chi^2 \pi \left(3 \left(\hat{b} \cdot \hat{n}\right)^2 + \left(\hat{v} \cdot \hat{n}\right)^2\right)}{8 b^3 v}.
\end{aligned}
\tag{4.4}
$$

As the noise term is stochastic, the treatment is more complex. For simplicity, we model the noise as a stationary Gaussian process or white noise. Let the sampling timestep be $\Delta t$, and the noise be Gaussian at each sample where the noise integrated over one timestep $\Delta t$ has standard deviation $\sigma_{\text{noise}}$. Note that with this definition, $\sigma_{\text{noise}}$ has units of acceleration $\times$ time. We now denote the integral of the noise time series $w(t)$ over time $\tau$ as $W_\tau$:

$$
W_\tau = \int_0^\tau w(t) dt.
\tag{4.5}
$$

As defined above, $W_{\Delta t} \sim \mathcal{N}(0, \sigma_{\text{noise}}^2)$. Due to stationarity, $W_{2\Delta t} = W_{\Delta t} + W'_{\Delta t} \sim \mathcal{N}(0, 2\sigma_{\text{noise}}^2)$. As such, $W_\tau \sim \mathcal{N}\left(0, \frac{\tau}{\Delta t} \sigma_{\text{noise}}^2\right)$. It can be seen that this is a Wiener process [118]. The noise variance from template matching, as defined in Equation 4.3, can thus be derived as such:

$$
\begin{aligned}
N^2 &= \text{Var}\left[\int_{-\infty}^{\infty} a(t) w(t) dt\right] \\
&= \text{Var}\left[\lim_{\delta t \to 0} \sum_{i=-\infty}^{\infty} a(i\delta t) W_{\delta t}\right] \\
&= \lim_{\delta t \to 0} \sum_{i=-\infty}^{\infty} a(i\delta t)^2 \frac{\delta t}{\Delta t} \sigma_{\text{noise}}^2 \\
&= \int_{-\infty}^{\infty} a(t)^2 \frac{\sigma_{\text{noise}}^2}{\Delta t} dt \\
&= \frac{\sigma_{\text{noise}}^2}{\Delta t} S.
\end{aligned}
\tag{4.6}
$$

We can also express this in terms of the power spectral density (PSD) of noise, in units of $\frac{[\text{accel}]^2}{[\text{frequency}]}$. The Wiener-Kinchin theorem states that the spectral density $S_{aa}(\omega) = \langle \hat{a}_{\text{noise}}(\omega) \hat{a}_{\text{noise}}(\omega) \rangle$, can be given by taking the Fourier transform of the autocorrelation function $r_{aa}(\tau) = \langle a_{\text{noise}}(t) a_{\text{noise}}(t - \tau) \rangle$ [119]. The auto-correlation of white noise is simply a delta function because the Dirac delta function forms a Fourier transform pair with the constant 1 [119]; as such, for a discrete measurement, $S_{aa} = r_{aa}[0]$. The value of the autocorrelation function at the origin is given by the noise variance, $r_{aa}[0] = \sigma'^2_{\text{noise}}$, where $\sigma'_{\text{noise}} = \frac{\sigma_{\text{noise}}}{\Delta t}$ is the standard deviation of measured samples in units of acceleration. Thus, in the units of the discrete Fourier transform, $S_{aa} = \sigma'^2_{\text{noise}}$. As DFT units are per $\frac{1}{\Delta t}$, in real units we get $S_{aa} = \Delta t \sigma'^2_{\text{noise}} = \frac{\sigma^2_{\text{noise}}}{\Delta t}$.

$$\begin{aligned} \frac{S}{N} &= \frac{\sqrt{S \Delta t}}{\sigma_{\text{noise}}} \\ &= \sqrt{\frac{S}{S_{aa}}} \end{aligned} \tag{4.7}$$

When used together, Equation 4.4 and Equation 4.7 can be used to directly compute the signal-to-noise ratio for a given dark matter track and sensor. This can be extended to a sensor array by summing the signal-to-noise ratios of each sensor in quadrature. The above derivation does not account for tracks that intersect the test mass of a sensor. In the absence of a detailed derivation of the signal from a dark matter track that intersects a sensor, we conservatively consider a smaller sensor test mass where the density remains the same, but the radius is reduced such that it no longer intersects the dark matter track. This reduces the force on the sensor and decreases the SNR; equivalently, in units of acceleration, the signal is unchanged but the noise increases.

### 4.2.2 Noise models

There are 3 primary sources of noise that we model in this section: thermal noise, quantum noise, and superconducting quantum interference device (SQUID) measurement noise. Thermal noise and quantum noise refer to noise due to thermal fluctuations and the Heisenberg uncertainty principle respectively. SQUID measurement noise, on the other hand,

is motivated by the concept of magnetically-levitated superconducting sensors, where the position of a test mass is measured using a SQUID, such as [120].

**Thermal Noise**

In [23], Daniel Carney et al. note that the uncertainty from thermal noise for impulse sensing is given by

$$\Delta I^2_{\text{thermal}} = \alpha_{\text{thermal}} t_{\text{int}} \tag{4.8}$$

for a constant $\alpha_{\text{thermal}}$, which depends on the way thermal noise couples with the sensor. $t_{\text{int}}$ refers to the integration or measurement time. This $\alpha_{\text{thermal}}$ is related with the $\sigma_{\text{noise}}$ defined in subsection 4.2.1 as such:

$$\alpha_{\text{thermal}} = m_s^2 \frac{\sigma^2_{\text{noise}}}{\Delta t} \tag{4.9}$$

where $m_s$ is the test mass of the sensor. Defining the parameter $\beta = \alpha_{\text{thermal}}/m_s^2 = \sigma^2_{\text{noise}}/\Delta t$, the SNR of a single sensor is simply given by

$$\frac{S}{N} = \sqrt{\frac{S}{\beta}}. \tag{4.10}$$

The parameter $\beta$ can thus be recognised as the spectral density of thermal noise. For a sensor that is mechanically coupled to the environment, the thermal noise is given by

$$\beta_{\text{mech}} = \frac{4k_B T \gamma}{m_s} \tag{4.11}$$

where $k_B$ is Boltzmann's constant, $T$ is the temperature, and $\gamma = \omega_m/Q_m$ is the mechanical damping rate given by the mechanical resonance frequency divided by the quality factor. For a sensor that is free-falling and is hence not mechanically coupled to the environment, the thermal noise is instead given by

$$\beta_{\text{gas}} = \frac{P A_d \sqrt{m_a k_B T}}{m_s^2}. \tag{4.12}$$

Here, $P$ is the pressure of the ambient gas, $A_d$ is the cross-sectional area of the sensor, and $m_a$ is the mass of the gas atoms or molecules.

**Quantum Noise**

As quantum noise is not necessarily white noise, instead of using the template matching formalism derived in subsection 4.2.1, we simply consider the signal as a sharp impulse fully contained within a measurement period $\tau$, and consider the amount of integrated impulse from noise sources over the measurement period. Without any quantum noise reduction techniques such as back-action evasion (for example, see [121]), for a free particle, the uncertainty of a position measurement is given by

$$\delta x^2 \leq \frac{\hbar \tau}{m_s}, \tag{4.13}$$

where $\tau$ is the measurement time [122]. We term the sensitivity limit due to this quantum noise the standard quantum limit (SQL). If one considers a force or impulse measurement made by subtracting subsequent position measurements, the force uncertainty would be given by

$$F_{SQL}^2 = \frac{4m_s\hbar}{\tau^3}, \tag{4.14}$$

and as impulse is $I = F\tau$, the impulse uncertainty would be given by

$$I_{SQL}^2 = \frac{4m_s\hbar}{\tau}. \tag{4.15}$$

For a sensor where the test mass is bound as opposed to free-falling, the $I_{SQL}$ derived above is only approximate. This remains a good approximation, however, as long as $1/\tau \gg \omega_m$; when this condition is not satisfied, the ground state momentum fluctuations of the oscillator ($\sim \hbar m \omega_m$) [23, 123] are no longer negligible.

While thermal and quantum noise are technically independent, they have different dependence on the measurement time, $\tau$. We can consider the total noise in our system, and optimise $\tau$ to give the lowest possible impulse uncertainty. In addition, for studies of the sensitivity of sensor arrays where quantum noise reduction techniques such as back-action evasion are applied, quantum noise reduction can be introduced by simply scaling the quantum

noise by a parameter $\xi$. This is a naive treatment, as it does not account for changes in the noise spectrum that are introduced by many such techniques. We use this parameterisation primarily to benchmark the amount of quantum noise reduction required for the science targets of future Windchime experiments, in the absence of a detailed experimental design that can be used to derive more physically-motivated noise models. The impulse uncertainty of a sensor is thus:

$$\Delta I^2_{\text{quantum}} = \frac{4m\hbar}{\tau\xi^2} + \alpha_{\text{thermal}}\tau. \tag{4.16}$$

The $\alpha_{\text{thermal}}$ term is defined equivalently to Equation 4.8.

The optimal measurement time, $\tau$, can then be computed by finding the minima of Equation 4.16. This yields $\tau_{\text{optimal}}$:

$$\tau_{\text{optimal}} = \frac{2}{\xi}\sqrt{\frac{\hbar m_s}{\alpha_{\text{thermal}}}} \tag{4.17}$$

The optimal impulse sensitivity can then be found by substituting Equation 4.17 into Equation 4.16, giving

$$\Delta I^2_{\text{optimal}} = \frac{4}{\xi}\sqrt{\hbar m_s \alpha_{\text{thermal}}}. \tag{4.18}$$

As Equation 4.18 is derived under the approximation that the signal is fully contained within the measurement time $\tau$, Equation 4.17 and Equation 4.18 only apply when $\tau$ is smaller than the characteristic time of our signal. To remedy this, we can use a piecewise function that uses $\tau_{\text{optimal}}$ only when it is smaller than $2b/v$, where $v$ is the velocity of a given dark matter track and $b$ is the impact parameter. Integrating Equation 4.1 from $t = -b/v$ to $t = b/v$ shows that this characteristic time captures $1/\sqrt{2}$ of the signal. We thus obtain the following expression for the combined quantum and thermal noise:

$$\Delta I^2 = \begin{cases} \frac{4}{\xi}\sqrt{\hbar m_s \alpha_{\text{thermal}}} & \tau_{\text{optimal}} > \frac{2b}{v} \\ \frac{2m_s \hbar v}{b\xi^2} + \alpha_{\text{thermal}}\frac{2b}{v} & \tau_{\text{optimal}} \leq \frac{2b}{v} \end{cases} \tag{4.19}$$

We can compare the Equation 4.19 with a detailed frequency-domain optomechanical noise model, using the noise model from [23] based on an interferometric readout with a pair of optical cavities, with the force noise PSD:

$$N(\omega) = \frac{1}{|G|^2 |\chi_c|^2 |\chi_m|^2} + N_{BM} + \hbar^2 |G|^2 |\chi_c|^2 \tag{4.20}$$

In Equation 4.20, the first term is due to shot noise, the second term is due to thermal noise, and the last term is due to quantum back-action. The optomechanical coupling strength is given by

$$G = \sqrt{\frac{2 P_{in} \omega_c}{\hbar \kappa l_c^2}}, \tag{4.21}$$

where $P_{in}$ is the laser power, $\omega_c$ is the optical cavity resonance frequency, $\kappa = \omega_c/Q_c$ is the optical cavity energy loss rate given by the cavity resonance frequency divided by its quality factor, and $l_c$ is the cavity length. The cavity susceptibility is given by

$$|\chi_c(\omega)|^2 = \frac{\kappa}{\omega^2 + \kappa^2/4}, \tag{4.22}$$

and the mechanical susceptibility is given by

$$|\chi_m(\omega)|^2 = \frac{1}{m_s^2 \left((\omega^2 - \omega_m^2)^2 + \gamma^2 \omega^2\right)} \tag{4.23}$$

where $\omega_m$ is the mechanical resonance frequency of the sensor being read out, and $\gamma = \omega_m/Q_m$ is the mechanical damping rate. We can also introduce quantum noise reduction by simply scaling the shot noise and quantum backaction terms by $\xi^2$.

The thermal noise term is as defined by Equation 4.8, with $N_{BM} = \alpha$. We can now compare the SNR of an impulse computed with Equation 4.19, with a numerically integrated SNR with the frequency-domain noise model as given by Equation 4.20. The SNR using the approximate model, Equation 4.19, is simply given by $\mathrm{SNR}_{approx} = \Delta p/\Delta I$, with $\Delta p = \frac{2 G m_{planck} m_s}{bv} \left(\hat{b} \cdot \hat{n}\right)$ being the total transferred momentum in the direction of sensor sensitivity indicated by unit

vector $\hat{n}$. The SNR from the frequency-domain noise model, on the other hand, is obtained by computing the integral

$$\int_0^\infty \frac{|\hat{F}(\omega)|^2}{N(\omega)} d\omega \tag{4.24}$$

where $\hat{F}(\omega)$ is the Fourier transform of the measured force, $F(t)$. This is the Fourier transform of the acceleration signal, Equation 4.1, multiplied by the sensor mass $m_s$:

$$|\hat{F}(\omega)|^2 = (Gm_\chi m_s)^2 \frac{2\omega^2}{\pi v^4} \left[ K_1 \left(\frac{b}{v}\omega\right)^2 \left(\hat{b} \cdot \hat{n}\right)^2 + K_0 \left(\frac{b}{v}\omega\right)^2 \left(\hat{v} \cdot \hat{n}\right)^2 \right] \tag{4.25}$$

where $K_n$ is the modified Bessel functions of the second kind of order $n$ [83]. For the comparison between the simplified model and the frequency model, we can consider tracks that are perpendicular to the $\vec{b}$ vector, such that $\hat{b} \cdot \hat{n} = 1$. The parameters used for the comparison can be found in Table 4.1.

**Table 4.1.** Parameters used for the comparison between the frequency-domain noise model and the simplified noise model. Only mechanical quality factor $Q_m$, sensor mass $m_s$, sensor density, pressure $P$, dark matter velocity $v$, dark matter mass $m_\chi$, and impact parameter $b$ are used in the simplified model. The cross-sectional area of the sensor test mass, $A_d$, is computed using the sensor mass $m_s$ and density, assuming a spherical test mass. The density is based on silicon nitride [124].

| Parameter | Value |
|---|---|
| Mechanical quality factor $Q_m$ | $10^8$ |
| Mechanical resonance frequency $\omega_m$ | $10^{-4}$ Hz |
| Optical quality factor $Q_c$ | $10^8$ |
| Optical resonance frequency $\omega_c$ | $2\pi 1.94 \times 10^{14}$ Hz |
| Cavity length $l_c$ | $1.5$ cm |
| Sensor mass $m_s$ | $1$ g |
| Sensor density | $3.17 \times 10^3$ kg/m$^3$ |
| Pressure $P$ | $10^{-10}$ Pa |
| Dark matter velocity $v$ | $220$ km/s |
| Dark matter mass $m_\chi$ | $M_{\text{Planck}}$ |
| Impact parameter $b$ | $5$ mm |
| Temperature $T$ | $10$ mK |

A plot of frequency-domain optomechanical noise model and the frequency-domain signal are shown in Figure 4.2. It should be noted that because the x-axis is logarithmic, while the

spectral density of the signal is flat, almost all of the signal is concentrated in the highest few orders of magnitudes of frequency before the cut-off near $10^8$ Hz. For a flat spectral density as shown, for example, it is evident that the $10^6$ Hz $\sim 10^7$ Hz range contributes $10\times$ more than in the $10^5$ Hz $\sim 10^6$ Hz range when the signal is integrated in frequency. It can also be seen that while Equation 4.24 can be computed numerically as-is, this is challenging, as there are spectral features that span many orders of magnitude. Thus, a substitution can be made so that the integral can be computed in log-space. We let $e^u = \omega$, giving us $e^u du = d\omega$, and numerically compute the following integral instead:

$$\int_{-\infty}^{\infty} \frac{|\hat{F}(e^u)|^2}{N(e^u)} e^u du. \tag{4.26}$$

As the SNR depends on the laser power, for every value of $\xi$, the laser power is optimised. This is done simply by computing the SNR as a function of laser power and finding the maxima, as shown in Figure 4.3. The comparison between the simplified and frequency-domain noise models is shown below in Figure 4.4. It can be seen that the two models agree well; as such, the simplified model can be used to estimate the performance of a large array of sensors with optomechanical readout. In addition, it should be noted that Figure 4.4 shows that this approximate model is not conservative, and predicts a slightly better sensitivity than obtained from numerical integration.

**Classical Position-sensing Noise**

Calculations in this subsection are based on personal communication and internal Windchime notes by Gerard Higgins. For sensors where impulses are inferred from position measurement, if the position-sensing noise is modelled to be frequency-independent, the position sensing uncertainty is given by

$$\Delta x^2 = \frac{S_{xx}}{\tau} \tag{4.27}$$

where $S_{xx}$ is the position-sensing PSD.
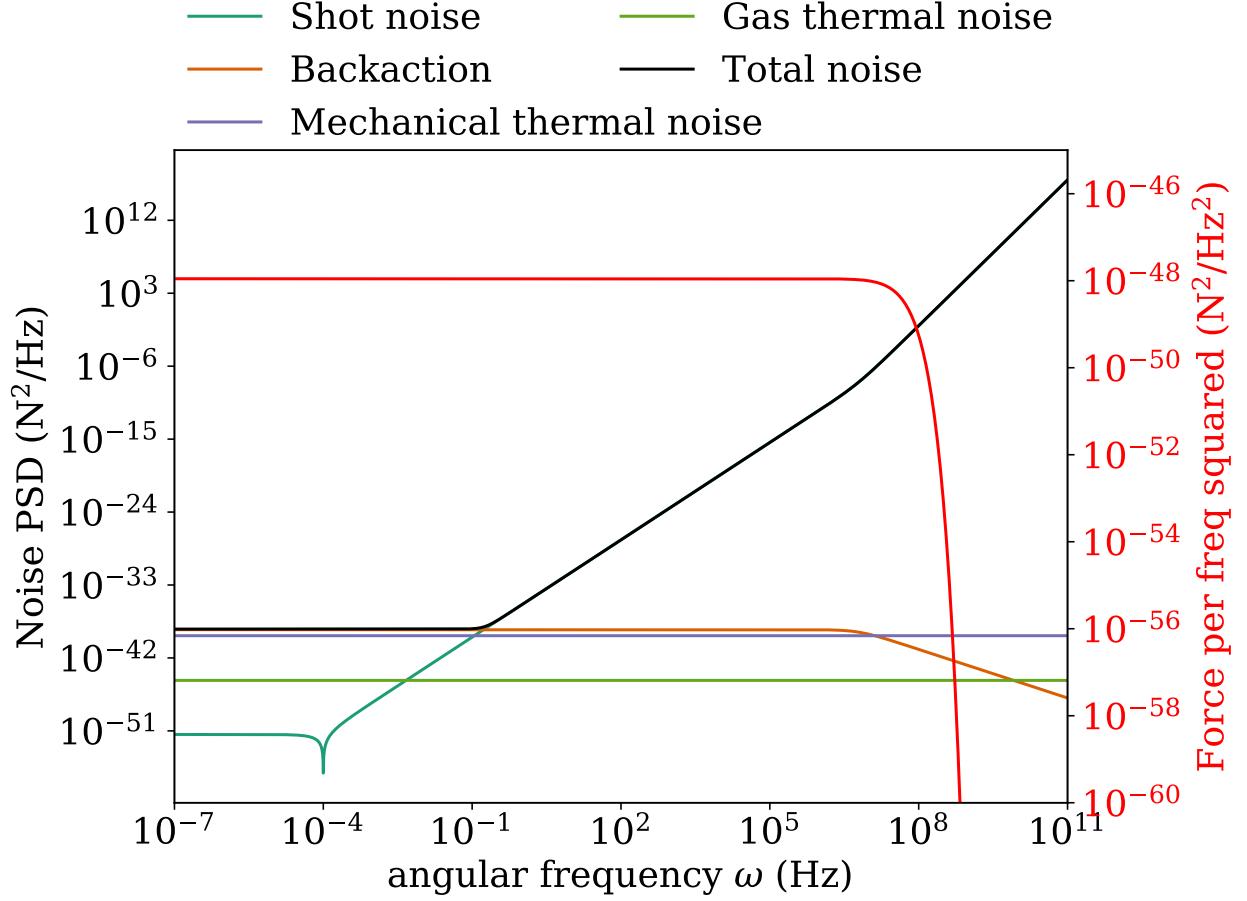
**Figure 4.2.** Noise power spectra as a function of angular frequency with thermal noise and the signal model from a Planck mass particle passing by our sensor. The parameters used are given by Table 4.1, and the optical power used is $10^{-10}$ W. The dimensions for noise PSD and signal spectral density are different, thus the scale for noise PSD y-axis is on the left, whereas the scale for the signal spectral density is on the right in red.
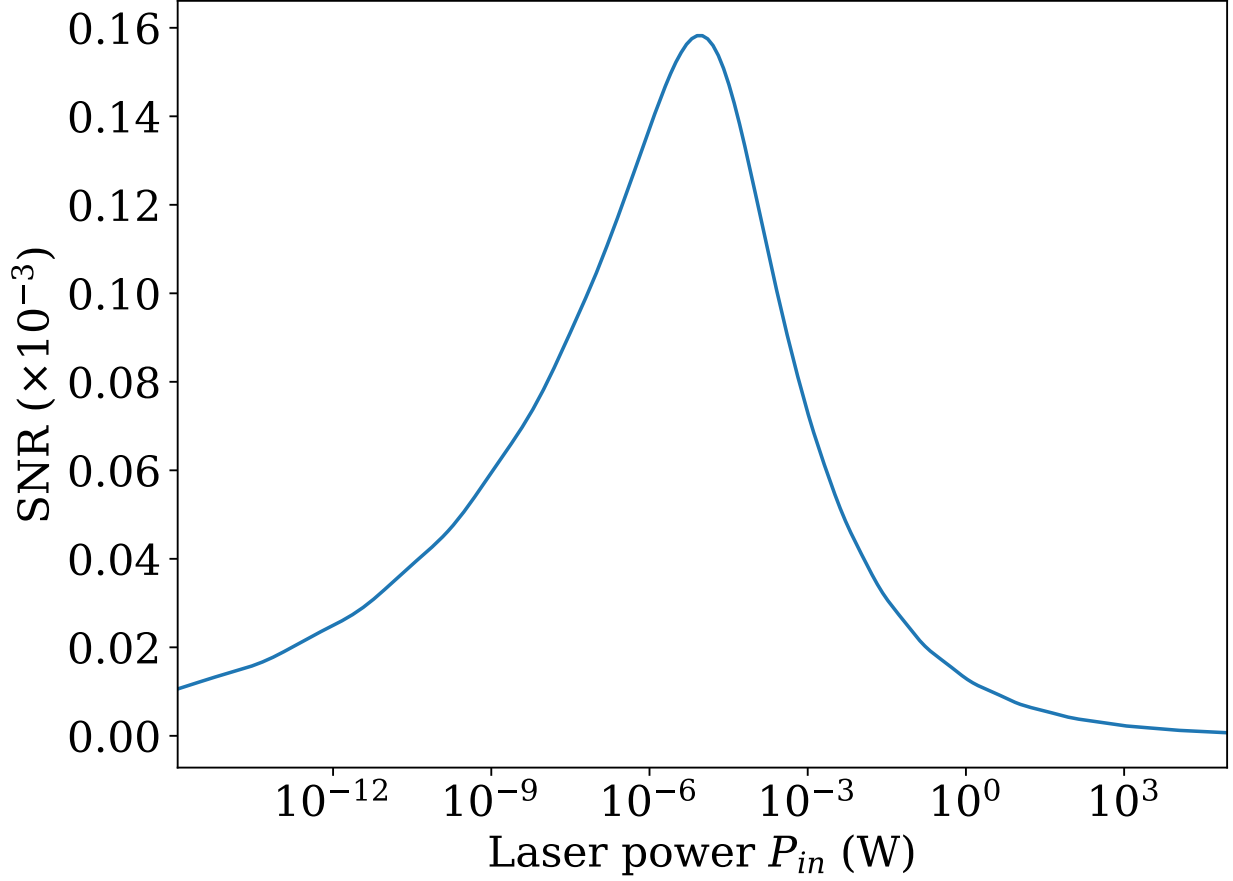
**Figure 4.3.** SNR of a dark matter track passing by a single sensor. The parameters of the noise and signal models are given by Table 4.1, and 30 dB of quantum noise reduction is used to generate this plot.

If $\tau$ is much greater than the mechanical period of the sensor, the position and momentum amplitudes are related as such due to conservation of energy:

$$\frac{1}{2}m_s\omega_m^2 x_{max}^2 = \frac{p_{max}^2}{2m_s} \tag{4.28}$$
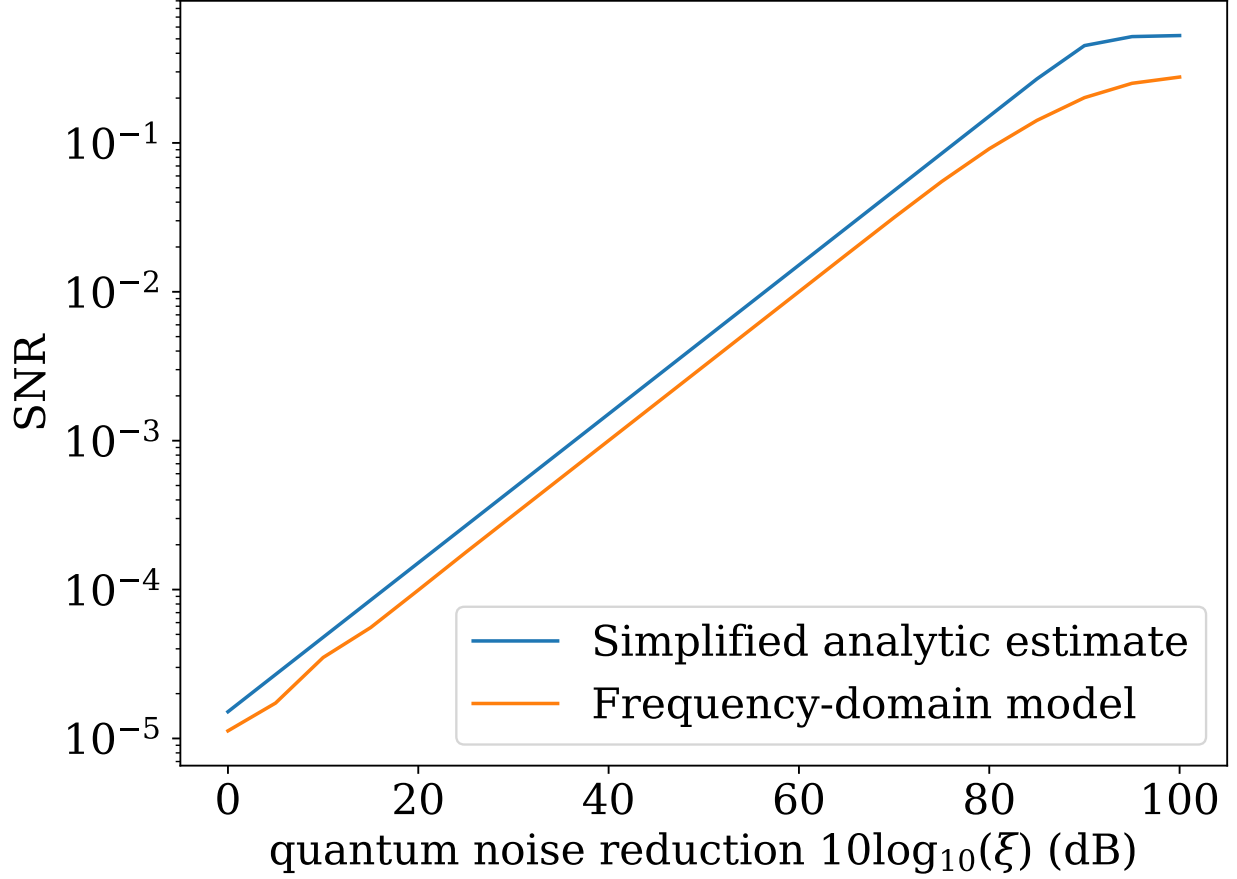
**Figure 4.4.** Comparison of SNR predicted with the simplified model, and the frequency-domain model with numerical integration. It can be seen that the two models agree with only a small discrepancy.

As the PSD is proportional to the square of the amplitude, the momentum-sensing PSD can be expressed in terms of position-sensing PSD as such:

$$S_{pp} = m_s^2 \omega_m^2 S_{xx}, \tag{4.29}$$

and thus the uncertainty of an impulse measurement is

$$\Delta I_{\text{classical}}^2 = \frac{S_{pp}}{\tau} = m_s^2 \omega_m^2 \frac{S_{xx}}{\tau}. \tag{4.30}$$

The optimal $\tau$, given both thermal and classical measurement noise, can be derived using the same approach earlier used for quantum noise, giving

$$\tau_{\text{optimal}} = \sqrt{\frac{m_s^2 \omega_m^2 S_{xx}}{\alpha_{\text{thermal}}}} \tag{4.31}$$

and

$$\Delta I^2 = \begin{cases} 2m_s\omega_m\sqrt{S_{xx}\alpha_{\text{thermal}}} & \tau_{\text{optimal}} > \frac{20\pi}{\omega_m} \\ m_s^2\omega_m^3\frac{S_{xx}}{2\pi} + \alpha_{\text{thermal}}\frac{2\pi}{\omega_m} & \tau_{\text{optimal}} \leq \frac{20\pi}{\omega_m} \end{cases} \tag{4.32}$$

The minimum allowed value for $\tau$ is $\frac{20\pi}{\omega_m}$ because the above derivation assumes $\tau \gg \frac{2\pi}{\omega_m}$.

### 4.2.3 Sensitivity of a Sensor Array

Given the above signal and noise models, we can make projections of the sensitivity of various configurations of sensor arrays. Instead of Newtonian gravity, we consider is an arbitrary long-range attractive interaction, as the gravitational interaction is extremely weak and is the eventual goal of Windchime, not the near-term goal. Considering an arbitrary long-range force allows for the sensitivity to be re-cast into the relevant parameter space for specific dark matter models that involve long-range attractive forces with ranges longer than the metre-scale, corresponding to mediator masses below $100\,\text{neV}/\text{c}^2$ [26]. In addition, to make the coupling as generic as possible, we consider a coupling to atomic nuclei or neutral atoms, as opposed to mass, as the relevant charge for some models might be material-dependent, such as $B - L$ charge [26, 125]. Limits are thus made based on the following parameterisation of the long-range force:

$$F = \frac{\alpha\hbar c N_{\text{nuclei}}}{r^2} \tag{4.33}$$

where $\alpha$ is the dimensionless coupling constant we use to parameterise the sensitivity of a sensor array. This parameterisation is only valid for interactions with ranges that are much greater than the spacing between sensors in our sensor array. The value of $\alpha$ corresponding to the gravitational interaction is then given by

$$\alpha_G = \frac{Gm_\chi m_{\text{nuclei}}}{\hbar c}. \tag{4.34}$$

It can be seen from the form of Equation 4.34 that the $\alpha$ defined here is analogous to the fine structure constant for the electromagnetic interaction; however, $m_{\mathrm{nuclei}}$ is used instead of the nucleon mass because the scaling between nucleon and nuclear cross sections can be model-dependent in this high cross section regime [126]. It should be noted that due to $m_{\mathrm{nuclei}}$ appearing in Equation 4.34, $\alpha_G$ is material dependent. In addition, it depends on $m_\chi$, and hence the gravitational coupling strength does not correspond to a constant mass-independent coupling strength. The sensitivity is determined based on the procedure listed at the beginning of this section. The probability of getting a detection over an SNR threshold of 10 is computed for every combination of $\alpha$ and $m_\chi$, and the sensitivity curves are defined by the regions of parameter space that are more than 90% likely to produce at least one dark matter track with a positive detection. We can demonstrate the sensitivity-estimate procedure detailed in this work by estimating the sensitivity of three sensor arrays, with parameters as shown in Table 4.2. These configurations represent guesses for the performance and scale of different generations of the Windchime experiment, and are meant to demonstrate this sensitivity estimation procedure; they should not be viewed as a roadmap for Windchime. The SNR threshold is chosen based on estimates of the look-elsewhere effect from section 4.4 and chapter 5.

A plot of the sensitivity curves is shown in Figure 4.5. The XENON1T limit is based on the limit from [127]. The conversion to the parameterisation given by Equation 4.33 is derived by Zhen Liu and computed by Shengchao Li, who are part of the Windchime collaboration. This is done by first considering the cross section for Coulomb scattering for an electron and a millicharged particle. In natural units, this is [128]:

$$\frac{d\sigma}{dE_r} = \pi\alpha^2\epsilon^2 \frac{2E_\chi^2 m_e + E_r^2 m_e - E_r\left(m_\chi^2 + m_e(2E_\chi + m_e)\right)}{E_r^2(E_\chi^2 - m_\chi^2)m_e^2}, \qquad (4.35)$$

where the charge is given by $\epsilon$. Note that this differential cross section diverges when integrated, as expected for a long-range force; in experiments, this divergence is not an issue due to a

**Table 4.2.** Parameters for different sensor array configurations. These configurations should not be viewed as a roadmap for Windchime, and represent plausible configurations used to demonstrate the limit-setting procedure. The noise PSD for configuration 1 is based on estimates of the achievable noise for magnetically levitated particles read out via a SQUID from the supplemental materials of [120], though the paper notes that lower noise levels might be achievable still as the sensor mass considered here is considerably higher. The quantum noise reduction value for configuration 3 is based on the optomechanical sensing backaction evasion scheme described in [121], where it is noted that the scheme is likely limited to 30 dB given losses in currently-achievable fabrication techniques; configuration 2 was chosen to have 15 dB of quantum noise reduction as an intermediate step.

| Parameter | Configuration 1 | Configuration 2 | Configuration 3 |
|---|---|---|---|
| Mechanical quality factor $Q_m$ | $10^9$ | $3 \times 10^9$ | $3 \times 10^9$ |
| Resonance frequency $\omega_m$ | 100 Hz | 100 Hz | 10 Hz |
| Sensor mass $m_s$ | 1 g | 1 g | 1 g |
| Sensor density | $1.13 \times 10^4\,\mathrm{kg/m^3}$ | $1.13 \times 10^4\,\mathrm{kg/m^3}$ | $1.13 \times 10^4\,\mathrm{kg/m^3}$ |
| Pressure $P$ | $10^{-14}$ Pa | $10^{-14}$ Pa | $10^{-14}$ Pa |
| Temperature $T$ | 15 mK | 15 mK | 15 mK |
| Noise model | Classical | Quantum | Quantum |
| Quantum noise reduction $\xi$ | - | 15 dB | 30 dB |
| Classical noise PSD $S_{xx}$ | $10^{-15}\,\mathrm{m}/\sqrt{\mathrm{Hz}}$ | - | - |
| Sensor count | $3 \times 1 \times 1$ | $3 \times 1 \times 1$ | $10 \times 10 \times 10$ |
| Sensor array size | 0.6 m | 0.6 m | 1.2 m |

threshold on the recoil energy $E_r$. As dark matter is non-relativistic, $E_\chi \approx m_\chi + \frac{1}{2}m_\chi v_\chi^2$. For a long range force that couples to the $B - L$ charge, we instead have

$$\frac{d\sigma}{dE_r} = \pi\alpha_{B-L}^2(A-Z)^2\frac{2E_\chi^2 m_n + E_r^2 m_n - E_r\left(m_\chi^2 + m_n(2E_\chi + m_n)\right)}{E_r^2(E_\chi^2 - m_\chi^2)m_n^2}, \qquad (4.36)$$

where $m_n$ is the neutron mass, $A$ is the mass number, $Z$ is the atomic number, and $\alpha_{B-L} = \frac{g_{B-L}g_{B-L}Q_\chi}{4\pi}$. This differential cross section is then integrated from a recoil energy of $10\,\mathrm{keV}$ (the XENON1T NR threshold [29]) to the maximum energy allowed by energy conservation (see [128]), to find $\sigma_{B-L}(\alpha_{B-L})$. In deriving the absolute cross section, we also multiplied the differential cross section with the XENON1T efficiency as a function of recoil energy. We then define $\sigma'_{B-L}(\alpha_{B-L}) = \sigma_{B-L}(\alpha_{B-L})/A^2$ to make the defined cross section comparable to the XENON1T limit which reports per-nucleus cross sections with $A^2$ scaling. This can be used to compute the value of $\alpha_{B-L}$ corresponding to the XENON1T limits. Finally, the corresponding conversion between $\alpha_{B-L}$ and $\alpha$ as defined in Equation 4.33 is $\alpha = 4\pi(A-Z)\alpha_{B-L}$, assuming $Q_\chi = \frac{m_\chi}{m_n}$. Making charge proportional to mass as such renders the conversation factor independent of mass $m_\chi$. This assumes that dark matter is a composite particle.

It should also be noted that these limits do not extend indefinitely to higher interaction strengths and lower masses. These limits are bounded both by the assumptions in the limit setting procedure and by the requirement that dark matter that is detected by a terrestrial experiment must make it through the atmosphere, and the overburden for underground experiments, without losing too much momentum. The assumption that dark matter tracks are linear implies that dark matter interacting with sensor test masses must not lose too much momentum; a line indicating where this becomes relevant to the configuration 2 limit is shown in Figure 4.6. This line is computed by finding the value of $\alpha$ where more than 1% of the momentum of a dark matter particle of a given mass can be deposited into a test mass. The overburden of terrestrial experiments might impose further bounds on the projected limits, and will be the subject of future work.
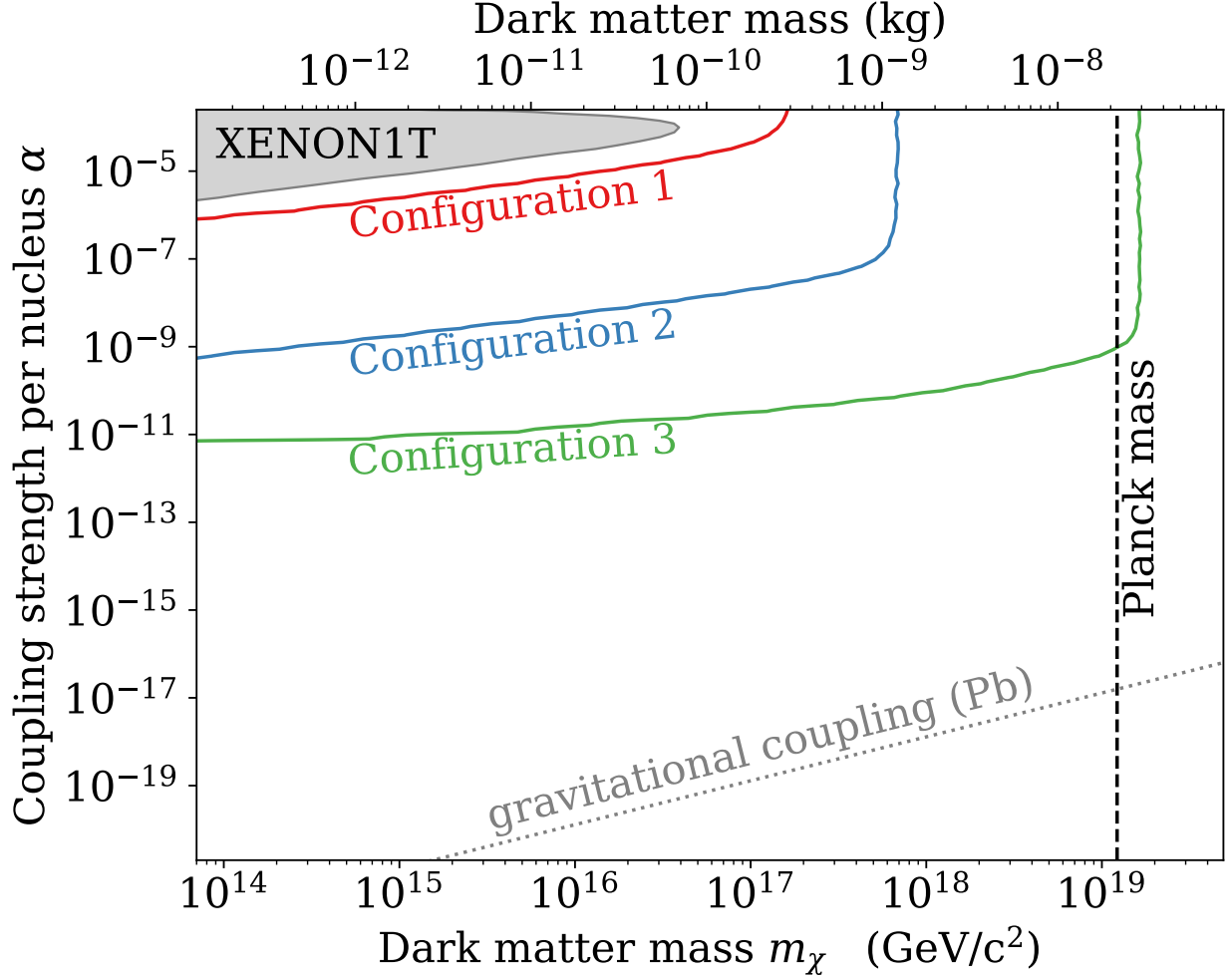
**Figure 4.5.** Dark matter sensitivity of 3 different sensor array configurations, as detailed in Table 4.2. The sensitivities computed here represent 90% confidence level exclusion limits in the signal-free scenario, where there is no dark matter close to the parameter spaces excluded by the exclusion limits. The Planck mass is indicated by the black dashed line, and the line corresponding to $\alpha_G$ for Pb, which is the material corresponding to the density used in Table 4.2, is indicated by the grey dotted line. The XENON1T limit is based on the limit from [127], with conversion to the parameterisation given by Equation 4.33 courtesy of Zhen Liu and Shengchao Li. This conversion assumes a long-range force coupling to the $B - L$ charge.
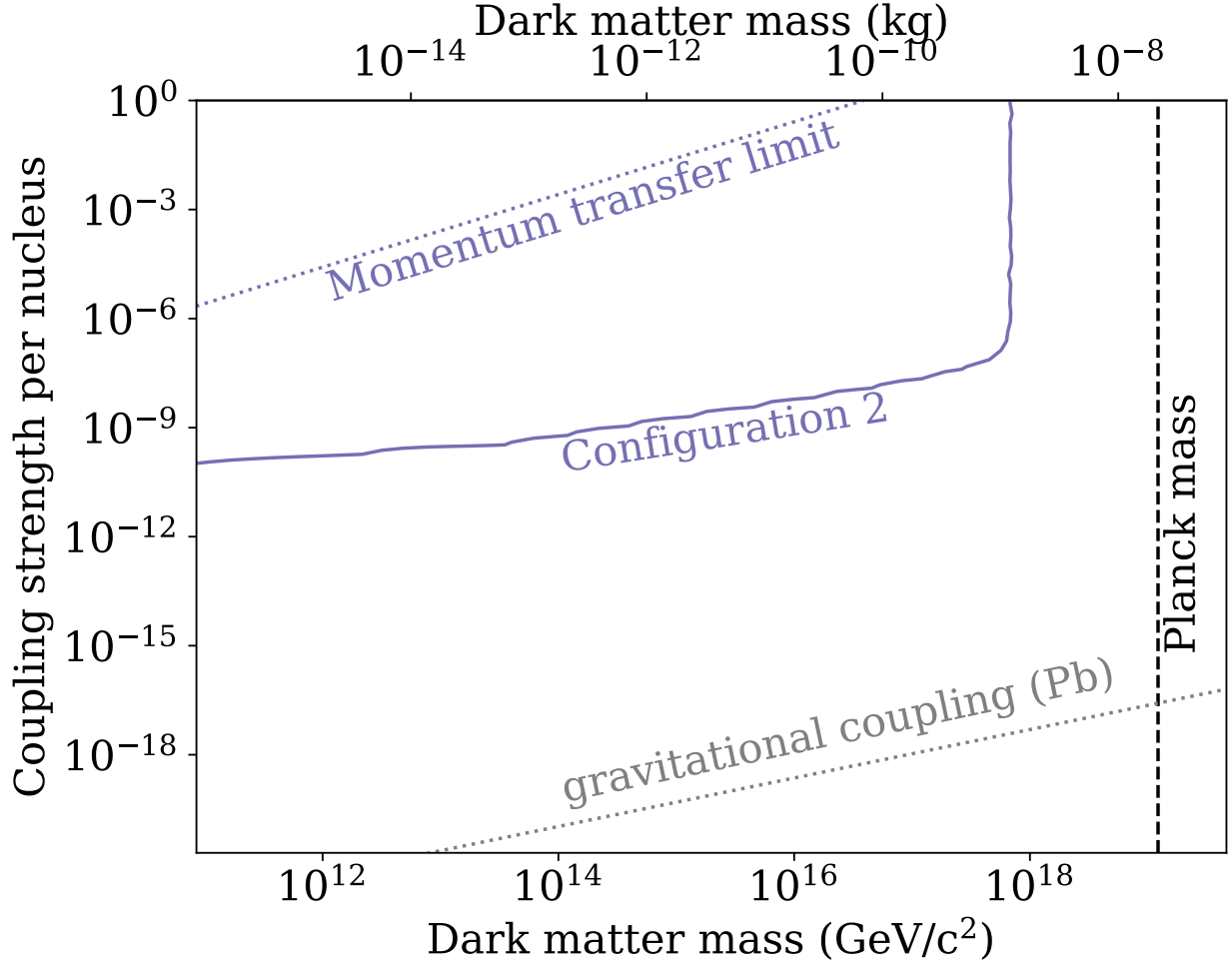
**Figure 4.6.** Dark matter sensitivity of configuration 2 as detailed in Table 4.2. The sensitivity here represents the 90% confidence level exclusion limit in the signal-free scenario, where there is no dark matter close to the parameter spaces excluded by the exclusion limits. The Planck mass is indicated by the black dashed line, and the line corresponding to $\alpha_G$ for Pb, which is the material corresponding to the density used in Table 4.2, is indicated by the grey dotted line. The dotted purple line indicates the line where the assumption that dark matter tracks are always linear is no longer accurate. Note that the axes on this plot differ from Figure 4.5, and that the dotted purple line is not visible without the bounds of that plot.

### 4.2.4 Further Work

In [23], it is noted that a sensor array that would be sensitive to the gravitational attraction of Planck-mass dark matter might require up to $\sim 10^9$ sensors. The methodology demonstrated above still takes approximately $\sim 1\,\text{hour}$ of CPU time for the $10^3$ sensor array in configuration 3. While the use of high-performance computing systems could allow for this limit to be scaled up by a few orders of magnitude, it is clear that this remains a challenge. To achieve this, in future work, I intend to pursue methods to project the sensitivity of a large array by splitting a large array into smaller sub-arrays, and only considering the signal from sub-arrays that the track would intersect. This relies on the fact that the relevant signal is highly concentrated towards sensors that are close to the track, owing to the rapid decay of the inverse-square law.

The above work also relies on the assumption of an isotropic distribution of dark matter tracks. This is an approximation that does not take into account the modulation of the dark matter velocity distribution and flux due to the relative motion of the lab frame and the galactic frame; further work will aim to address this shortcoming by implementing the relevant coordinate transforms to compute the diurnal and annual dark matter modulation [2, 43].

Finally, as noted previously, the overburden of dark matter with long range interactions has not yet been computed, and will be the subject of future work to make these limits more rigorous.

### 4.3 Frequentist Track-finding Using Template Matching

In this section, we demonstrate track-finding using template matching in a $4^3$ sensor array using simulated data. This sensor array with a dark matter track passing through is shown below in Figure 4.7.

The dark matter mass used is $2 \times 10^{-8}\,\text{kg} \approx m_{\text{planck}}$, and the noise PSD is $6 \times 10^{-21}\,\text{g}/\sqrt{\text{Hz}}$. The power spectral density is chosen to be able to demonstrate a positive detection and is not a projection of detector capabilities. The velocity of the chosen track is $280\,\text{km/s}$, close to the peak of the velocity distribution according to the standard halo model [43]. A sampling
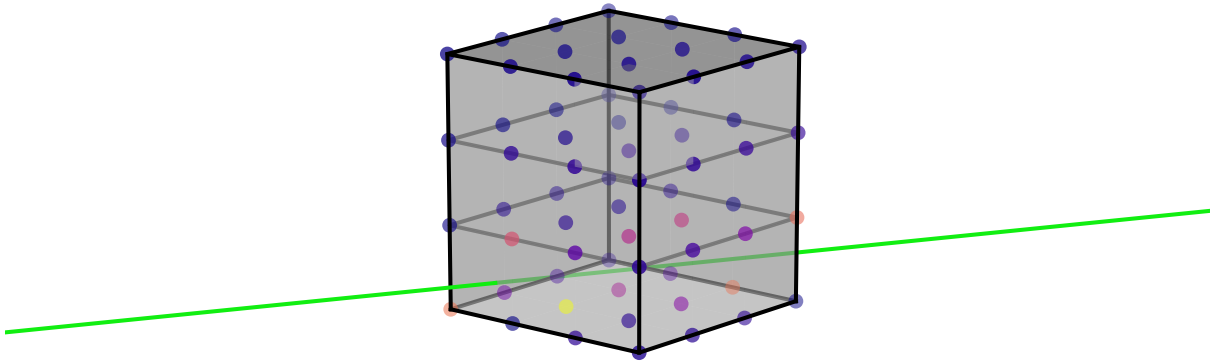
**Figure 4.7.** Plot of a $4 \times 4 \times 4$ sensor array, with sensors represented by coloured circles. The strength of an acceleration signal is indicated by the sensor colour. An example track going through the array is shown in green. The length of one side of the sensor array is $0.6\,\mathrm{m}$.

time of 100 ns is used. The simulated data for this track is shown in Figure 4.8, where we can see that the signal is not visible above the noise floor. This demonstrates the necessity of template matching to extend the reach of our sensors.
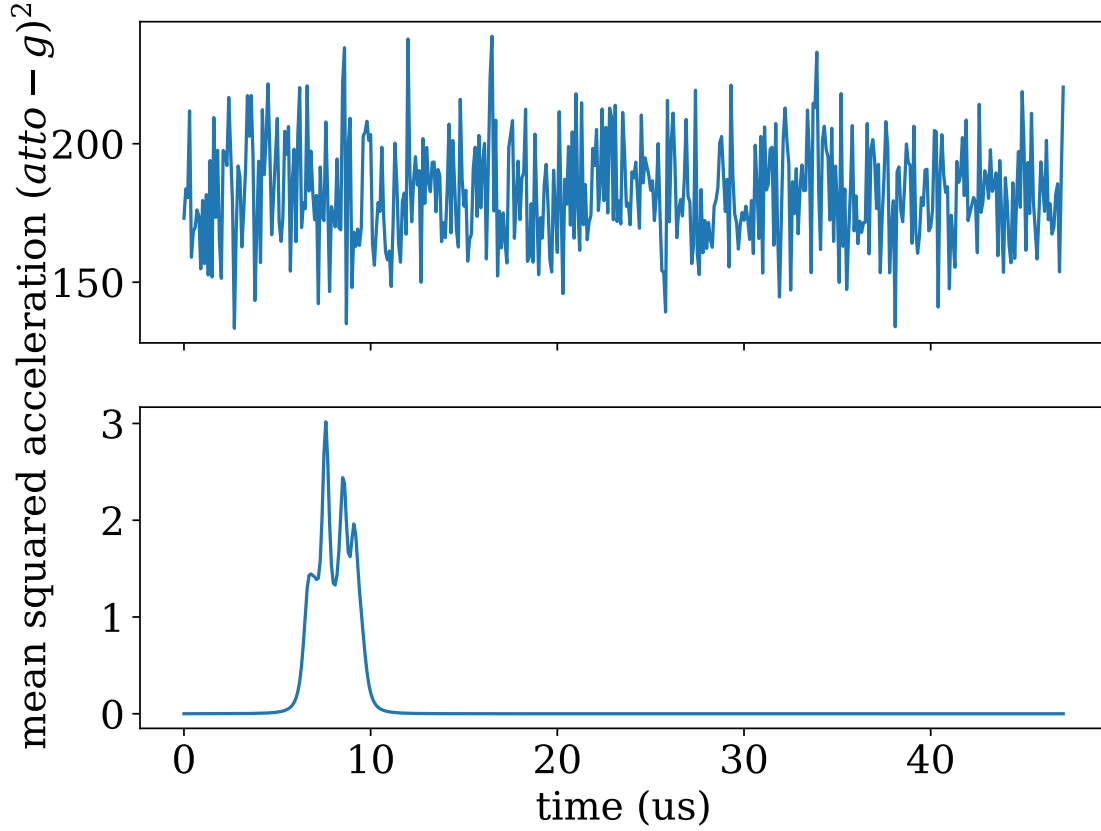


**Figure 4.8.** Top: the mean squared acceleration with noise. Bottom: the mean squared acceleration without noise. It can be seen that if one simply considers the mean squared signal, the signal is not visible above the noise floor.

Tracks are parameterised as described in subsection 4.1.1, with the following 6 parameters: velocity $(v)$, entry time, the spherical coordinates of the entry point $(\cos(\theta_0), \phi_0)$, and the spherical coordinates of the exit point $(\cos(\theta_1), \phi_1)$. The cosine of the $\theta$ angles is used as evenly-spaced bins in $\cos(\theta)$ represent equal-sized areas on a sphere. For every set of parameters, a template is constructed by considering the positions of the dark matter particle

as a function of time, $r(t)$. For the $i^{\text{th}}$ timestep and the $j^{\text{th}}$ sensor, the template is then given by the following:

$$\mathbf{f}_{ij} = \frac{\mathbf{r}_{ij}}{r_{ij}^3} \tag{4.37}$$

This template is multiplied by the data from each sensor at every timestep to obtain the signal strength. The SNR can be computed by dividing the signal strength by the square-root of the noise variance. This is easily computed for white Gaussian noise, as this assumes that noise is uncorrelated between sensors; the total variance given a template is thus simply the variance of each individual data point multiplied by the template values. A full 6-dimensional SNR map of the parameter space produced by template matching unfortunately cannot be printed on a page or displayed on a computer screen; as such, 2D slices of the SNR map are shown in Figure 4.9.
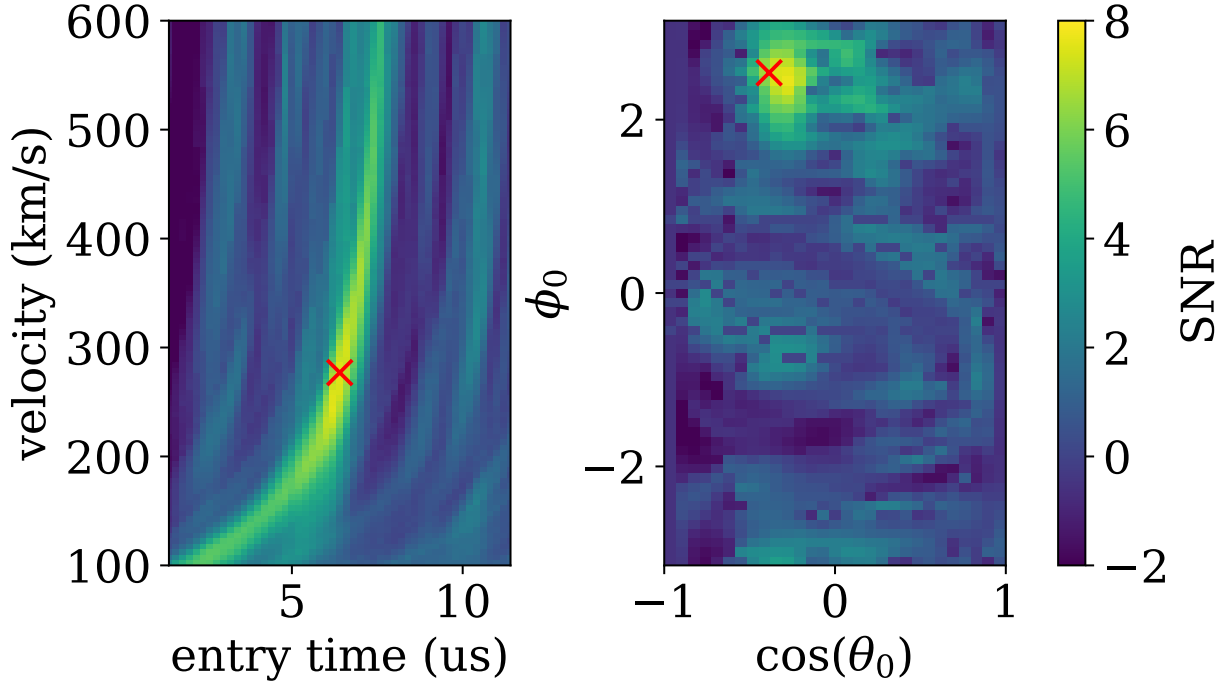


**Figure 4.9.** 2D slices of the significance map obtained from template matching. It can be seen that even though the signal is buried below the noise, as shown in Fig. 4.8, a clear peak around the truth parameter values of the track is clearly visible. These 2D slices are taken by setting all other parameters to the truth values.

We can see that despite the signal being below the noise floor when the data is considered naively, as in Figure 4.8, there is indeed a signal above the noise floor when a technique that accounts for the correlation between data points across sensors and timesteps, such as template matching, is used. In addition, we can see that this method successfully recovers the parameters describing this track as well.

### 4.3.1 Further work

The template matching approach above assumes white noise. For noise which is not constant in frequency, a template would need to be convolved with the reciprocal of the autocorrelation function of the noise; in frequency domain, this can also be understood as dividing the Fourier transformed template by the noise PSD to weigh a search for signals in favour of frequencies where the noise is low [129]. This is not yet implemented, and will need to be implemented in the future for a search for dark matter using a sensor array. Due to the 6-dimensional parameter space and the high sampling rates required, this search is also extremely computationally intensive. To remedy this, I hope to implement an optimiser to compute the highest SNR for each time bin, similar to a profile likelihood [2], using computationally efficient optimisation methods such as Bayesian optimisation [130]. Bayesian optimisation, in particular, can be used in conjunction with maps of the covariance function, as described in chapter 5, to make optimisation even more efficient by removing the need to train covariance function hyperparameters.

### 4.4 Bayesian Track-finding

In this section, I describe the use of Bayesian inference for track-finding. The same track and sensor array configuration described in section 4.3 are used in this section as well. I use the nested sampling with slice sampling [131] as implemented in `ultranest` [132] to compute the posterior distribution of the parameters, and to evaluate the model evidence and determine the significance of a signal.

Nested sampling works iteratively using a collection of 'live points' in the parameter space. The live point with the lowest likelihood is killed each iteration, and becomes a

'dead point'; dead points are then replaced by a new point that is sampled from the prior distribution within the contour defined by the likelihood of the most recent dead point, until pre-determined halting criteria are met [133]. This produces a population of weighted points that represent the posterior distribution together with an estimate of the Bayesian evidence. The reason nested sampling is used for this is that the sampling of complex multi-modal distributions is a key strength of the nested sampling family of methods [131]; as we can see from section 4.3, this is the case for Windchime significance maps.

Bayesian inference involves computing the posterior distribution using a prior distribution and a likelihood function:

$$P(\vec{\theta}|\vec{X}) = \frac{P(\vec{X}|\vec{\theta})P(\vec{\theta})}{P(\vec{X})} \tag{4.38}$$

where $\vec{X}$ refers to the data and $\vec{\theta}$ refers to the parameters. $P(\vec{X}|\vec{\theta}) \equiv \mathcal{L}_{\vec{X}}(\vec{\theta})$ is the likelihood function, and $P(\vec{\theta}) \equiv \pi(\vec{\theta})$ is the prior. $P(\vec{X}) = \int \mathcal{L}_{\vec{X}}(\vec{\theta})\pi(\theta)d(\vec{\theta})$ is the marginal likelihood, or the Bayesian evidence. We can see that we need any algorithm performing Bayesian parameter inference and model comparison to do two things. First, we would like to sample the likelihood function densely in the region with higher probability, and sparsely elsewhere. This is because we are only interested in regions where the likelihood is non-negligible. This doubles as a fitting routine, finding the best-fit region in the parameter space. Secondly, we are interested in the Bayesian evidence, so that our signal model can be compared to a null (signal-free) model.

### 4.4.1 Likelihood function

For each data sample and set of coordinates, the likelihood is constructed under the assumption that each sensor and each data sample represents a random variable that is uncorrelated with all other variables. In this case, the likelihood of the $i^{\text{th}}$ data sample from the $j^{\text{th}}$ sensor in the $\text{k}^{\text{th}}$ axis is:

$$p_{\text{ijk}} \propto e^{-\frac{1}{2\sigma_{\text{ijk}}^2}(a_{\text{ijk}} - \mu_{\text{ijk}}(\vec{\theta}))^2}, \tag{4.39}$$

114

where $a_{\mathrm{ijk}}$ is the measured acceleration value, $\sigma_{\mathrm{ijk}}$ is the standard deviation of the noise distribution, and $\mu_{\mathrm{ijk}}(\vec{\theta})$ is a function describing the expected acceleration measured in the $i^{\mathrm{th}}$ data sample from the $j^{\mathrm{th}}$ sensor in the $k^{\mathrm{th}}$ axis. In this case we consider sensors that are sensitive along all three axes, but the last index can be neglected for sensors that only have one axis of sensitivity. $\mu_{\mathrm{ijk}}(\vec{\theta})$ is produced analogously to the template used in section 4.3, Equation 4.37, as such:

$$\mu_{\mathrm{ijk}}(\vec{\theta}) = \frac{G m_\chi \vec{r}_{ij}}{r_{ij}^3} \cdot \hat{n}_{\mathrm{k}} \tag{4.40}$$

where $\hat{n}_{\mathrm{k}}$ is the unit vector corresponding to the $k^{\mathrm{th}}$ axis of a sensor.

The dataset log-likelihood is thus given by

$$\Lambda(\vec{\theta}) = \sum_{i,j,\mathrm{k}} -\frac{1}{2\sigma_{\mathrm{ijk}}^2}(a_{\mathrm{ijk}} - \mu_{\mathrm{ijk}}(\vec{\theta}))^2 + \log(\mathcal{N}), \tag{4.41}$$

where $\mathcal{N}$ is the normalisation that can be neglected for the purposes of model comparison with a Bayes factor.

### 4.4.2 Prior distribution

Uniform priors are used in all parameters aside from the signal strength parameter. `ultranest` requires priors to be specified by transforming the parameter space to a unit cube, where a uniform prior can be represented by a simple linear map, and the inverse cumulative distribution can be used to encode specific priors [131]. On the other hand, as the signal strength is effectively unbounded, the following equation is used to transform the parameter space $m \in [0, \infty)$ to $\zeta \in [0, 1]$:

$$\zeta = \tanh\left(\frac{m_\chi}{C m_c}\right) \tag{4.42}$$

where $C$ is a numerical constant, and $m_c$ is a characteristic mass relevant to the detector, given by $m_c = \frac{\sigma d^2}{G N^{1/6}}$. This is because we expect the average force to scale as $N^{1/6}$, where $N$ is the number of sensors, and as $\frac{1}{d^2}$, where $d$ is the average sensor spacing [23]. The use of such a transformation allows coverage of the entire parameter space with regularisation towards lower signal strengths, and in the limit of large amounts of data, can make the

inference procedure asymptotically correct from a frequentist perspective as well, due to the Bernstein-von Mises theorem [134], for parameter values that are not close to parameter space boundaries. The prior on the variable $m_\chi$, using the numerical constant $C = 10$, is shown in Figure 4.10.
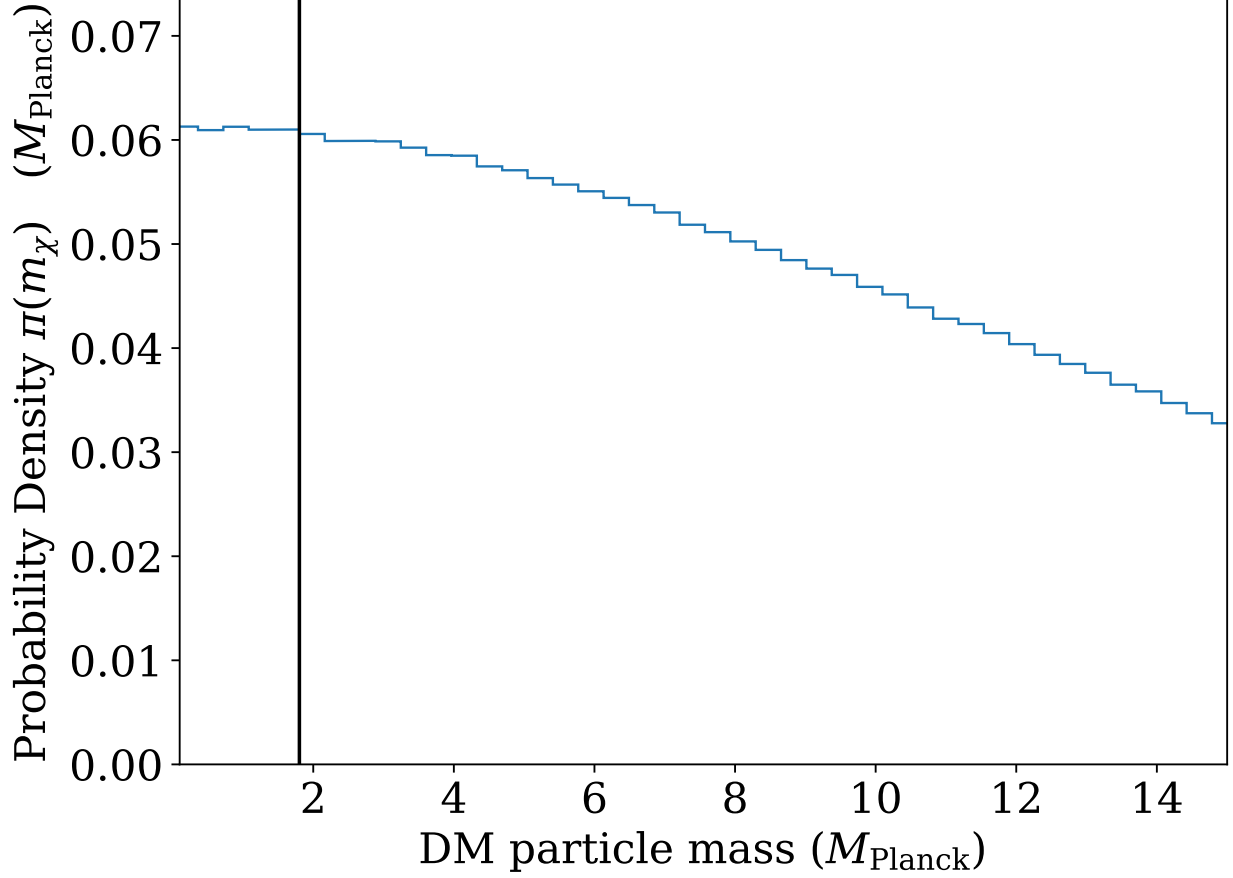


**Figure 4.10.** Prior distribution of $m_\chi$, produced by sampling $5 \times 10^6$ uniform random numbers in the interval $[0, 1]$, and transforming them via the inverse of Equation 4.42.

It can be seen that the prior is flat in the region of parameter space close to the region close to the threshold of sensitivity, $\sim M_{\text{Planck}}$. This ensures that the statistical significance of a result is not biased in the near the sensitivity threshold, where accurate estimation of the significance of a signal is the most crucial.

### 4.4.3 Posterior Distribution from Bayesian Inference

A corner plot of the posteriors is shown below in Figure 4.11. We can see that the parameters are all recovered successfully, and there is a clear peak near the parameter truth values as expected. The Bayes factor is 47800. As a Bayes factor is an odds ratio, this can be interpreted in terms of $\sigma$ [136], corresponding to $4.25\sigma$. The local frequentist p-value can be computed using the likelihood ratio, and is found to be $9 \times 10^{16}$, corresponding to SNR $= 8.0$, or a local significance of $8.0\sigma$. This does not take the look-elsewhere effect into account and overstates the significance; estimating the global significance is the focus of the next section.

### 4.4.4 Estimation of Trial Factor

The method used to estimate the trial factor from a Bayesian posterior is based on [114]. In that paper, it can be seen that in the simple case of a single Gaussian peak in the posterior dominating the trial factor, the trial factor is given by the ratio of the volume of the prior distribution to the volume posterior distribution in all parameters other than the signal strength parameter. This is because the size of the parameter space allowed for the signal strength parameter has no influence on frequentist false positive rates, aside from determining whether limits are one-tailed or two-tailed.

To estimate the trial factor, we start with the likelihood ratio test statistic:

$$q_L(\vec{\theta}) = 2\log\left(\frac{p(\vec{X}|\vec{\theta}, M)}{p(\vec{X}|M_0)}\right) \equiv 2\log(\Lambda(\vec{\theta}))$$
(4.43)

where $M$ is the signal model, and $M_0$ is the null model. If we approximate the posterior as Gaussian, the Bayes factor can be represented in terms of the likelihood ratio! In the following derivation, maximised variables are indicated with a hat, such as $\hat{\Lambda}$ for the maximised likelihood ratio, $\hat{\vec{\theta}}$ for the parameters corresponding to that maximised likelihood ratio, and $\hat{q}_L$ for the corresponding test statistic.

The Bayes factor is defined as

$$B = \frac{\int d\vec{\theta}\, p(\vec{X}|\vec{\theta}, M)p(\vec{\theta}|M)}{\int d\vec{\theta}_0\, p(\vec{X}|\vec{\theta}_0, M_0)p(\vec{\theta}_0|M_0)}.$$
(4.44)

117
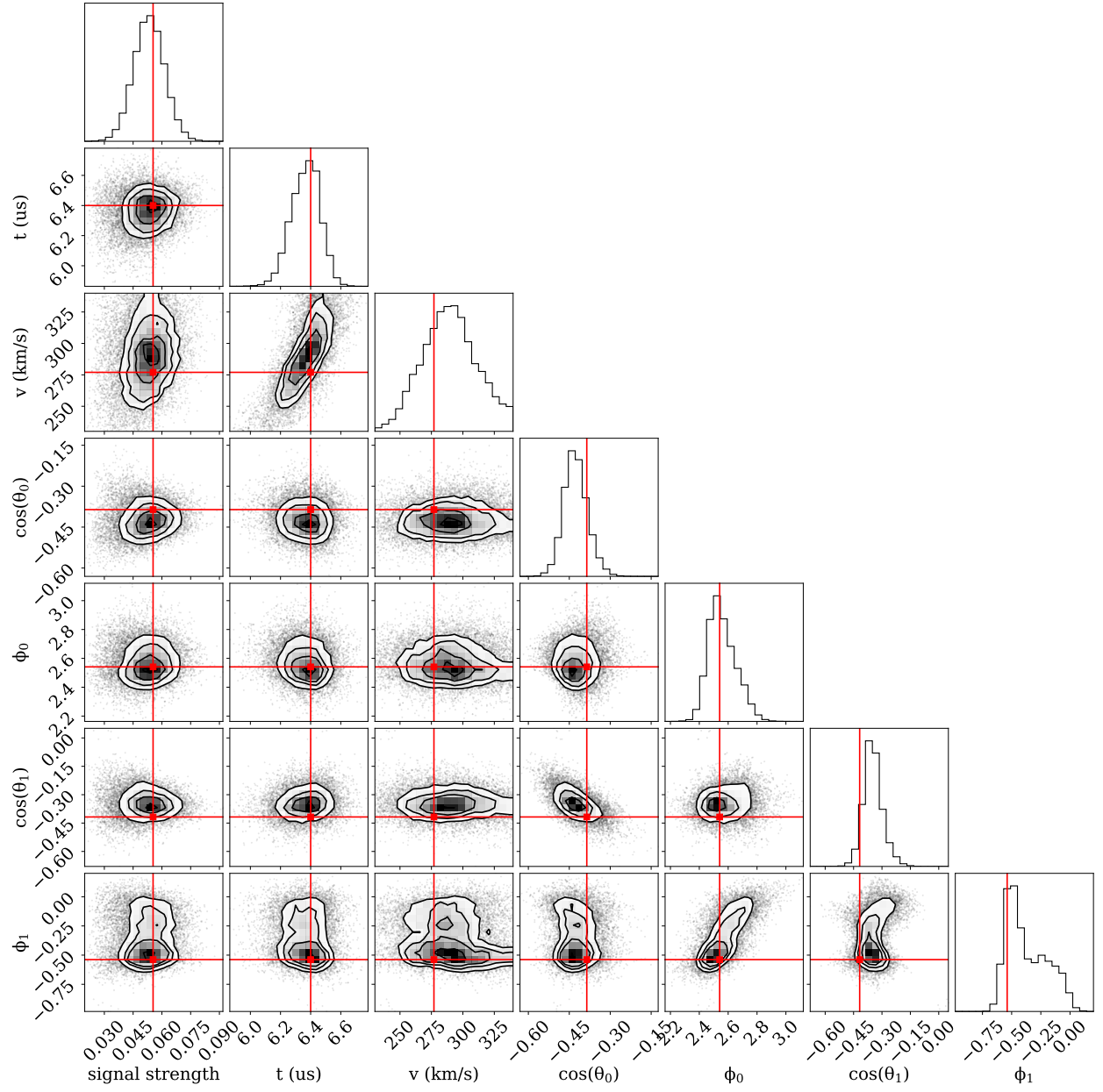
**Figure 4.11.** A corner plot showing that the truth value can be recovered with a full 6-dimensional search. The 1, 2, 3 and $4\sigma$ contours are shown. In 2D histograms as shown here, these correspond to 39%, 86%, 99% and 99.97%, because the probability content of $\sigma$-levels depend on dimensionality [2]. Made with `corner` [135].

This can be simplified when the signal-free model is a point hypothesis with parameters as such:

$$B = \frac{\int d\vec{\theta} p(\vec{X}|\vec{\theta}, M) p(\vec{\theta}|M)}{p(\vec{X}|M_0)} \tag{4.45}$$

We can separate the signal strength parameter and the other parameters as $\vec{\theta} = (\vec{\phi}, s)$. Under the assumption that the prior is flat, we can obtain:

$$B = \frac{\int ds \int d\vec{\phi} p(\vec{X}|\vec{\phi}, s, M) \frac{1}{V_{\text{prior}}}}{p(\vec{X}|M_0)} \tag{4.46}$$

If we then assume that posterior distributions are Gaussian, and that the signal strength posterior is uncorrelated to other posteriors, we get the following:

$$
\begin{aligned}
B &= \frac{\hat{\Lambda}}{V_{\text{prior},s} V_{\text{prior},\phi}} \int ds \int d\vec{\phi} e^{-\frac{1}{2}(\vec{\phi}-\hat{\vec{\phi}})^T \Sigma^{-1}(\vec{\phi}-\hat{\vec{\phi}})} e^{-\frac{1}{2}\left(\frac{s-\hat{s}}{\sigma_s}\right)^2} \\
&= \frac{\hat{\Lambda}}{V_{\text{prior},s} V_{\text{prior},\phi}} \sqrt{(2\pi)^k |\Sigma|} \sqrt{(2\pi)\sigma_s^2} \\
&= \hat{\Lambda} \frac{V_{\text{posterior},s} V_{\text{posterior},\phi}}{V_{\text{prior},s} V_{\text{prior},\phi}}
\end{aligned} \tag{4.47}
$$

This works because in taking the ratio of the evidence for the two models, the normalising constants cancel out. Assuming that the signal strength is uncorrelated is reasonable because one would typically not expect the shape parameters of a signal to depend strongly on the signal strength, though in practice this would need to be verified by Monte-Carlo simulations. In Equation 4.47, the trial factor is given by $\frac{V_{prior,\phi}}{V_{posterior,\phi}}$ [114]. The relation between the Bayes factor and maximum likelihood ratio is then given by

$$\log(B) = log(\hat{\Lambda}) + log\left(\frac{V_{\text{posterior},s}}{V_{\text{prior},s}}\right) + \log\left(\frac{V_{\text{posterior},\phi}}{V_{\text{prior},\phi}}\right), \tag{4.48}$$

whereas the trial factor is given by

$$\log(N_{trials}) = -log\left(\frac{V_{\text{posterior},\phi}}{V_{\text{prior},\phi}}\right) = -\log(B) + \log\left(\frac{V_{\text{posterior},s}}{V_{\text{prior},s}}\right) + log(\hat{\Lambda}). \tag{4.49}$$

We have thus shown that under the above assumptions, the trial factor can be obtained if we know the Bayes factor, the maximum likelihood ratio, and the prior to posterior volume ratio of the signal parameter. This is simplified by the fact that the prior volume of the signal parameter is simply 1 in our case, due to the transformation described in the previous sections. $V_{posterior,s}$, on the other hand, is simply given by the standard deviation of the signal strength parameter.

From this derivation, we can see that while Bayesian model comparison using the Bayes factor does automatically account for the look elsewhere effect due to the considered parameter space, it is not a panacea; Bayesian methods do not distinguish between amplitude parameters and other parameters. There is a good reason for this distinction in frequentist methods, however, as for rare event searches we are concerned with the false-positive rate due to backgrounds and noise. The false positive rate should not depend on the size of the signal strength parameter space.

It should be noted that this is only valid when the posterior is dominated by a single mode. However, it is likely that in the regime we are working in, the posterior would be locally dominated by a single mode if there were to be a real signal, as we need a false-positive rate on the order of 1 event/year or lower, making this approximation reasonable. The derivation also assumes a flat prior. While not strictly true in our case, the prior is locally flat in the region near the sensitivity threshold of the detector; as such, this holds in the region we are interested in. The trial factor estimate might be biased for signals that are far above our sensitivity threshold, but as the look elsewhere effect is unimportant far away from the sensitivity threshold, this should not matter.

Using the above derivation, we can obtain a trial factor of $N_{\mathrm{trials}} = 4.5 \times 10^7$. The global significance can be derived as such:

$$p_{\mathrm{global}} \approx p_{\mathrm{local}} N_{\mathrm{trials}} \tag{4.50}$$

This gives a final global significance of $5.5\sigma$ for the above track. It should be noted that this is for a search time of $8\,\mathrm{us}$. Assuming the trial factor scales linearly with time as one would intuitively expect, the trial factor is $2.4 \times 10^{20}\,\mathrm{yr}^{-1}$. This implies that to get a global

120

significance of $3\sigma$ for a 1 year exposure time, a signal with SNR $= 10$ is needed; stated another way, for a rare event search with 64 sensors and a 1 year exposure time, the SNR threshold needs to be at least 10. The trial factor derived using this method is an estimate, as the resultant posterior distribution exhibits non-Gaussian behaviour (see Figure 4.11).

### 4.4.5   Further work

Computational cost is a key issue for this approach as well. One key issue is that at low values of the signal strength parameter $\zeta$, the likelihood is effectively independent of parameters other than signal strength. This causes difficulties with both nested sampling and Markov chain Monte Carlo, and is analogous to the difficulties encountered in sampling hierarchical models, typified by Neal's funnel [137, 138]. A typical approach to solve this is to consider a transformation of the parameter space that eliminates or reduces this funnel structure, and will be explored in future work. Another approach could also be to partition the parameter space into portions that individually are not as challenging to sample.

In addition, a likelihood function for noise that is not constant in frequency has to be developed. This can use the Whittle likelihood, an approximate likelihood for coloured noise that is also the basis for the matched filtering method mentioned in section 4.3 [139]. Finally, the estimation of the trial factor can be extended to larger arrays by considering the scaling of the resolution of a sensor array with array size, and will be helpful to extend the trial factor estimate given here to larger sensor arrays.

### 4.5   Likelihood Ratio for Ultralight Dark Matter Searches

### 4.5.1   The Signal from Ultralight Dark Matter

In addition to ultra-heavy dark matter, a large array of accelerometers will also be sensitive to coherent signals, such as various types of ultralight dark matter [125]. One model of ultralight dark matter that we are focusing on is $B - L$ dark matter, which is dark matter that couples to the baryon number minus the lepton number, or the $B - L$ charge. For dark matter with masses lighter than $\sim 0.1\,\mathrm{eV}$, the dark matter signal can be expected to be a coherent sinusoidal signal due to the high particle density, with the frequency given by

121

the dark matter mass [125]. This is because dark matter has a typical velocity of $\sim 10^{-3}c$ (see chapter 1), hence the energy corresponding to the rest mass is much higher than the kinetic energy. For a neutral object, the number of protons and electrons is the same, hence the $B-L$ charge is given by the neutron number of a sensor test mass. The force signal on a sensor is thus given by [125]:

$$F \approx g_{B-L}(A-Z)F_0 \sin(\omega_\phi t + \phi_0) \tag{4.51}$$

where $g_{B-L}$ is the dimensionless $B-L$ coupling, $A$ is the mass number, $Z$ is the atomic number, $\omega_\phi \approx \frac{mc^2}{\hbar}$ is the frequency of the signal, and $F_0 = \sqrt{\frac{2e^2\rho_\chi}{\epsilon 0}} \approx 6 \times 10^{-16}\,\mathrm{N}$ is the force on a single neutron if the coupling is $g_{B-L} = 1$ [140]. It should be noted that this equation, as given in [125], is approximate as it does not account for the polarisation of the signal.

This force is applied on every object, however, and hence only the differential acceleration can be detected. This differential acceleration is due to the fact that the neutron content is material dependent. The acceleration from $B-L$ dark matter is can be found by dividing Equation 4.51 by the sensor mass:

$$\begin{aligned}
a &\approx g_{B-L}\frac{A-Z}{m_s}F_0 \sin(\omega_\phi t + \phi_0) \\
&\approx g_{B-L}\frac{A-Z}{m_n A}F_0 \sin(\omega_\phi t + \phi_0) \\
&= g_{B-L}\frac{A-Z}{A}a_0 \sin(\omega_\phi t + \phi_0)
\end{aligned} \tag{4.52}$$

where $a_0 = \frac{F_0}{m_n}$ is the acceleration on a single neutron if the coupling is $g_{B-L} = 1$. The differential acceleration between materials 1 and 2 is therefore

$$a_{\mathrm{diff}} \approx g_{B-L}\Delta \sin(\omega_\phi t + \phi_0) \tag{4.53}$$

where $\Delta = \left(\frac{Z_1}{A_1} - \frac{Z_2}{A_2}\right)$ is the difference between the neutron-to-nucleon numbers between two materials. For typical materials, $\Delta \lesssim 0.1$. This differential acceleration can be detected either by comparing the acceleration from test masses with different materials, or by detecting the

differential acceleration between a test mass and the readout system, such as a pickup loop or an interferometer.

### 4.5.2 Derivation of the Likelihood Function

Let $\{X_n : n \in T\}$ be a set of $N$ measurements representing a real wide-sense stationary Gaussian time series with zero mean and autocorrelation function $K(j)$ where $j$ is the difference between the indices of two measurements. The time between subsequent measurements is $\tau$. This can be done with no loss of generality, as the mean of any wide-sense stationary Gaussian process can be subtracted to satisfy this condition. The discrete Fourier transform of this time series is

$$\tilde{X}_k = \frac{1}{\sqrt{N\tau}} \sum_{n=0}^{N-1} X_i e^{-\frac{i2\pi}{N}kn}. \tag{4.54}$$

As the expectation of each $X_n$ is zero, the expectation of $\tilde{X}_k$ is zero. The real and imaginary components are independently distributed Gaussian random variables $\Re\left(\tilde{X}_k\right) \sim \mathcal{N}(0, \sigma_k^2)$ and $\Im\left(\tilde{X}_k\right) \sim \mathcal{N}(0, \sigma_k^2)$, except for $k = 0$, and $k = N/2$ if $N$ is even [139]. This is the Whittle approximation, and is asymptotically correct as $N$ increases, as long as the autocorrelation function satisfies $\sum_{j=-\infty}^{\infty} |K(j)||j|^{1/2} < \infty$ and $E(X_n^4) < \infty$ [141]. A formal derivation can be found in pg. 348 of [142]. The independence and equal variance of the real and imaginary components is required because otherwise the system would not be invariant to a shift in phase [139].

For an ultralight dark matter search, we are not interested in the edges of frequency space where $k = 0$ and $k = N/2$, thus they will be neglected for the following derivation. As the real and imaginary components of $\tilde{X}_k$ are independent, the random variable $|\tilde{X}_k|^2$ is given by $\left(\Re\left(\tilde{X}_k\right)^2 + \Im\left(\tilde{X}_k\right)^2\right)$. As $|\tilde{X}_k|^2$ is the sum of 2 independent identically distributed Gaussian random variables, if it is normalised by the variance, $\sigma_k^2$, it is described by a $\chi^2$ distribution with 2 degrees of freedom: $\frac{|\tilde{X}_k|^2}{\sigma_k^2} \sim \chi_2^2$. In the limit of $N \to \infty$, $\sigma_k^2 \approx S(\omega_k)$, the PSD of the stationary process. The null (signal-free) likelihood at a single frequency is thus given by

$$\mathcal{L}_{0,k} = \chi_2^2 \left(\frac{|\tilde{X}_k|^2}{S(\omega_k)}\right). \tag{4.55}$$

Negative frequencies are not included, because the absolute value of the Fourier transform is the same.

If there is a sinusoidal signal present at frequency $\omega_\kappa$, the expectation of $\tilde{X}_\kappa$ will instead be given by a phasor describing the sinusoidal signal, $Ae^{i\theta}$. As the phase of a dark matter signal is unknown, a signal likelihood should not involve $\theta$; as such, likelihood in complex space would not do. In this scenario, $\Re\left(\tilde{X}_\kappa\right) \sim \mathcal{N}(\Re(Ae^{i\theta}), \sigma_\kappa^2)$ and $\Im\left(\tilde{X}_\kappa\right) \sim \mathcal{N}(\Im(Ae^{i\theta}), \sigma_\kappa^2)$. As such, $\mathrm{E}(|\tilde{X}_\kappa|^2) = \Re(Ae^{i\theta})^2 + \Im(Ae^{i\theta})^2 = A^2$. As $|\tilde{X}_\kappa|^2$ is now given by the sum of two independent Gaussian random variables, it is described by a non-central $\chi^2$ distribution: $\frac{|\tilde{X}_\kappa|^2}{\sigma_\kappa^2} \sim f_{nc}(2, \frac{A^2}{\sigma_\kappa^2})$ where $f_{nc}(\nu, \lambda)$ refers to a non-central $\chi^2$ distribution with $\nu$ degrees of freedom and non-centrality parameter $\lambda$ [143]. The signal model likelihood of a single frequency is thus given by

$$\mathcal{L}_k(A) = f_{nc}\left(\frac{|\tilde{X}_k|^2}{S(\omega_k)}; 2, \frac{A^2}{\sigma_k^2}\right) \tag{4.56}$$

where $A$ is the fit parameter for the amplitude of a signal.

The likelihood ratio test statistic is:

$$\Lambda_k(A) = -2\log\left(\frac{\mathcal{L}_{0,k}}{\mathcal{L}_k(A)}\right). \tag{4.57}$$

As Equation 4.55 is a special case of Equation 4.56, Wilks' theorem can apply to this likelihood ratio test. However, as the null model lies on the boundary of the parameter space, the asymptotic distribution of the likelihood ratio is given by $\frac{1}{2}\chi_1^2(\Lambda) + \delta(\Lambda)$, instead of $\chi_1^2(\Lambda)$ [144].

### 4.5.3 Further Work

The signal likelihood Equation 4.56 does not account for the stochastic nature of the dark matter signal, or the broadening of the dark matter signal due to the standard halo model [145]. As such, for searches of dark matter longer than one coherence time, a likelihood that accounts for these effects would be needed, and will be the subject of future work.

## 4.6    Conclusion

The Windchime project aims to use mechanical accelerometers to detect ultra-heavy dark matter via gravitational couplings, with a secondary goal of searching for ultralight dark matter. In this chapter, I have discussed methods to compute sensitivity projections for the Windchime project, frequentist and Bayesian approaches for track-finding below the single-sensor noise floor, and the construction of a likelihood ratio for the search of ultralight dark matter. The work detailed in this chapter represents foundational work for the data analysis and science goals of the Windchime project. I hope this work, combined with work on instrumentation and ultralight dark matter sensitivity projections analysis by the rest of the collaboration, will enable either a discovery of dark matter or a ruling out of the relevant parameter space in the future.

# 5. FAST ESTIMATION OF THE LOOK-ELSEWHERE EFFECT USING GAUSSIAN RANDOM FIELDS

*This work is a paper manuscript that is intended to be published shortly after the submission of this thesis.*

## 5.1 Introduction

In hypothesis testing problems with composite hypotheses, the correct frequentist p-value might not be the same as the p-value one would compute for fixed values of the composite hypothesis parameters [2]. This is referred to as the look-elsewhere effect. The correct p-value given composite hypotheses is often termed the global p-value, whereas the p-value computed with fixed parameters is termed the local p-value. The look-elsewhere effect correction is often parameterised by a trial factor, which is the ratio between the local and global p-values [146]. A simple approach to finding the trial factor would be to run a large number of null-hypothesis Monte-Carlo simulations, often using simplified or "toy" models. These simplified simulations are known as toy MCs. An example of this approach can be found in [35].

However, in the case of complex and high-dimensional problems, the use of toy MCs can be computationally too expensive. In addition, data-analysis and inference of modern experiments can be extremely computationally-intensive, requiring dedicated computational infrastructure. This makes estimation of trial factors for the purposes of sensitivity projections for future experiments difficult. Thus, the use of Gaussian random fields to directly generate null significance maps and estimate the trial factor can be very useful.

Gaussian random fields are random functions over a domain, where the values of every finite collection of points on the domain are described by a multivariate Gaussian distribution. Such fields can be viewed as a higher-dimensional generalization of Gaussian processes, commonly used in Gaussian process regression [147]. Gaussian random fields are used for the estimation of the look-elsewhere effect in neuroimaging [148], and for the modelling of the matter distribution in the universe [149]. There has been existing work regarding the use of Gaussian random fields for the estimation of the look-elsewhere effect in physics [150, 151].

The use of Gaussian random fields for estimation of look-elsewhere effect corrections relies on computations of the excursion probability, which is the probability for samples of a Gaussian random field to exceed a given significance level. In this chapter, we detail techniques to use Gaussian random fields for the estimation of look-elsewhere effect corrections, with a focus on problems with underlying Gaussian random variables.

A discussion of the classes of problems that can be modelled by Gaussian random fields, an overview of the spectral method for efficient sampling of Gaussian random fields, and an analytic approximation for the excursion probability can be found in section 5.2. A demonstration of these methods using a 2-dimensional template-matching problem with a Gaussian kernel can be found in section 5.3, and a demonstration using a 1-dimensional template-matching problem with a non-Gaussian kernel can be found in section 5.4. Finally, in section 5.5, these methods are used to estimate the trial factor when searching for dark matter tracks using an accelerometer array.

## 5.2 Statistical underpinnings of method

This section is split into 3 parts. First, an explanation for why Gaussian random fields correctly model the significance maps of a large set of problems is given in subsection 5.2.1. Second, a discussion regarding how to sample Gaussian random fields efficiently is given in subsection 5.2.2. Finally, subsection 5.2.3 contains a description of a fitting procedure that can be used to extend this method to extremely small p-values using an analytic approximation of the excursion probability of a Gaussian random field.

### 5.2.1 Why Gaussian Random Fields Can Model a Large Set of Problems

Let us consider a statistical problem where one searches for a fluctuation over finely-spaced set of Gaussian random variables distributed in a parameter space. One example of this could be a template matching search for a transient over a regular grid of CCD pixels with Gaussian noise. A diagram of this is shown in Fig. 5.1.
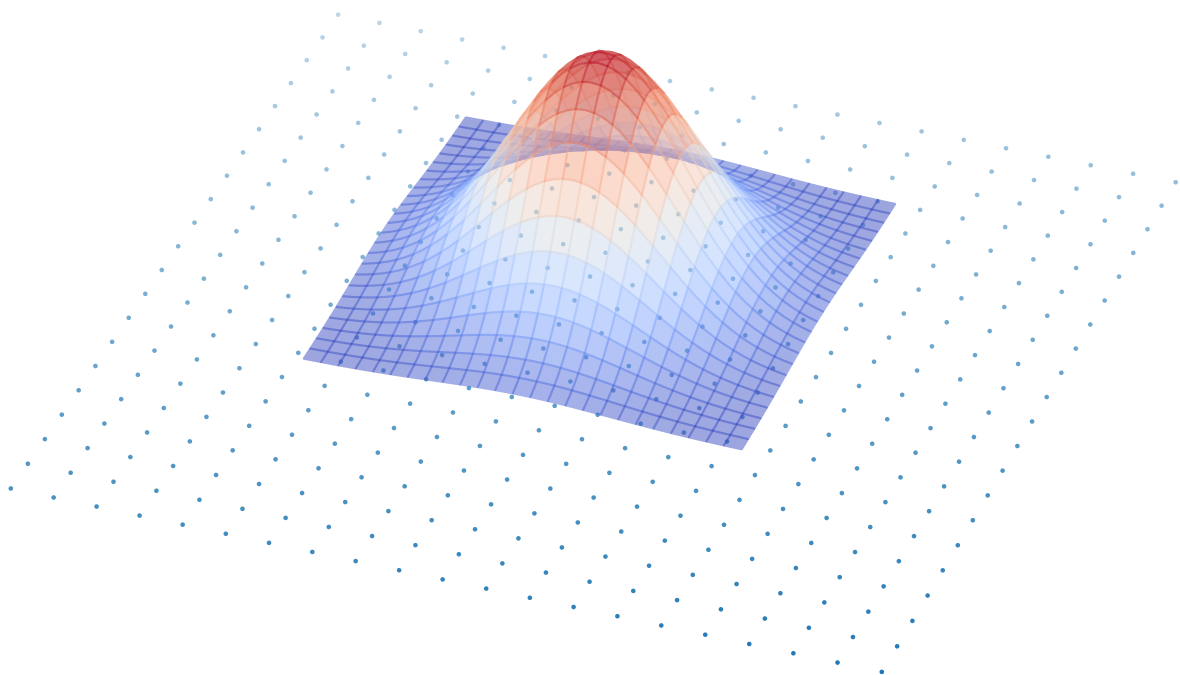
**Figure 5.1.** Diagram depicting a template matching search for an excess over a grid of random variables. The grid of random variables is indicated by the blue points, and the template used to search for an excess is shown in the coloured wire-frame distribution.

While a 2D grid with a simple template that is symmetric and does not vary with position is depicted in Fig. 5.1, this is for ease of illustration, and these assumptions are not made in the following argument except where noted. We can see that at each possible template position, the resultant signal strength recovered is a weighted sum of Gaussian random variables, where the weights correspond to the template amplitude at a given random variable. The significance map formed using such a template thus corresponds to the formal definition of a random field [152] where each point is Gaussian-distributed, and every collection of points represent a multivariate Gaussian distribution.

In addition, given independent underlying random variables, the covariance between two points can be computed from the template directly. Consider two points in the parameter space, $(\mathbf{x_0}, \mathbf{x_1})$. At each point, the random variable in the case of a signal-free dataset is given by:

$$Y_i = \sum_j \alpha_{i,j} X_j \tag{5.1}$$

where $X_j$ are the underlying finely spaced Gaussian random variables such as CCD pixels, and $\alpha_{i,j}$ refers to the template value at each underlying random variable for template $i$. $E(X_j) = 0$ is taken without loss of generality as the mean value can be subtracted. As such, the covariance would be given by:

$$
\begin{aligned}
K(\mathbf{x_0}, \mathbf{x_1}) &= \mathrm{cov}\left(\sum_j \alpha_{0,j} X_j, \sum_k \alpha_{1,k} X_k\right) \\
&= \mathbb{E}\left(\left(\sum_j \alpha_{0,j} X_j\right)\left(\sum_k \alpha_{1,k} X_k\right)\right)
\end{aligned}
\tag{5.2}
$$

This can be taken further if the underlying Gaussian random variables are independent, as then $\mathbb{E}(X_i X_j) = 0$ for $i \neq j$. The covariance can then be computed as such:

$$
\begin{aligned}
K(\mathbf{x_0}, \mathbf{x_1}) &= \mathbb{E}\left(\left(\sum_j \alpha_{0,j} X_j\right)\left(\sum_k \alpha_{1,k} X_k\right)\right) \\
&= \mathbb{E}\left(\sum_j \alpha_{0,j} \alpha_{1,j} X_j^2\right) \\
&= \sum_j \alpha_{0,j} \alpha_{1,j} \sigma_j^2
\end{aligned}
\tag{5.3}
$$

We can thus see that in the case of template matching with underlying Gaussian random variables, the significance map is modelled by a Gaussian random field and the covariance function can be directly calculated based on the template and measured properties of the underlying random variables. In addition, Gaussian random fields can also be used to model significance maps with underlying Gaussian random variables generated with likelihood ratio tests. This is because the log likelihood-ratio is simply the sum of squared residuals normalised by the standard deviation, as shown in Equation 5.4.

$$
\begin{aligned}
\Lambda &= \log\left(\frac{\hat{\mathcal{L}}}{\mathcal{L}_{\prime}}\right) \\
&= \sum_i \frac{-\left(X_i - \mu_i\right)^2}{2\sigma} - \sum_i \frac{-\left(X_i\right)^2}{2\sigma} \\
&= \sum_i \frac{2\mu_i X_i - \mu_i^2}{2\sigma}
\end{aligned}
\tag{5.4}
$$

In addition to the above, other problems that do not use underlying Gaussian random variables can still be represented approximately by Gaussian random fields in some circumstances. Where a likelihood ratio test is used the distribution of the test statistic asymptotically approaches a $\chi^2$ distribution due to Wilks' theorem when the relevant conditions, detailed in [144], are satisfied. In such a situation, a signal-free significance map over a parameter space would represent a $\chi^2$ random field [150]. While this differs from a Gaussian random field, because a $\chi^2$ random variable can be defined by the square of a Gaussian random variable, where the degrees of freedom of the relevant $\chi^2$ random field is $k = 1$, such a $\chi^2$ random field can be sampled simply by sampling a Gaussian random field with the correct covariance and squaring it, and the excursion probability of such a random field is simply double the one-sided excursion probability described in subsection 5.2.3. The fact that a $\chi^2$ random field can be represented using Gaussian random field is also noted by Ananiev and Read in [151].

It should also be noted that due to Lindeberg and Lyapunov's central limit theorems, if the underlying random variables are independent and sufficiently finely distributed to give a large sample size, this argument holds for non-Gaussian underlying random variables such as Poisson noise as long as Lindeberg's condition or Lyapunov's condition are satisfied [153]. While a detailed discussion of these conditions is beyond the scope of this paper, verifying the

Gaussianity of a given significance map numerically or constraining it using the Berry-Esseen theorem [154] might be sufficient for practical purposes.

### 5.2.2 Efficient Spectral Sampling of Stationary Gaussian Random Fields

While for sufficiently complex problems Gaussian random fields might be easier to sample than toy MC-based methods, this might still be too computationally intensive. For example, if we consider template-matching search in a flat 2-dimensional parameter space with $10^2$ bins per dimension, there would be $10^4$ points that need to be correlated with each other, resulting in a correlation matrix with $10^8$ entries. We can see that with higher dimensional problems, populating such a covariance matrix which is needed for naive sampling of Gaussian random fields quickly becomes intractable.

A review of efficient methods for the sampling of Gaussian random fields by Liu et al. can be found in [155]. In sections 5.3 and 5.5, the spectral method as described in [155] is used to efficiently sample from Gaussian random fields. This method of generating samples from a Gaussian random field requires the field to be weakly stationary, such that a covariance function can be described by a function of the displacement between two points, such that:

$$K(\mathbf{x_0}, \mathbf{x_1}) \equiv K_s(\mathbf{x_0} - \mathbf{x_1}) \tag{5.5}$$

$K_s(\mathbf{d})$ is simply the autocorrelation function multiplied by the variance. For a field with unity variance, which is typical for a significance map that is scaled to represent the signal-to-noise ratio (SNR), then, $K_s(\mathbf{d})$ is the autocorrelation function. This case is considered without loss of generality, as one can scale any stationary Gaussian random field to have a variance of unity. The Fourier transform of the autocorrelation function of a weakly stationary process is the power spectral density (PSD) due to the Wiener-Khinchin theorem [119, 156].

The spectral method for sampling Gaussian random fields makes use of this Fourier transform pair. Samples of a Gaussian random field can be generated in frequency domain by multiplying the Fourier transform of white noise by the square root of the PSD, then performing an inverse Fourier transform to return the sample to the relevant parameter space.

We can thus sample stationary Gaussian random fields in high-dimensional parameter spaces without having to populate extremely large covariance matrices.

### 5.2.3 Analytic Approximation of Excursion Probability

Even when sampling Gaussian random fields with the spectral method, in high-dimensional parameter spaces, sampling can still be prohibitively expensive due to the curse of dimensionality. In this scenario, the look-elsewhere effect correction can be extended to lower p-values using an analytic approximation of the excursion probability. For a random field $\{f(t) : t \in M\}$, the excursion probability over a level $u$ is defined as:

$$p_{\text{excur}} = \mathbb{P}\left\{\sup_{t \in M} f(t) \geq u\right\} \tag{5.6}$$

It can be seen that the excursion probability represents the probability that any point on a random field exceeds $u$. The excursion probability for a smooth Gaussian random field on a locally convex space is given by [152]:

$$\begin{aligned}
p_{\text{excur}} =& C_0 \Phi\left(\frac{u}{\sigma}\right) + u^N e^{-u^2/2\sigma^2} \sum_{j=1}^{N} C_j u^{-j} + \\
& \mathcal{O}\left(e^{-\alpha u^2/2\sigma^2}\right)
\end{aligned} \tag{5.7}$$

where $\Phi(u)$ is the Gaussian tail distribution, $N = \dim(M)$, $\sigma$ is the standard deviation of the Gaussian random field, and $\alpha > 1$ is a constant describing the exponential suppression of the error term. We can see that Equation 5.7 contains a number of constants $(C_i)$. While these constants can be computed directly for some cases, this is often non-trivial [152]. Instead, Equation 5.7 can be used to fit the excursion probability directly using a set of samples of signal-free significance maps. This, combined with the spectral method of sampling Gaussian random fields shown in subsection 5.2.2, greatly reduces the computational cost of computing look-elsewhere effect correction. It should be noted that Equation 5.7 is based on approximating the excursion probability using the Euler characteristic of an excursion set, thus for particularly computationally challenging problems methods from [150] for estimating

the Euler characteristic can further reduce the number of samples needed to derive the look-elsewhere effect correction.

## 5.3  Demonstration with a 2D Toy Problem

The ideas introduced in section 5.2 can be first demonstrated using a search in a 2D parameter space. Here, we will model a 2D template matching search using a 2D Gaussian random field. 2D Gaussian random fields can be used to model the look-elsewhere correction for various experiments, such as searches for dark matter using pixel detectors [54, 157] and searches for astronomical transients [158, 159].

The expected signal shape and hence the template matching kernel are modelled using a Gaussian kernel. In such a situation, the normalised covariance function or the correlation function, is also a Gaussian kernel with double the covariance matrix and $\sqrt{2}$ the linear dimensions, as shown in Figure 5.2.

This can be seen by expanding Equation 5.3 in the case of a position independent kernel as such:

$$K(\mathbf{x_0}, \mathbf{x_1}) = \sum_j \alpha(\mathbf{x_0}, \vec{x}_j)\alpha(\mathbf{x_1}, \vec{x}_j)\sigma_j^2 \tag{5.8}$$

where $\alpha(\mathbf{x_0}, \vec{x}_j)$ is the template weight for a sample at $x_j$, and a template at $x_0$. For the case of a stationary field, $\sigma_j$ is the same for all $j$, so we simply call this $\sigma$. Then, taking the template function to be a Gaussian with covariance $\Sigma$, we can apply the continuum approximation if each data samples takes up a volume of $V_\mathrm{s}$ to derive the following:

$$\begin{aligned}
K(\mathbf{x_0}, \mathbf{x_1}) =& \sigma^2 \sum_j \alpha(\mathbf{x_0}, \vec{x}_j)\alpha(\mathbf{x_1}, \vec{x}_j) \\
\approx& \frac{\sigma^2}{V_s} \int \alpha(\mathbf{x_0}, \vec{x})\alpha(\mathbf{x_1}, \vec{x})d\vec{x} \\
=& \frac{\sigma^2}{V_s} \int e^{(\mathbf{x_0}-\vec{x})^T\Sigma^{-1}(\mathbf{x_0}-\vec{x})}e^{(\mathbf{x_1}-\vec{x})^T\Sigma^{-1}(\mathbf{x_1}-\vec{x})}d\vec{x}
\end{aligned} \tag{5.9}$$
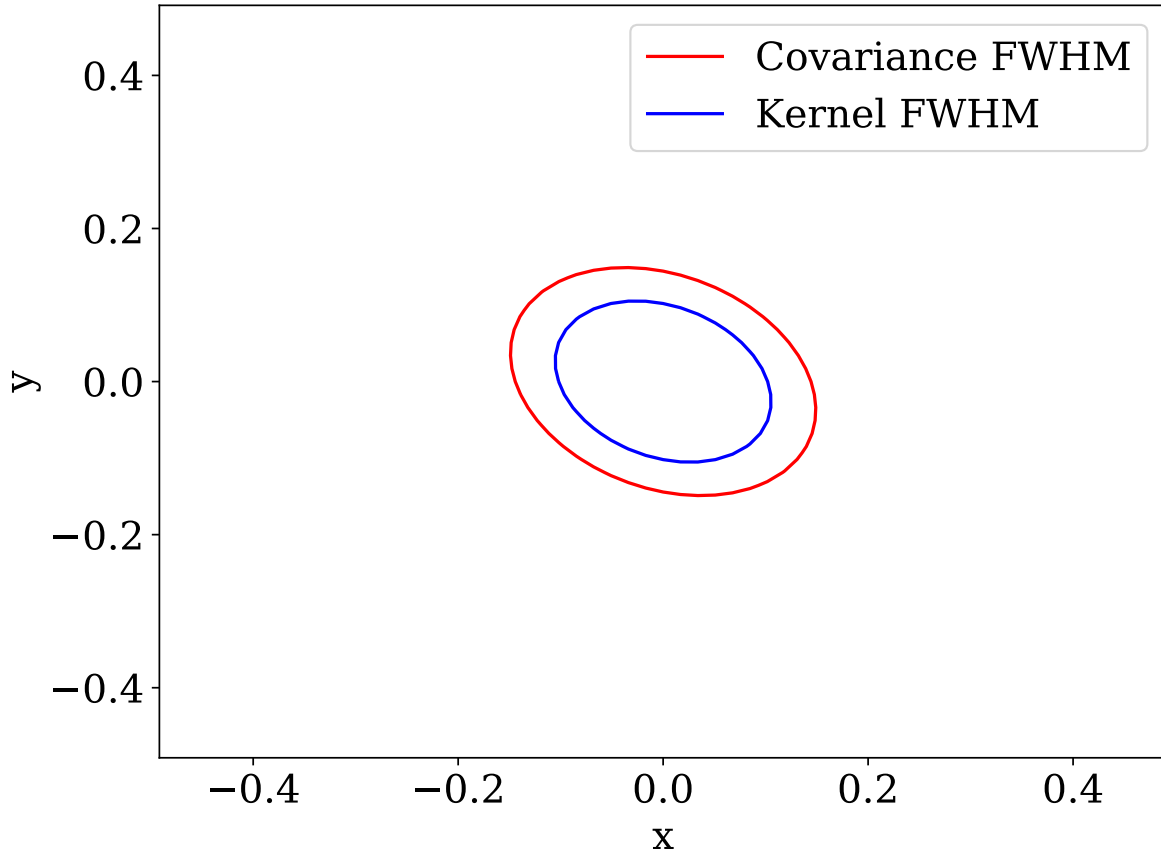
**Figure 5.2.** 2D toy problem template matching kernel and covariance function. The FWMN ellipse corresponding to the covariance function is $\sqrt{2}$ bigger than that of the kernel in linear dimension.

We can see that this is linearly proportional to the convolution of two Gaussian distributions. It is a well known result that the convolution of Gaussian distributions is Gaussian, with a covariance matrix that is the sum of the covariance matrix of the individual Gaussian random variables; this is because the sum of two Gaussian random variables is Gaussian [156]. Thus, if the templates in a search are Gaussian, the resulting Gaussian field from the template search has the covariance function shown in Equation 5.10.

$$K(\mathbf{x_0}, \mathbf{x_1}) = K_s(\mathbf{x_0} - \mathbf{x_1}) \propto e^{(\mathbf{x_0}-\mathbf{x_1})^T \Sigma'^{-1} (\mathbf{x_0}-\mathbf{x_1})} \tag{5.10}$$

where $\Sigma' = 2\Sigma$. One can then compute the normalisation analytically using the convolution integral above. In our case, it is acceptable to simply discard the normalisation as the goal is to produce a null significance map for the purpose of calibrating the look-elsewhere effect, and such significance maps are typically normalised to have unity variance. A single sample from the Gaussian random field described by Equation 5.10 is shown in Figure 5.3. The parameter space is divided into 60 bins in each dimension when generating this sample.

We can now compare samples generated using a traditional toy MC and Gaussian field samples. This is shown in Figure 5.4. The Gaussian random fields are sampled both using the spectral method described in subsection 5.2.2 and the naive method, where a large covariance matrix describing the covariance between every pair of points is directly sampled as a multivariate Gaussian.

As expected, the excursion probability obtained from toy MC samples agree with those obtained by sampling Gaussian random fields. This demonstrates how Gaussian random fields can be sampled to produce large numbers of null significance map samples without a full toy MC. Finally, we can test the use of Equation 5.7 to fit the excursion probability. As the error term in Equation 5.7 is exponentially suppressed at small excursion probabilities, the fit only uses data points from after $u^2 = 10$, where the excursion probability is approximately 0.1; this is shown in Figure 5.5.
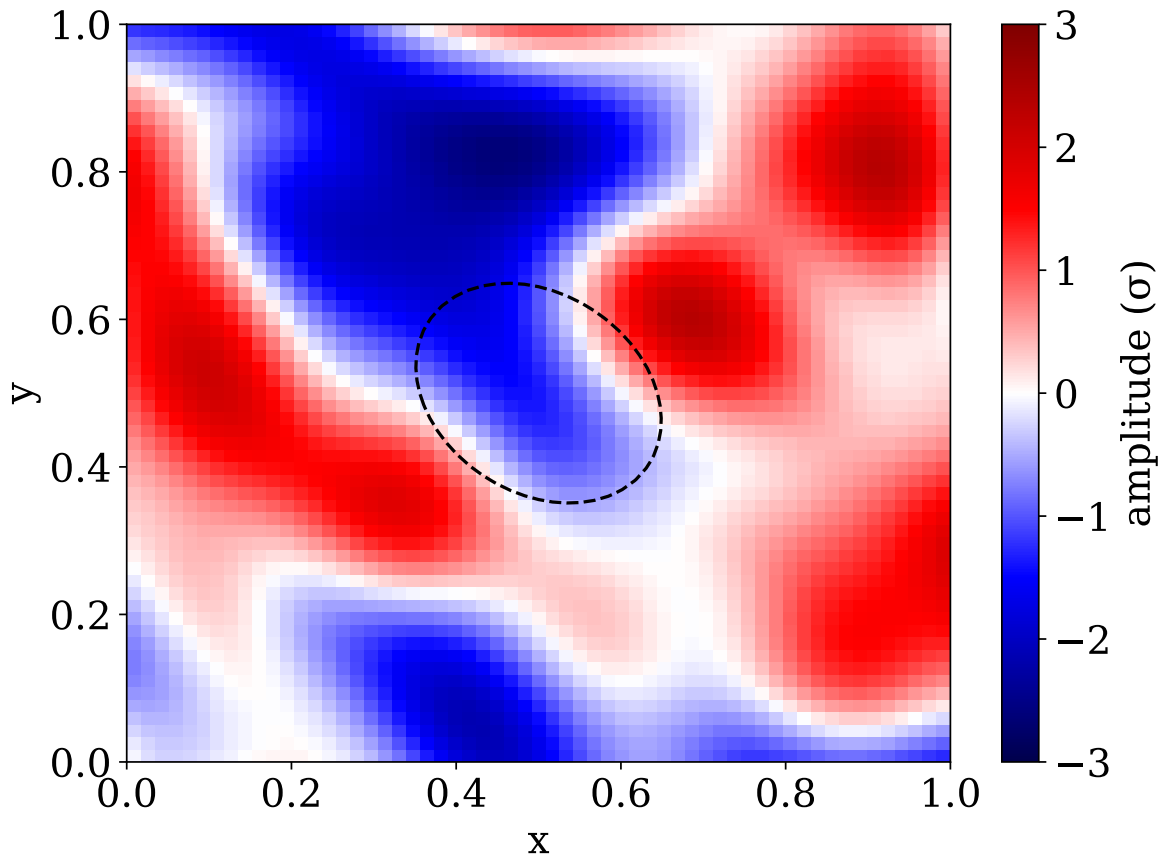
**Figure 5.3.** Example of a single null random sample. The FWHM of the covariance function is overlaid as a black dashed ellipse for comparison.
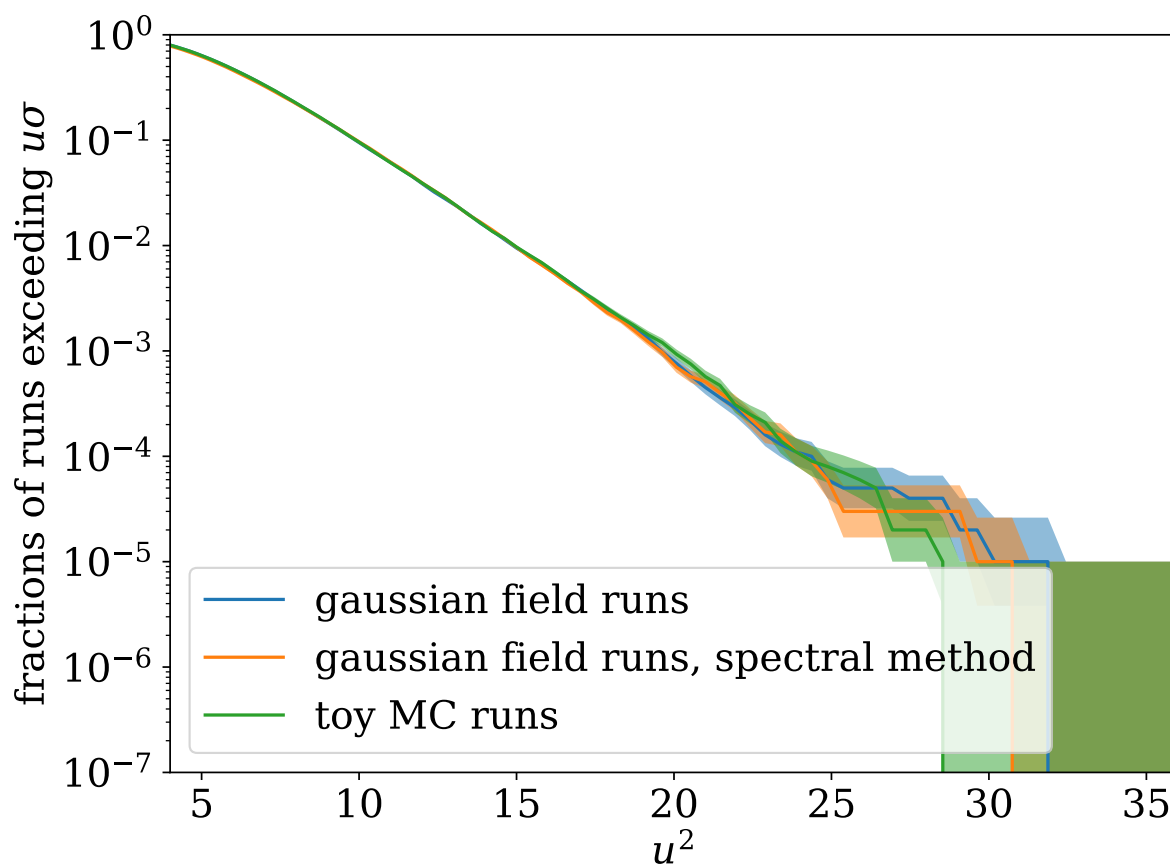
**Figure 5.4.** The fraction of $10^5$ null random samples showing false positives as a function of the significance threshold in units of $\sigma^2$. We can see that the different methods to generate random fields work produce global p-values that are in agreement.
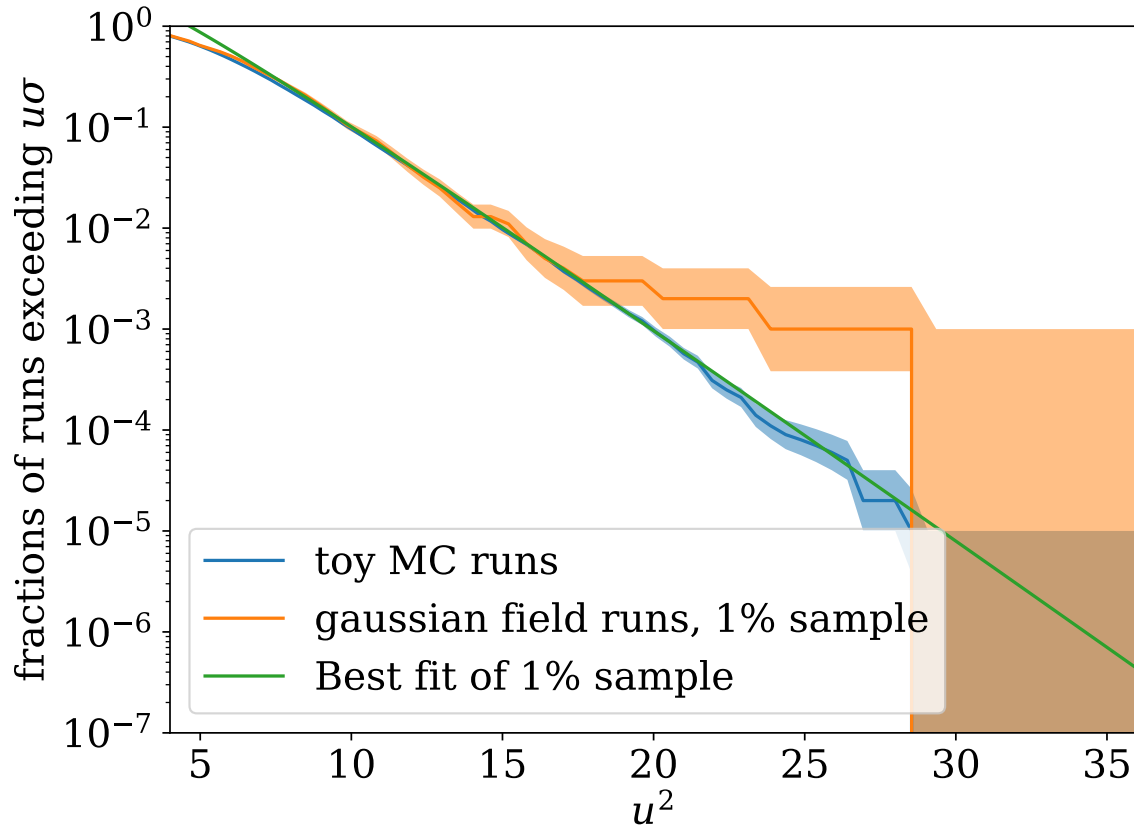
**Figure 5.5.** The fraction of null random samples showing false positives as a function of the significance threshold in units of $\sigma^2$. A fit using Equation 5.7 is shown here, and we can see that a fit with only $10^3$ samples agrees well with the exceedance probability derived from $10^5$ toy MC samples.

Even though only $10^3$ samples are used to fit the excursion probability, the fit matches the excursion probability expected from the toy MC samples. This demonstrates that fitting a limited set of samples using Equation 5.7 does indeed allow one to estimate the look-elsewhere effect correction with greatly reduced computational expense. These results are summarised in Table 5.1, where it can be seen that the various methods all agree within expected uncertainties.

**Table 5.1.** Global p-values at $4\sigma$ and $5\sigma$ local significance for the 2D toy problem. It can be seen that the p-values are consistent within stated binomial errors, and the best fit value produced using a 1% sample size reproduces the simulated values well.

| Method | $p_{4\sigma}$ | $p_{5\sigma}$ |
|---|---|---|
| Toy MC | $\left(6.27^{+0.25}_{-0.24}\right) \times 10^{-3}$ | $\left(8.0^{+3.4}_{-2.4}\right) \times 10^{-5}$ |
| Gaussian random field | $\left(6.17^{+0.25}_{-0.24}\right) \times 10^{-3}$ | $\left(6.0^{+3.0}_{-2.0}\right) \times 10^{-5}$ |
| Gaussian random field, spectral method | $\left(5.98^{+0.25}_{-0.24}\right) \times 10^{-3}$ | $\left(5.0^{+2.8}_{-1.8}\right) \times 10^{-5}$ |
| Best fit | $6.36 \times 10^{-3}$ | $8.8 \times 10^{-5}$ |

## 5.4 Demonstration with a 1D Template Matching Problem

We showed in section 5.3 that in the case of a Gaussian search kernel and uniformly distributed underlying random variables, the covariance function can be easily computed. Indeed, while the derivation focused on Gaussian kernels, the result should hold in general for kernels that are closed under convolution, such as kernels that represent stable distributions [160].

In many cases, however, the covariance function might be easier to compute numerically. To demonstrate such an example, in this section we consider a 1-dimensional search with a non-Gaussian kernel, for an excess in time-series data due to a particle interacting via a long-range force passing by an accelerometer. This toy problem is inspired by the Windchime project [41], where the direct detection of dark matter particles with masses of around the Planck mass will be attempted. While technically challenging, it has been suggested that this might be possible with large accelerometer arrays [23]. In the case of a dark matter particle passing by an accelerometer, the force as a function of time is given by Equation 5.11, where

$G$ is the gravitational constant, $m_\chi$ is the mass of a dark matter particle, $m_s$ is the test mass of the sensor, $b$ is the impact parameter of a dark matter track, and $v$ is the velocity of the dark matter track [23].

$$F(t) = \frac{Gm_\chi m_s b}{(b^2 + v^2 t^2)^{3/2}} \tag{5.11}$$

For template matching purposes, a normalised template with the same shape as Equation 5.11 can be used. This is shown in equation Equation 5.12.

$$f(t) = \frac{vb^2}{2 (b^2 + v^2 t^2)^{3/2}} \tag{5.12}$$

In this demonstration, values of $b = 3\,\text{mm}$ and $v = 3 \times 10^5\,\text{m/s}$ are used, and the sampling rate is $10^9\,\text{Hz}$. With this information, we can generate the template for template matching, and then compute the covariance function using Equation 5.3. As this system is also described by a stationary random field, this is done by simply computing the autocorrelation of the template. These are shown together with MC data samples in Figure 5.6. As in section 5.3, the global p-values at $4\sigma$ and $5\sigma$ local significance are computed using $10^5$ signal-free samples each using a toy MC, direct sampling of the Gaussian random field using the covariance function, sampling of the Gaussian random field in frequency space, and a best-fit with $10^3$ samples using Equation 5.7. The best-fit only uses data points after $u^2 = 10$, where the excursion probability is approximately 0.1. These results are shown in Table 5.2.

**Table 5.2.** Global p-values at $4\sigma$ and $5\sigma$ local significance for the 1D template matching problem. It can be seen that the p-values are consistent within stated binomial errors, and the best fit value produced using a 1% sample size reproduces the simulated values well.

| Method | $p_{4\sigma}$ | $p_{5\sigma}$ |
|---|---|---|
| Toy MC | $\left(5.82^{+0.25}_{-0.24}\right) \times 10^{-3}$ | $\left(3.0^{+2.3}_{-1.3}\right) \times 10^{-5}$ |
| Gaussian random field | $\left(6.13^{+0.25}_{-0.24}\right) \times 10^{-3}$ | $\left(10^{+4}_{-3}\right) \times 10^{-5}$ |
| Gaussian random field, spectral method | $\left(6.29^{+0.25}_{-0.25}\right) \times 10^{-3}$ | $\left(10^{+4}_{-3}\right) \times 10^{-5}$ |
| Best fit | $5.42 \times 10^{-3}$ | $4.9 \times 10^{-5}$ |

As we expect, the different values agree to the computed uncertainty, demonstrating how the methods outlined in this paper can be used to estimate the look-elsewhere effect. While
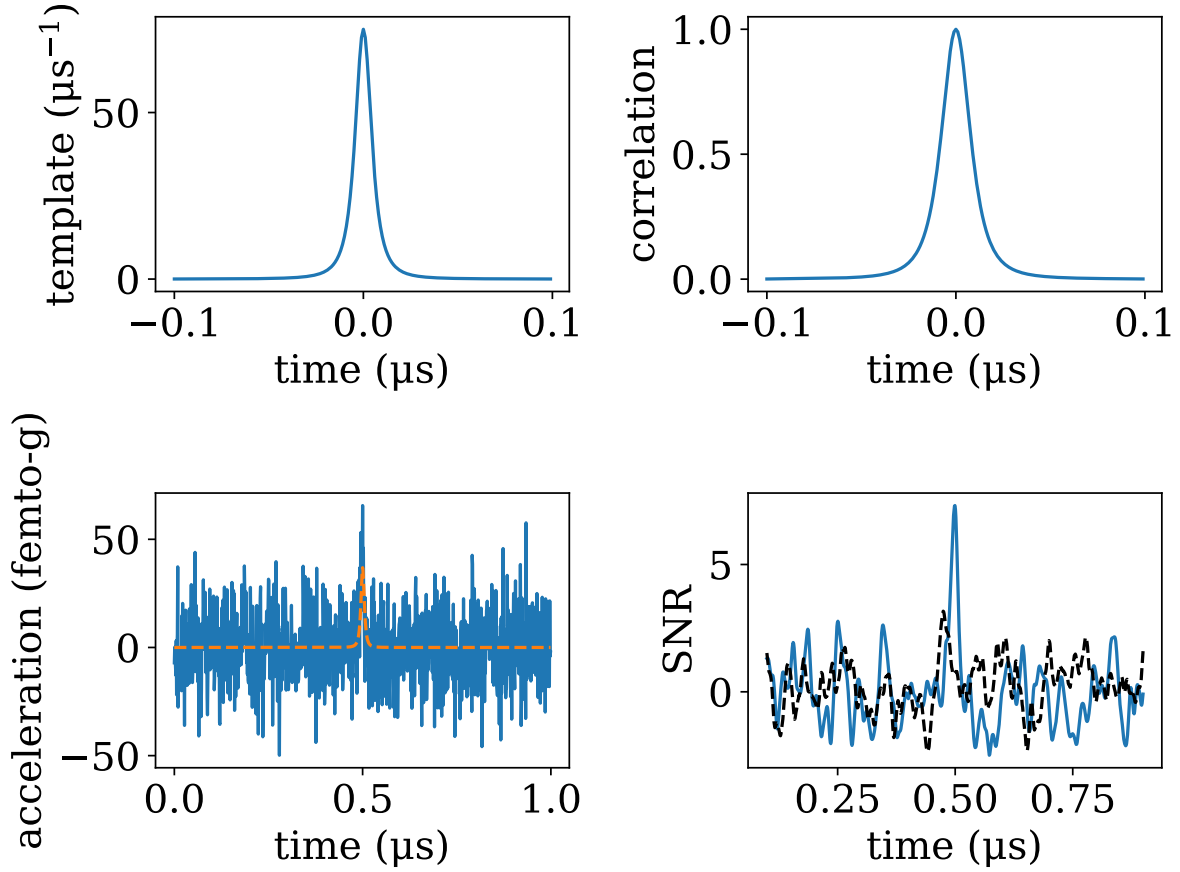
**Figure 5.6.** Top left: The template function of the 1D toy problem. Top right: The correlation function derived as the autocorrelation of the template. Bottom left: One random sample containing a true signal, with the signal truth expectation shown in dashed orange. Bottom right: Two significance maps generated using the toy MC procedure. The blue line contains a true signal, whereas the black dashed line does not.

the example here uses a template that is relevant to the Windchime project, this procedure can be used in general to calibrate the look-elsewhere effect correction for problems involving template matching or matched filtering of time-series data, including sonar [161] and fast radio burst detection [162]. It should be noted that for cases involving multiple templates, correlations between templates would need to be computed as well to avoid underestimation of the significance of a signal.

## 5.5   Application to Windchime

These methods can now be applied to estimate the look-elsewhere effect correction needed for a dark matter direct detection experiment based on the Windchime concept [41]. In this section, we consider the detection of dark matter interacting via a long range force using a $0.6\,\mathrm{m}$ array of $4^3$ accelerometers, with a sampling rate of $10^7\,\mathrm{Hz}$.

The force on a single sensor is given in Equation 5.11. However, for a particle passing through a sensor array, the impact parameter $b$ would be different for each sensor, and additionally, the time of closest approach differs between sensors. Thus, instead of using the template for a single sensor, a template for the entire array is considered. As each template represents a track, we have to consider the parameterisation of a track through the sensor array. This is accomplished using a bounding sphere that is larger than the accelerometer array, so that each track through the array intersects the bounding sphere twice and hence can be parameterised by two points on the bounding sphere. Any given template can then be parameterised by 6 parameters: velocity ($v$), entry time, the spherical coordinates of the entry point $(\cos(\theta_0), \phi_0)$, and the spherical coordinates of the exit point $(\cos(\theta_1), \phi_1)$. The cosine of the $\theta$ angles is used as evenly-spaced bins in $\cos(\theta)$ represent equal-sized areas on a sphere. Here, we consider a bounding sphere with a diameter of $1\,\mathrm{m}$, so that it encloses the entire array.

For each set of the 6 parameters, a template is generated by considering the force on each sensor over a series of timesteps. At every timestep, the distance between the particle and every sensor is calculated, and the template for each sensor is computed using the inverse-square law. The equation for the template at the $i^{\text{th}}$ timestep and the $j^{\text{th}}$ sensor is thus simply:

$$\mathbf{f}_{ij} = \frac{\mathbf{r}_{ij}}{r_{ij}^3} \tag{5.13}$$

After the computation of the entire template over a set of timesteps and all sensors, the template is divided by its sum to normalise it to unity. Finally, the covariance between two sets of parameters can be computed by summing across all sensors and timesteps using Equation 5.3. This allows for the covariance function to be mapped out between one template and all surrounding templates. Some 2D slices of the covariance function is shown in Figure 5.7.

It can be seen from Figure 5.7 that the Gaussian random field representing this problem is not stationary. This is because in the case of a stationary field, the covariance function only depends on the displacement between points, as described in Equation 5.5. This implies that $K(\mathbf{x}, \mathbf{x} - \mathbf{d}) = K(\mathbf{x} - \mathbf{d}, \mathbf{x}) = K(\mathbf{x}, \mathbf{x} + \mathbf{d})$. Thus, for a stationary process, $K_s(\mathbf{d}) = K_s(-\mathbf{d})$ and the covariance function should be symmetric. Unfortunately, this means that Wiener-Khinchin theorem does not apply, and spectral sampling of this covariance is not possible. To get an estimate the look-elsewhere correction, we can approximate the covariance function using a symmetric functional form. Here, we use a Gaussian kernel to approximate the covariance function. Similar 2D slices of the approximate covariance function is shown in Figure 5.8. A random sample from the Gaussian random field represented by Figure 5.8, sampled using the spectral method, is shown in Figure 5.9. The excursion probability can then be fit to samples such as Figure 5.9. The excursion probability estimated with 2000 such samples is shown in Figure 5.10.
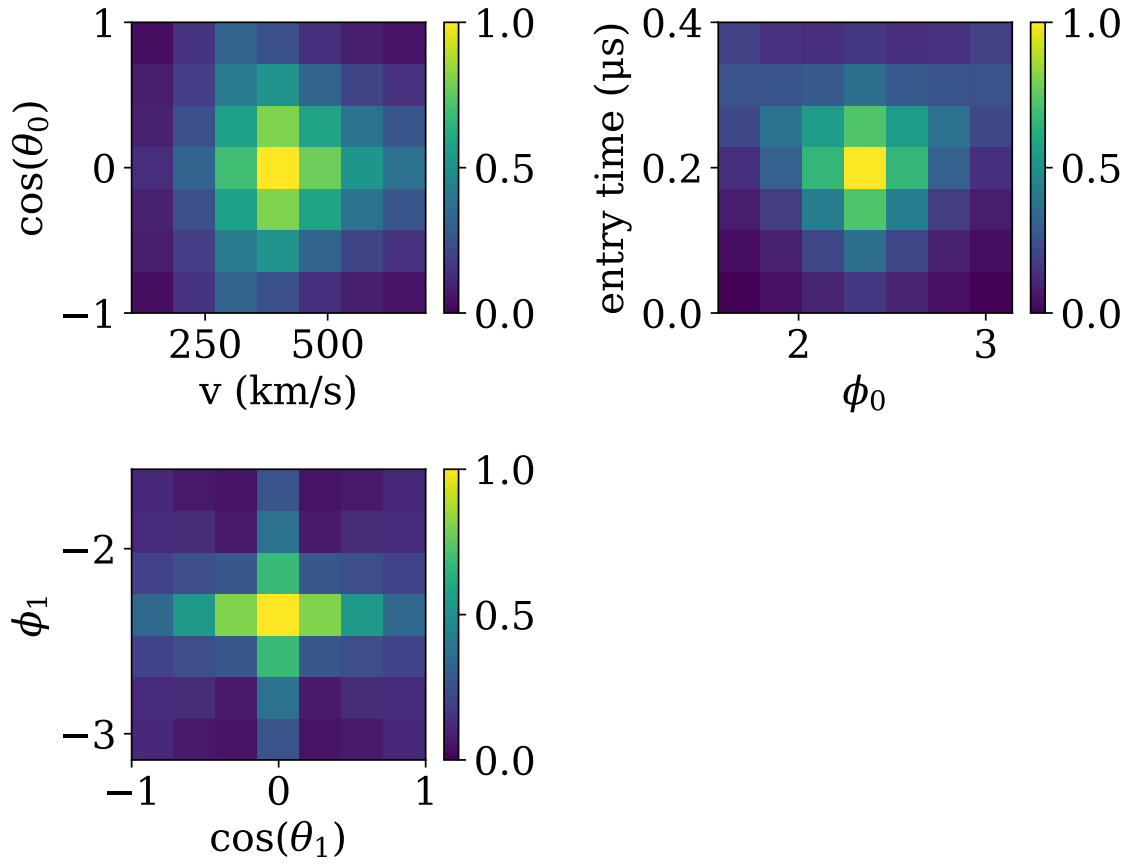
**Figure 5.7.** 2D slices of the 6D covariance function computed using accelerometer array templates.
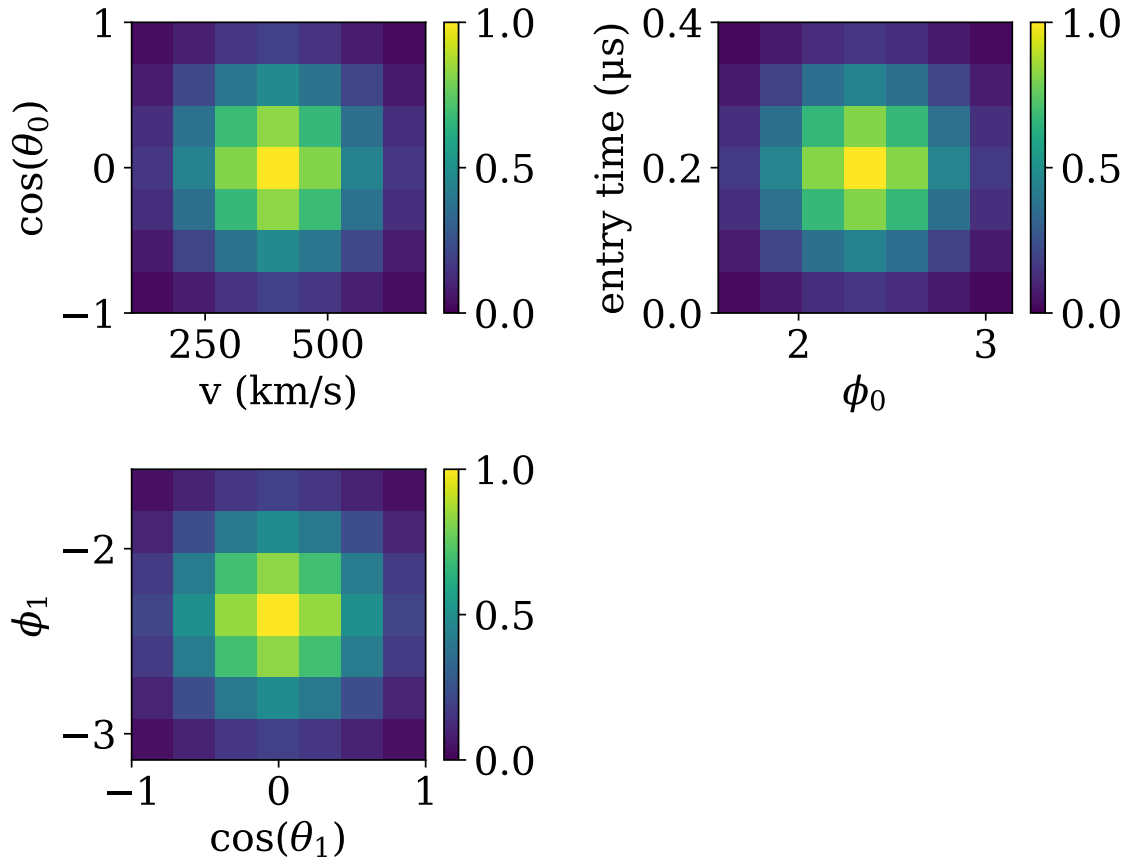
**Figure 5.8.** Gaussian kernel approximation of the slices of the 6D correlation function shown in Fig. 5.7
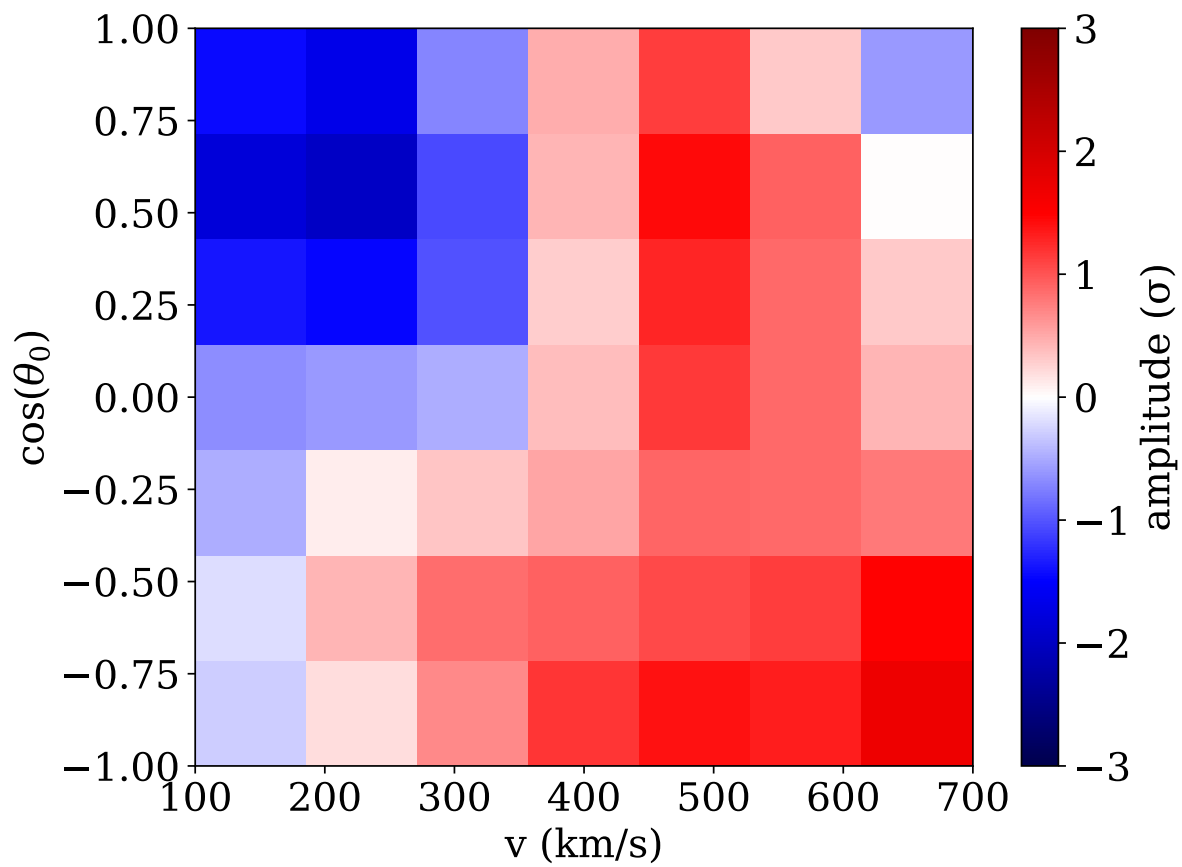
**Figure 5.9.** 2D slice of one null sample, generated using the covariance function shown in Fig. 5.8.
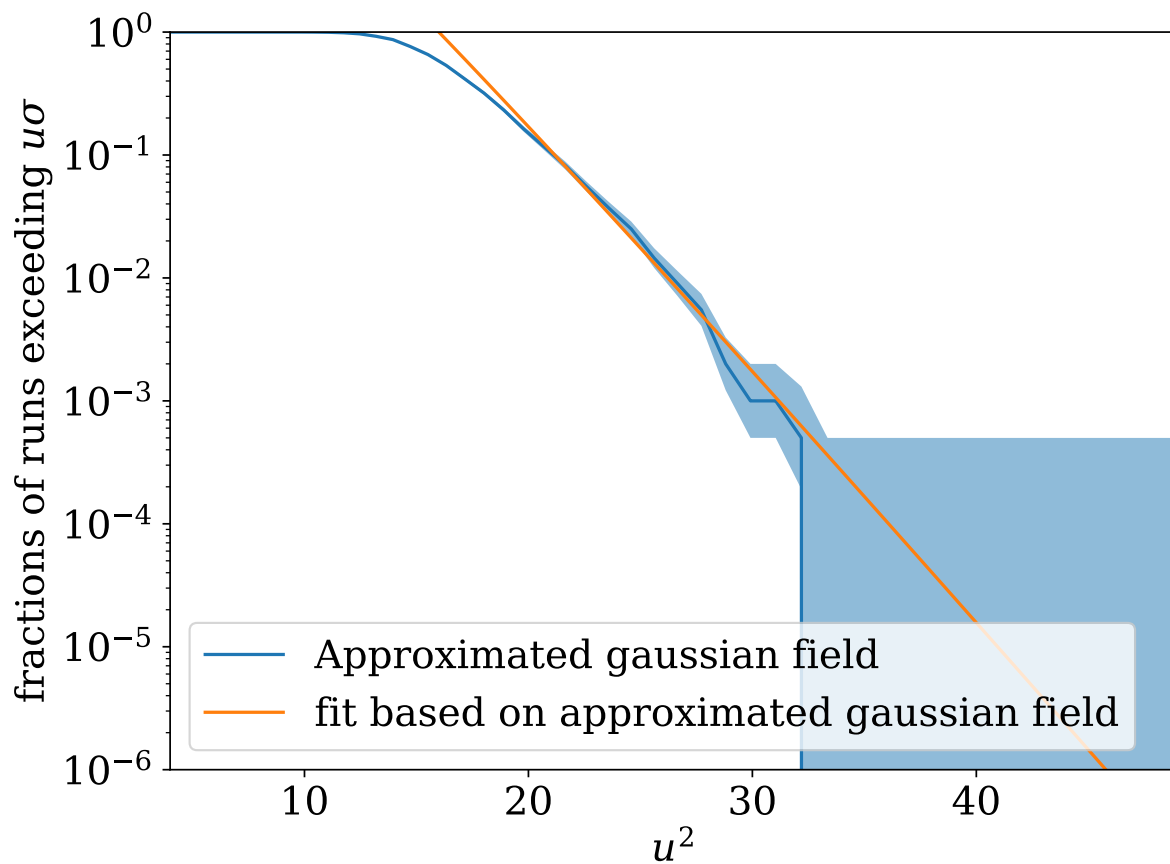
**Figure 5.10.** The fraction of null random samples showing false positives as a function of the significance threshold in units of $\sigma^2$, with a fit using Equation 5.7. 2000 samples generated using the spectral method are shown here.

We can now compute the trial factor using the fit in Figure 5.10. First, we need to compute the SNR threshold needed for a search with confidence level $1 - \alpha$ over time $t$. Here, we use $\alpha = 0.0027$, corresponding to a significance level of $3\sigma$. The SNR threshold is then found by solving Equation 5.14 for $u$:

$$\Psi(u)\frac{V'}{V}\frac{T'}{T} - \alpha = 0 \tag{5.14}$$

where $\Psi(u)$ is the fitted excursion probability function, $\frac{V'}{V}$ corresponds to the fraction of parameter space covered by the sampled Gaussian field, and $\frac{T'}{T}$ corresponds to the search time covered by the random field divided by the desired search time. This procedure tells us we need an SNR threshold of 8 for a 1 s search time and 10 for a 1 yr search time. The trial factor, $N_{\text{trials}}$, is then simply given by:

$$N_{trials} = \frac{\alpha}{\Phi(u)} \tag{5.15}$$

This results in estimated trial factors of $\sim 10^{12}$ for a 1 s search, and $\sim 10^{20}$ for a 1 yr search. We can see that due to the high dimensional search space, there is an extremely high trial factor. Thus, thresholds much higher than the $5\sigma$ level customary in particle physics [2, 163, 164] are needed for a rare event search with an accelerometer array.

## 5.6 Summary and Conclusions

In this paper, we describe and demonstrate the use of Gaussian random fields in the estimation of the look-elsewhere effect. The presented methods can be used to greatly reduce the computational requirements for the estimation of the look-elsewhere effect. This is particularly useful for high-dimensional and otherwise computationally complex problems, and can also be helpful for sensitivity projections of future experiments where the computational infrastructure needed for the data-analysis of such an experiment does not yet exist.

Gaussian random fields can be used to model a large set of statistical problems commonly encountered in physics. Because the Gaussian distribution is stable, for a problem involving underlying Gaussian random variables, template matching or matched filtering would result

in significance maps that can be described by Gaussian random fields. This is also true if likelihood ratio tests are used instead of template matching. An example of such a system where the underlying random variables are random could be a pixel array with Gaussian noise [157]. In cases where the underlying random variables might be non-Gaussian, the resulting null significance maps might still be asymptotically Gaussian or $\chi^2$, due to either central limit theorems in the case of template matching and matched filtering, or to Wilk's theorem in the case of likelihood ratio tests. For problems that can be modelled using Gaussian random fields, it is often possible to directly compute the covariance function, such as from the templates used for template matching.

When it has been ascertained that a given significance map can be modelled by a Gaussian random field, two techniques that can be used to reduce the computational cost of estimating the look-elsewhere effect correction for local significance are introduced in this paper. First, various methods exist for the efficient sampling of Gaussian random fields, such as the spectral method where samples are generated in frequency space. A review of such methods can be found in [155]. This can allow for Gaussian random fields to be sampled more efficiently than the directly sampling from a large covariance matrix. Second, an analytic approximation of excursion probability, from [152], can be used to fit a small set of null significance map samples. These methods can be combined to further reduce the computational cost of estimating the look-elsewhere effect correction at low p-values.

The above techniques are then demonstrated on 2D and 1D toy problems. The 2D toy problem represents searches in a 2D parameter space, such as searches for dark matter using pixel detectors [54, 157] and searches for astronomical transients [158, 159]. A Gaussian kernel is used for the template, thus allowing for direct analytic computation of the covariance function. The 1D toy problem represents searches in a 1D parameter space, such as searches for dark matter using accelerometers [41], sonar [161], and fast radio burst detection [162]. Using $10^5$ samples generated with each method, we show that the look-elsewhere effect corrections derived using toy MC significance maps agree with those sampled from Gaussian random fields, both when the Gaussian random field covariance functions are directly sampled and when the Gaussian random fields are sampled using the spectral method. Finally, a much smaller sample of $10^3$ null significance maps is used to fit the excursion probability.

This analytic fit also agrees with the other approaches, allowing for a greater reduction in computational cost.

Finally, these techniques are applied to a $4^3$ accelerometer array based on the Windchime concept. Tracks through such an array are parameterised by 6 parameters: velocity ($v$), entry time, the spherical coordinates of the entry point $(\cos(\theta_0), \phi_0)$, and the spherical coordinates of the exit point $(\cos(\theta_1), \phi_1)$. The Gaussian random field representing null significance maps from this problem is not stationary, hence the spectral method for sampling this array cannot be directly used. Thus, a Gaussian kernel is used to approximate the covariance function. The spectral method is then used to generate 2000 null significance map samples, which are used to fit the excursion probability. We find that when we require a global significance of $3\sigma$ the estimated trial factor for such an accelerometer array is $10^{12}$ for a 1 s search, and $10^{20}$ for a 1 yr search.

# 6. CONCLUSION

*"Writing is hard work."* - Isaac Asimov [165]

Over the course of my PhD, as a member of the XENON and Windchime collaborations, I have worked on improving and broadening the search for dark matter, with a focus on computational techniques and algorithms. This has culminated in my work, as detailed in the chapters of this thesis, on the reduction of radon chain backgrounds in XENON, the calibration of XENONnT using a $^{88}$Y photo-neutron source, analysis and sensitivity projections for the Windchime project, and the use of Gaussian random fields to estimate corrections to statistical significance due to the look-elsewhere effect.

To reduce radon chain backgrounds in XENON, I have designed an algorithm to veto these backgrounds, and demonstrated the use of this algorithm using XENON1T data. The algorithm performs tagging of the $^{214}$Pb background, which is part of the $^{222}$Rn decay chain. This was done by first constructing the convection velocity field in the detector. The constructed velocity field was then used to propagate velocity fields out from candidate $^{214}$Pb events to search for events corresponding to the decays preceding and succeeding the decay of $^{214}$Pb from the same decay chain–the candidate event could then be vetoed if there was a match. It was shown that this works and produces a modest background reduction in XENON1T, with the potential for significantly higher performance in XENONnT and future detectors. Variations of this method can also be used to veto the cosmogenic $^{137}$Xe background, which is important for the search for the search for neutrinoless double-beta decay in xenon detectors.

I have also designed and constructed a $^{88}$Y/Be photo-neutron source for the calibration of the XENONnT detector. The source was designed to maximise ratio of neutron events to overall rate in the PC as much as possible given the physical constraints of the I-Belt system, and has been shown to work, producing a population of neutron events in the expected energy range. This will be used in the calibration of the XENONnT detector. I expect this measurement to strongly constrain our detector response to nuclear recoils below 5 keV and

hence to help enable a measurement of $^8$B solar neutrinos via CE$\nu$NS. In addition, such a calibration of the detector response close to the threshold will also aid in the search for WIMP dark matter.

As a founding member of Windchime, I then laid down foundational work for the Windchime project to enable sensitivity projections and searches for dark matter. This includes methods to compute sensitivity projections for the Windchime project, frequentist and Bayesian approaches for track-finding below the single-sensor noise floor, and the construction of a likelihood ratio for the search of ultralight dark matter. I show that the methods developed do work on simulated data and various sensor array configurations, and can be used as a basis for a future dark matter search programme.

Finally, in the course of developing methods for the Windchime project, I also worked on the use of Gaussian random fields to estimate corrections to statistical significance due to the look-elsewhere effect. This can be used to greatly reduce the computational requirements for the estimation of the look-elsewhere effect, and will be used to determine the appropriate thresholds for dark matter searches with Windchime that can maintain appropriately low false alarm rates.

I believe my work, as detailed in this thesis, represents a step forward in the search for dark matter. I am excited to see the impact my work has on the of the field in the future, and to continue pushing the boundaries of our understanding of the universe!

# REFERENCES

[1]     A. C. Clarke, *Profiles of the future*, 3rd ed. Oxford, England: Weidenfeld & Nicolson, Nov. 1999.

[2]     R. L. Workman, "Review of Particle Physics," *PTEP*, vol. 2022, p. 083C01, 2022. DOI: 10.1093/ptep/ptac097.

[3]     J. Billard *et al.*, "Direct detection of dark matter–APPEC committee report," *Rept. Prog. Phys.*, vol. 85, no. 5, p. 056 201, 2022. DOI: 10.1088/1361-6633/ac5754. arXiv: 2104.07634 [hep-ex].

[4]     N. Aghanim *et al.*, "Planck 2018 results. VI. Cosmological parameters," *Astron. Astrophys.*, vol. 641, A6, 2020, [Erratum: Astron.Astrophys. 652, C4 (2021)]. DOI: 10.1051/0004-6361/201833910. arXiv: 1807.06209 [astro-ph.CO].

[5]     Y. Sofue, "Rotation and Mass in the Milky Way and Spiral Galaxies," *Publications of the Astronomical Society of Japan*, vol. 69, no. 1, R1, Feb. 2017, ISSN: 0004-6264, 2053-051X. DOI: 10.1093/pasj/psw103. arXiv: 1608.08350.

[6]     L. Anderson *et al.*, "The clustering of galaxies in the SDSS-III Baryon Oscillation Spectroscopic Survey: Baryon Acoustic Oscillations in the Data Release 9 Spectroscopic Galaxy Sample," *Mon. Not. Roy. Astron. Soc.*, vol. 427, no. 4, pp. 3435–3467, 2013. DOI: 10.1111/j.1365-2966.2012.22066.x. arXiv: 1203.6594 [astro-ph.CO].

[7]     B. D. Fields, K. A. Olive, T.-H. Yeh, and C. Young, "Big-Bang Nucleosynthesis after Planck," *JCAP*, vol. 03, p. 010, 2020, [Erratum: JCAP 11, E02 (2020)]. DOI: 10.1088/1475-7516/2020/03/010. arXiv: 1912.01132 [astro-ph.CO].

[8]     E. Gawiser and J. Silk, "The Cosmic microwave background radiation," *Phys. Rept.*, vol. 333, pp. 245–267, 2000. DOI: 10.1016/S0370-1573(00)00025-9. arXiv: astro-ph/0002044.

[9]     N. Aghanim *et al.*, "Planck 2018 results. I. Overview and the cosmological legacy of Planck," *Astron. Astrophys.*, vol. 641, A1, 2020. DOI: 10.1051/0004-6361/201833880. arXiv: 1807.06205 [astro-ph.CO].

[10]    T. M. C. Abbott *et al.*, "Dark Energy Survey year 1 results: Cosmological constraints from galaxy clustering and weak lensing," *Phys. Rev. D*, vol. 98, no. 4, p. 043 526, 2018. DOI: 10.1103/PhysRevD.98.043526. arXiv: 1708.01530 [astro-ph.CO].

[11]    "Apod: 2017 january 15 - the matter of the bullet cluster." (Jan. 2017), [Online].
        Available: https://apod.nasa.gov/apod/ap170115.html.

[12]    M. Markevitch, "Chandra observation of the most interesting cluster in the universe,"
        *ESA Spec. Publ.*, vol. 604, p. 723, 2006. arXiv: astro-ph/0511345.

[13]    D. Clowe *et al.*, "A direct empirical proof of the existence of dark matter," *Astrophys.
        J. Lett.*, vol. 648, pp. L109–L113, 2006. DOI: 10.1086/508162. arXiv: astro-ph/0608407.

[14]    D. H. Perkins, *Particle astrophysics, second edition* (Oxford Master Series in Physics),
        en, 2nd ed. London, England: Oxford University Press, Oct. 2008.

[15]    K. Freese, "Review of Observational Evidence for Dark Matter in the Universe and in
        upcoming searches for Dark Stars," *EAS Publ. Ser.*, vol. 36, E. Pécontal, T. Buchert,
        P. Di Stefano, and Y. Copin, Eds., pp. 113–126, 2009. DOI: 10.1051/eas/0936016.
        arXiv: 0812.4005 [astro-ph].

[16]    . Chrobáková, M. López-Corredoira, F. Sylos Labini, H. .-. Wang, and R. Nagy,
        "Gaia-DR2 extended kinematical maps. III. Rotation curves analysis, dark matter,
        and MOND tests," *Astronomy & Astrophysics*, vol. 642, A95, A95, Oct. 2020. DOI:
        10.1051/0004-6361/202038736. arXiv: 2007.14825 [astro-ph.GA].

[17]    C. Grupen, *Astroparticle physics*, en. Cham, Switzerland: Springer Nature, Jan. 2020.

[18]    Y. Yoon, C. Park, H. Chung, and K. Zhang, "Rotation curves of galaxies and their
        dependence on morphology and stellar mass," *The Astrophysical Journal*, vol. 922, no. 2,
        p. 249, Dec. 2021. DOI: 10.3847/1538-4357/ac2302. arXiv: 2110.06033 [astro-ph.GA].

[19]    E. Corbelli and P. Salucci, "The Extended Rotation Curve and the Dark Matter Halo
        of M33," *Mon. Not. Roy. Astron. Soc.*, vol. 311, pp. 441–447, 2000. DOI: 10.1046/j.1365-
        8711.2000.03075.x. arXiv: astro-ph/9909252.

[20]    M. H. Chan, S. Desai, and A. Del Popolo, "There is no universal acceleration scale
        in galaxies," *Publ. Astron. Soc. Jap.*, vol. 74, no. 6, pp. 1441-1452–1452, 2022. DOI:
        10.1093/pasj/psac083. arXiv: 2205.07515 [astro-ph.GA].

[21]    K. Pardo and D. N. Spergel, "What is the price of abandoning dark matter? Cos-
        mological constraints on alternative gravity theories," *Phys. Rev. Lett.*, vol. 125,
        no. 21, p. 211 101, 2020. DOI: 10.1103/PhysRevLett.125.211101. arXiv: 2007.00555
        [astro-ph.CO].

[22]    L. Roszkowski, E. M. Sessolo, and S. Trojanowski, "WIMP dark matter candidates and searchescurrent status and future prospects," *Rept. Prog. Phys.*, vol. 81, no. 6, p. 066 201, 2018. DOI: 10.1088/1361-6633/aab913. arXiv: 1707.06277 [hep-ph].

[23]    D. Carney, S. Ghosh, G. Krnjaic, and J. M. Taylor, "Proposal for gravitational direct detection of dark matter," *Phys. Rev. D*, vol. 102, no. 7, p. 072 003, 2020. DOI: 10.1103/PhysRevD.102.072003. arXiv: 1903.00492 [hep-ph].

[24]    J. Bramante, B. Broerman, R. F. Lang, and N. Raj, "Saturated Overburden Scattering and the Multiscatter Frontier: Discovering Dark Matter at the Planck Mass and Beyond," *Phys. Rev. D*, vol. 98, no. 8, p. 083 516, 2018. DOI: 10.1103/PhysRevD.98.083516. arXiv: 1803.08044 [hep-ph].

[25]    D. Carney *et al.*, "Snowmass2021 Cosmic Frontier White Paper: Ultraheavy particle dark matter," Mar. 2022. arXiv: 2203.06508 [hep-ph].

[26]    C. Blanco, B. Elshimy, R. F. Lang, and R. Orlando, "Models of ultraheavy dark matter visible to macroscopic mechanical sensing arrays," *Phys. Rev. D*, vol. 105, no. 11, p. 115 031, 2022. DOI: 10.1103/PhysRevD.105.115031. arXiv: 2112.14784 [hep-ph].

[27]    E. Aprile *et al.*, "The XENON1T Dark Matter Experiment," *Eur. Phys. J. C*, vol. 77, no. 12, p. 881, 2017. DOI: 10.1140/epjc/s10052-017-5326-3. arXiv: 1708.07051 [astro-ph.IM].

[28]    J. Aalbers *et al.*, "First Dark Matter Search Results from the LUX-ZEPLIN (LZ) Experiment," Jul. 2022. arXiv: 2207.03764 [hep-ex].

[29]    E. Aprile *et al.*, "Dark Matter Search Results from a One Ton-Year Exposure of XENON1T," *Phys. Rev. Lett.*, vol. 121, no. 11, p. 111 302, 2018. DOI: 10.1103/PhysRevLett.121.111302. arXiv: 1805.12562 [astro-ph.CO].

[30]    Y. Meng *et al.*, "Dark Matter Search Results from the PandaX-4T Commissioning Run," *Phys. Rev. Lett.*, vol. 127, no. 26, p. 261 802, 2021. DOI: 10.1103/PhysRevLett.127.261802. arXiv: 2107.13438 [hep-ex].

[31]    E. Aprile *et al.*, "Double-Weak Decays of $^{124}$Xe and $^{136}$Xe in the XENON1T and XENONnT Experiments," *Phys. Rev. C*, vol. 106, no. 2, p. 024 328, 2022. DOI: 10.1103/PhysRevC.106.024328. arXiv: 2205.04158 [hep-ex].

[32]    G. Anton *et al.*, "Search for Neutrinoless Double-$\beta$ Decay with the Complete EXO-200 Dataset," *Phys. Rev. Lett.*, vol. 123, no. 16, p. 161 802, 2019. DOI: 10.1103/PhysRevLett.123.161802. arXiv: 1906.02723 [hep-ex].

[33]    D. S. Akerib *et al.*, "Projected sensitivity of the LUX-ZEPLIN experiment to the two-neutrino and neutrinoless double $\beta$ decays of $^{134}$Xe," *Phys. Rev. C*, vol. 104, no. 6, p. 065 501, 2021. DOI: 10.1103/PhysRevC.104.065501. arXiv: 2104.13374 [physics.ins-det].

[34]    E. Aprile *et al.*, "Observation of two-neutrino double electron capture in $^{124}$Xe with XENON1T," *Nature*, vol. 568, no. 7753, pp. 532–535, 2019. DOI: 10.1038/s41586-019-1124-4. arXiv: 1904.11002 [nucl-ex].

[35]    E. Aprile *et al.*, "Excess electronic recoil events in XENON1T," *Phys. Rev. D*, vol. 102, no. 7, p. 072 004, 2020. DOI: 10.1103/PhysRevD.102.072004. arXiv: 2006.09721 [hep-ex].

[36]    E. Aprile *et al.*, "Search for New Physics in Electronic Recoil Data from XENONnT," *Phys. Rev. Lett.*, vol. 129, no. 16, p. 161 805, 2022. DOI: 10.1103/PhysRevLett.129.161805. arXiv: 2207.11330 [hep-ex].

[37]    J. Aalbers *et al.*, "A next-generation liquid xenon observatory for dark matter and neutrino physics," *J. Phys. G*, vol. 50, no. 1, p. 013 001, 2023. DOI: 10.1088/1361-6471/ac841a. arXiv: 2203.02309 [physics.ins-det].

[38]    L. Althüser, "Light collection efficiency simulations of the xenon1t experiment and comparison to data," Master's thesis, WWU Münster, Nov. 2017.

[39]    E. Aprile *et al.*, "Projected WIMP sensitivity of the XENONnT dark matter experiment," *JCAP*, vol. 11, p. 031, 2020. DOI: 10.1088/1475-7516/2020/11/031. arXiv: 2007.08796 [physics.ins-det].

[40]    E. Aprile and T. Doke, "Liquid Xenon Detectors for Particle Physics and Astrophysics," *Rev. Mod. Phys.*, vol. 82, pp. 2053–2097, 2010. DOI: 10.1103/RevModPhys.82.2053. arXiv: 0910.4956 [physics.ins-det].

[41]    A. Attanasio *et al.*, "Snowmass 2021 White Paper: The Windchime Project," in *2022 Snowmass Summer Study*, Mar. 2022. arXiv: 2203.07242 [hep-ex].

[42]    M. B. Seiger, "THE EFFECTS OF CHROMOSOME SUBSTITUTION ON MALE BODY WEIGHT OF DROSOPHILA MELANOGASTER," *Genetics*, vol. 53, no. 2, pp. 237–248, Feb. 1966, ISSN: 1943-2631. DOI: 10.1093/genetics/53.2.237. eprint: https://academic.oup.com/genetics/article-pdf/53/2/237/34373028/genetics0237.pdf. [Online]. Available: https://doi.org/10.1093/genetics/53.2.237.

[43]    D. Baxter *et al.*, "Recommended conventions for reporting results from direct dark matter searches," *Eur. Phys. J. C*, vol. 81, no. 10, p. 907, 2021. DOI: 10.1140/epjc/s10052-021-09655-y. arXiv: 2105.00599 [hep-ex].

[44]    D. S. Akerib *et al.*, "The LUX-ZEPLIN (LZ) Experiment," *Nucl. Instrum. Meth. A*, vol. 953, p. 163 047, 2020. DOI: 10.1016/j.nima.2019.163047. arXiv: 1910.09124 [physics.ins-det].

[45]    J. Aalbers *et al.*, "DARWIN: towards the ultimate dark matter detector," *JCAP*, vol. 11, p. 017, 2016. DOI: 10.1088/1475-7516/2016/11/017. arXiv: 1606.07001 [astro-ph.IM].

[46]    H. Zhang *et al.*, "Dark matter direct search sensitivity of the PandaX-4T experiment," *Sci. China Phys. Mech. Astron.*, vol. 62, no. 3, p. 31 011, 2019. DOI: 10.1007/s11433-018-9259-0. arXiv: 1806.02229 [physics.ins-det].

[47]    E. Aprile *et al.*, "Material radiopurity control in the XENONnT experiment," *Eur. Phys. J. C*, vol. 82, no. 7, p. 599, 2022. DOI: 10.1140/epjc/s10052-022-10345-6. arXiv: 2112.05629 [physics.ins-det].

[48]    B. Singh *et al.*, "Nuclear Data Sheets for $A = 218$," *Nucl. Data Sheets*, vol. 160, pp. 405–471, 2019. DOI: 10.1016/j.nds.2019.100524.

[49]    E. Aprile *et al.*, "Material radioassay and selection for the XENON1T dark matter experiment," *Eur. Phys. J. C*, vol. 77, no. 12, p. 890, 2017. DOI: 10.1140/epjc/s10052-017-5329-0. arXiv: 1705.01828 [physics.ins-det].

[50]    M. Murra, D. Schulte, C. Huhmann, and C. Weinheimer, "Design, construction and commissioning of a high-flow radon removal system for XENONnT," *Eur. Phys. J. C*, vol. 82, no. 12, p. 1104, 2022. DOI: 10.1140/epjc/s10052-022-11001-9. arXiv: 2205.11492 [physics.ins-det].

[51]    D. S. Akerib *et al.*, "The LUX-ZEPLIN (LZ) radioactivity and cleanliness control programs," *Eur. Phys. J. C*, vol. 80, no. 11, p. 1044, 2020. DOI: 10.1140/epjc/s10052-020-8420-x. arXiv: 2006.02506 [physics.ins-det].

[52] M. Arthurs, D. Q. Huang, C. Amarasinghe, E. Miller, and W. Lorenzon, "Performance Study of Charcoal-based Radon Reduction Systems for Ultraclean Rare Event Detectors," Sep. 2020. arXiv: 2009.06069 [physics.ins-det].

[53] K. Pushkin *et al.*, "Study of radon reduction in gases for rare event search experiments," *Nucl. Instrum. Meth. A*, vol. 903, pp. 267–276, 2018. DOI: 10.1016/j.nima.2018.06.076. arXiv: 1805.11306 [physics.ins-det].

[54] J. Tiffenberg *et al.*, "DAMIC: a novel dark matter experiment," in *33rd International Cosmic Ray Conference*, Oct. 2013, p. 1243. arXiv: 1310.6688 [astro-ph.IM].

[55] A. Aguilar-Arevalo *et al.*, "Measurement of the bulk radioactive contamination of detector-grade silicon with DAMIC at SNOLAB," *JINST*, vol. 16, no. 06, P06019, 2021. DOI: 10.1088/1748-0221/16/06/P06019. arXiv: 2011.12922 [physics.ins-det].

[56] E. Aprile *et al.*, "Simultaneous measurement of ionization and scintillation from nuclear recoils in liquid xenon as target for a dark matter experiment," *Phys. Rev. Lett.*, vol. 97, p. 081 302, 2006. DOI: 10.1103/PhysRevLett.97.081302. arXiv: astro-ph/0601552.

[57] F. Jörg, D. Cichon, G. Eurin, L. Hötzsch, T. Undagoitia Marrodán, and N. Rupp, "Characterization of alpha and beta interactions in liquid xenon," *Eur. Phys. J. C*, vol. 82, no. 4, p. 361, 2022. DOI: 10.1140/epjc/s10052-022-10259-3. arXiv: 2109.13735 [physics.ins-det].

[58] M. Shamsuzzoha Basunia, "Nuclear Data Sheets for A = 210," *Nucl. Data Sheets*, vol. 121, pp. 561–694, 2014. DOI: 10.1016/j.nds.2014.09.004.

[59] S. Singh, A. K. Jain, and J. K. Tuli, "Nuclear Data Sheets for A = 222," *Nucl. Data Sheets*, vol. 112, pp. 2851–2886, 2011. DOI: 10.1016/j.nds.2011.10.002.

[60] S. Zhu and E. A. McCutchan, "Nuclear Data Sheets for A=214," *Nucl. Data Sheets*, vol. 175, pp. 1–149, 2021. DOI: 10.1016/j.nds.2021.06.001.

[61] F. G. Kondev, "Nuclear Data Sheets for A = 206," *Nucl. Data Sheets*, vol. 109, pp. 1527–1654, 2008. DOI: 10.1016/j.nds.2008.05.002.

[62] E. Aprile *et al.*, "Results from a Calibration of XENON100 Using a Source of Dissolved Radon-220," *Phys. Rev. D*, vol. 95, no. 7, p. 072 008, 2017. DOI: 10.1103/PhysRevD.95.072008. arXiv: 1611.03585 [physics.ins-det].

[63]     D. C. Malling, "Measurement and Analysis of WIMP Detection Backgrounds, and Characterization and Performance of the Large Underground Xenon Dark Matter Search Experiment," Ph.D. dissertation, Brown U., 2014. DOI: 10.7301/Z0057D9F.

[64]     F. Pedregosa *et al.*, "Scikit-learn: Machine learning in python," *Journal of Machine Learning Research*, vol. 12, no. 85, pp. 2825–2830, 2011. [Online]. Available: http://jmlr.org/papers/v12/pedregosa11a.html.

[65]     D. Masson, "Novel Ideas and Techniques for Large Dark Matter Detectors," Ph.D. dissertation, Purdue U., May 2018.

[66]     E. Aprile *et al.*, "$^{222}$Rn emanation measurements for the XENON1T experiment," *Eur. Phys. J. C*, vol. 81, no. 4, p. 337, 2021. DOI: 10.1140/epjc/s10052-020-08777-z. arXiv: 2009.13981 [physics.ins-det].

[67]     G. Ahlers *et al.*, "Aspect ratio dependence of heat transfer in a cylindrical rayleigh-bénard cell," *Phys. Rev. Lett.*, vol. 128, p. 084 501, 8 Feb. 2022. DOI: 10.1103/PhysRevLett.128.084501. [Online]. Available: https://link.aps.org/doi/10.1103/PhysRevLett.128.084501.

[68]     J. Ye, "Searches for WIMPs and axions with the XENON1T experiment," Ph.D. dissertation, University of California, San Diego, Jan. 2020.

[69]     J. B. S. HALDANE, "Note on the median of a multivariate distribution," *Biometrika*, vol. 35, no. 3-4, pp. 414–417, Dec. 1948, ISSN: 0006-3444. DOI: 10.1093/biomet/35.3-4.414. eprint: https://academic.oup.com/biomet/article-pdf/35/3-4/414/785927/35-3-4-414.pdf. [Online]. Available: https://doi.org/10.1093/biomet/35.3-4.414.

[70]     H. P. Lopuhaa and P. J. Rousseeuw, "Breakdown Points of Affine Equivariant Estimators of Multivariate Location and Covariance Matrices," *The Annals of Statistics*, vol. 19, no. 1, pp. 229–248, 1991. DOI: 10.1214/aos/1176347978. [Online]. Available: https://doi.org/10.1214/aos/1176347978.

[71]     J. B. Albert *et al.*, "Measurements of the ion fraction and mobility of $\alpha$- and $\beta$-decay products in liquid xenon using the EXO-200 detector," *Phys. Rev. C*, vol. 92, no. 4, p. 045 504, 2015. DOI: 10.1103/PhysRevC.92.045504. arXiv: 1506.00317 [nucl-ex].

[72]     J. Aalbers *et al.*, "Background Determination for the LUX-ZEPLIN (LZ) Dark Matter Experiment," Nov. 2022. arXiv: 2211.17120 [hep-ex].

[73]    M. Auger *et al.*, "The EXO-200 detector, part I: Detector design and construction," *JINST*, vol. 7, P05010, 2012. DOI: 10.1088/1748-0221/7/05/P05010. arXiv: 1202.2192 [physics.ins-det].

[74]    R. Bridson, J. Houriham, and M. Nordenstam, "Curl-noise for procedural fluid flow," *ACM Trans. Graph.*, vol. 26, no. 3, 46–es, Jul. 2007, ISSN: 0730-0301. DOI: 10.1145/1276377.1276435. [Online]. Available: https://doi.org/10.1145/1276377.1276435.

[75]    M. Ester, H.-P. Kriegel, J. Sander, and X. Xu, "A density-based algorithm for discovering clusters in large spatial databases with noise," in *Proceedings of the Second International Conference on Knowledge Discovery and Data Mining*, ser. KDD'96, Portland, Oregon: AAAI Press, 1996, pp. 226–231.

[76]    G. Cowan, K. Cranmer, E. Gross, and O. Vitells, "Asymptotic formulae for likelihood-based tests of new physics," *Eur. Phys. J. C*, vol. 71, p. 1554, 2011, [Erratum: Eur.Phys.J.C 73, 2501 (2013)]. DOI: 10.1140/epjc/s10052-011-1554-0. arXiv: 1007.1727 [physics.data-an].

[77]    E. Aprile *et al.*, "Emission of single and few electrons in XENON1T and limits on light dark matter," *Phys. Rev. D*, vol. 106, no. 2, p. 022 001, 2022. DOI: 10.1103/PhysRevD.106.022001. arXiv: 2112.12116 [hep-ex].

[78]    M. Speetjens, G. Metcalfe, and M. Rudman, "Lagrangian transport and chaotic advection in three-dimensional laminar flows," *Applied Mechanics Reviews*, vol. 73, no. 3, 2021.

[79]    J. Taylor, "Classical mechanics," in University Science Books, 2005, ch. 12, ISBN: 9781891389221.

[80]    S. Bruenner *et al.*, "Radon daughter removal from PTFE surfaces and its application in liquid xenon detectors," *Eur. Phys. J. C*, vol. 81, no. 4, p. 343, 2021. DOI: 10.1140/epjc/s10052-021-09047-2. arXiv: 2009.08828 [physics.ins-det].

[81]    E. Aprile *et al.*, "Search for New Physics in Electronic Recoil Data from XENONnT," *Phys. Rev. Lett.*, vol. 129, no. 16, p. 161 805, 2022. DOI: 10.1103/PhysRevLett.129.161805. arXiv: 2207.11330 [hep-ex].

[82]    A. Einstein, *Investigations on the theory of the Brownian movement* (Dover Books on Physics). Mineola, NY: Dover Publications, Jun. 1956, ISBN: 9780486603049.

[83]     A. D. ( D. Polianin, *Handbook of linear partial differential equations for engineers and scientists*, Second edition. Boca Raton: Chapman & Hall/CRC, 2002, ISBN: 9786610517145.

[84]     R. Richert, L. Pautmeier, and H. Bässler, "Diffusion and drift of charge carriers in a random potential: Deviation from einstein's law," *Phys. Rev. Lett.*, vol. 63, pp. 547–550, 5 Jul. 1989. DOI: 10.1103/PhysRevLett.63.547. [Online]. Available: https://link.aps.org/doi/10.1103/PhysRevLett.63.547.

[85]     D. S. Akerib *et al.*, "Projected sensitivity of the LUX-ZEPLIN experiment to the $0\nu\beta\beta$ decay of $^{136}Xe$," *Phys. Rev. C*, vol. 102, no. 1, p. 014 602, 2020. DOI: 10.1103/PhysRevC.102.014602. arXiv: 1912.04248 [nucl-ex].

[86]     E. Browne and J. K. Tuli, "Nuclear Data Sheets for A = 137," *Nucl. Data Sheets*, vol. 108, pp. 2173–2318, 2007. DOI: 10.1016/j.nds.2007.09.002.

[87]     M. Berger *et al.* "Xcom: Photon cross section database (version 1.5)." (2010), [Online]. Available: http://physics.nist.gov/xcom.

[88]     C. S. Amarasinghe *et al.*, "Feasibility study to use neutron capture for an ultralow energy nuclear-recoil calibration in liquid xenon," *Phys. Rev. D*, vol. 106, no. 3, p. 032 007, 2022. DOI: 10.1103/PhysRevD.106.032007. arXiv: 2204.03109 [physics.ins-det].

[89]     J. B. Albert *et al.*, "Improved measurement of the $2\nu\beta\beta$ half-life of $^{136}$Xe with the EXO-200 detector," *Phys. Rev. C*, vol. 89, no. 1, p. 015 502, 2014. DOI: 10.1103/PhysRevC.89.015502. arXiv: 1306.6106 [nucl-ex].

[90]     C. A. J. O'Hare, "New Definition of the Neutrino Floor for Direct Dark Matter Searches," *Phys. Rev. Lett.*, vol. 127, no. 25, p. 251 802, 2021. DOI: 10.1103/PhysRevLett.127.251802. arXiv: 2109.03116 [hep-ph].

[91]     C. A. J. O'Hare, "Can we overcome the neutrino floor at high masses?" *Phys. Rev. D*, vol. 102, no. 6, p. 063 024, 2020. DOI: 10.1103/PhysRevD.102.063024. arXiv: 2002.07499 [astro-ph.CO].

[92]     M. Wurm, "Solar Neutrino Spectroscopy," *Phys. Rept.*, vol. 685, pp. 1–52, 2017. DOI: 10.1016/j.physrep.2017.04.002. arXiv: 1704.06331 [hep-ex].

[93]     E. Aprile *et al.*, "Search for Coherent Elastic Scattering of Solar $^8$B Neutrinos in the XENON1T Dark Matter Experiment," *Phys. Rev. Lett.*, vol. 126, p. 091 301, 2021. DOI: 10.1103/PhysRevLett.126.091301. arXiv: 2012.02846 [hep-ex].

[94] J. A. Formaggio and G. P. Zeller, "From eV to EeV: Neutrino Cross Sections Across Energy Scales," *Rev. Mod. Phys.*, vol. 84, pp. 1307–1341, 2012. DOI: 10.1103/RevMod Phys.84.1307. arXiv: 1305.7513 [hep-ex].

[95] M. Agostini *et al.*, "Improved measurement of $^8$B solar neutrinos with $1.5kt\mathring{u}y$ of Borexino exposure," *Phys. Rev. D*, vol. 101, no. 6, p. 062 001, 2020. DOI: 10.1103/ PhysRevD.101.062001. arXiv: 1709.00756 [hep-ex].

[96] D. Z. Freedman, "Coherent Neutrino Nucleus Scattering as a Probe of the Weak Neutral Current," *Phys. Rev. D*, vol. 9, pp. 1389–1392, 1974. DOI: 10.1103/PhysRevD.9.1389.

[97] D. Akimov *et al.*, "Observation of Coherent Elastic Neutrino-Nucleus Scattering," *Science*, vol. 357, no. 6356, pp. 1123–1126, 2017. DOI: 10.1126/science.aao0990. arXiv: 1708.01294 [nucl-ex].

[98] D. Aristizabal Sierra, J. Liao, and D. Marfatia, "Impact of form factor uncertainties on interpretations of coherent elastic neutrino-nucleus scattering data," *JHEP*, vol. 06, p. 141, 2019. DOI: 10.1007/JHEP06(2019)141. arXiv: 1902.07398 [hep-ph].

[99] L. E. Strigari, "Neutrino Coherent Scattering Rates at Direct Dark Matter Detectors," *New J. Phys.*, vol. 11, p. 105 011, 2009. DOI: 10.1088/1367-2630/11/10/105011. arXiv: 0903.3630 [astro-ph.CO].

[100] J. Aalbers, B. Pelssers, and K. D. Morå, *Jelleaalbers/wimprates: V0.3.1*, version v0.3.1, Nov. 2019. DOI: 10.5281/zenodo.3551727. [Online]. Available: https://doi.org/10.5281/ zenodo.3551727.

[101] J. I. Collar, "Applications of an $^{88}Y/Be$ photo-neutron calibration source to Dark Matter and Neutrino Experiments," *Phys. Rev. Lett.*, vol. 110, no. 21, p. 211 101, 2013. DOI: 10.1103/PhysRevLett.110.211101. arXiv: 1303.2686 [physics.ins-det].

[102] M. F. Albakry *et al.*, "Ionization yield measurement in a germanium CDMSlite detector using photo-neutron sources," *Phys. Rev. D*, vol. 105, no. 12, p. 122 002, 2022. DOI: 10.1103/PhysRevD.105.122002. arXiv: 2202.07043 [physics.ins-det].

[103] J. B. Albert *et al.*, "Measurement of the Drift Velocity and Transverse Diffusion of Electrons in Liquid Xenon with the EXO-200 Detector," *Phys. Rev. C*, vol. 95, no. 2, p. 025 502, 2017. DOI: 10.1103/PhysRevC.95.025502. arXiv: 1609.04467 [physics.ins-det].

[104] S. Agostinelli *et al.*, "GEANT4–a simulation toolkit," *Nucl. Instrum. Meth. A*, vol. 506, pp. 250–303, 2003. DOI: 10.1016/S0168-9002(03)01368-8.

[105] E. Aprile *et al.*, "Physics reach of the XENON1T dark matter experiment," *JCAP*, vol. 04, p. 027, 2016. DOI: 10.1088/1475-7516/2016/04/027. arXiv: 1512.07501 [physics.ins-det].

[106] B. Hamermesh, M. Hamermesh, and A. Wattenberg, "The angular distribution of the photo-neutrons from beryllium," *Phys. Rev.*, vol. 76, pp. 611–613, 5 Sep. 1949. DOI: 10.1103/PhysRev.76.611. [Online]. Available: https://link.aps.org/doi/10.1103/PhysRev.76.611.

[107] C. Wittweg, "Second-Order Weak Decays in XENON1T and Future Xenon Time Projection Chambers," Ph.D. dissertation, WWU Münster, 2021.

[108] E. Aprile *et al.*, "The Triggerless Data Acquisition System of the XENONnT Experiment," Dec. 2022. arXiv: 2212.11032 [physics.ins-det].

[109] W. Adam *et al.*, "The CMS Phase-1 Pixel Detector Upgrade," *JINST*, vol. 16, no. 02, P02027, 2021. DOI: 10.1088/1748-0221/16/02/P02027. arXiv: 2012.14304 [physics.ins-det].

[110] G. Aad *et al.*, "The ATLAS Fast TracKer system," *JINST*, vol. 16, P07006, 2021. DOI: 10.1088/1748-0221/16/07/P07006. arXiv: 2101.05078 [physics.ins-det].

[111] I. Tomalin *et al.*, "An FPGA based track finder for the L1 trigger of the CMS experiment at the High Luminosity LHC," *JINST*, vol. 12, P12019, 2017. DOI: 10.1088/1748-0221/12/12/P12019.

[112] A. H. Nitz, T. Dent, T. Dal Canton, S. Fairhurst, and D. A. Brown, "Detecting binary compact-object mergers with gravitational waves: Understanding and Improving the sensitivity of the PyCBC search," *Astrophys. J.*, vol. 849, no. 2, p. 118, 2017. DOI: 10.3847/1538-4357/aa8f50. arXiv: 1705.01513 [gr-qc].

[113] S. Al Kharusi *et al.*, "SNEWS 2.0: a next-generation supernova early warning system for multi-messenger astronomy," *New J. Phys.*, vol. 23, no. 3, p. 031 201, 2021. DOI: 10.1088/1367-2630/abde33. arXiv: 2011.00035 [astro-ph.HE].

[114] A. E. Bayer and U. Seljak, "The look-elsewhere effect from a unified Bayesian and frequentist perspective," *JCAP*, vol. 10, p. 009, 2020. DOI: 10.1088/1475-7516/2020/10/009. arXiv: 2007.13821 [physics.data-an].

[115] S. Sakon *et al.*, "Template bank for compact binary mergers in the fourth observing run of Advanced LIGO, Advanced Virgo, and KAGRA," Nov. 2022. arXiv: 2211.16674 [gr-qc].

[116] R. Agnese *et al.*, "Low-mass dark matter search with CDMSlite," *Phys. Rev. D*, vol. 97, no. 2, p. 022 002, 2018. DOI: 10.1103/PhysRevD.97.022002. arXiv: 1707.01632 [astro-ph.CO].

[117] S. Helgason, *The Radon Transform* (Progress in Mathematics), en, 2nd ed. Secaucus, NJ: Birkhauser Boston, Aug. 1999.

[118] P. Whittle, *Probability via expectation* (Springer texts in statistics), en, 4th ed. New York, NY: Springer, Dec. 2012.

[119] M. Vetterli, J. Kovacevic, and V. K. Goyal, *Foundations of Signal Processing*, Hardcover. Cambridge University Press, Oct. 20, 2014, p. 738, ISBN: 978-1107038608.

[120] J. Hofer *et al.*, "High-Q magnetic levitation and control of superconducting microspheres at millikelvin temperatures," Nov. 2022. arXiv: 2211.06289 [quant-ph].

[121] S. Ghosh, D. Carney, P. Shawhan, and J. M. Taylor, "Backaction-evading impulse measurement with mechanical quantum sensors," *Phys. Rev. A*, vol. 102, no. 2, p. 023 525, 2020. DOI: 10.1103/PhysRevA.102.023525. arXiv: 1910.11892 [quant-ph].

[122] C. M. Caves, K. S. Thorne, R. W. P. Drever, V. D. Sandberg, and M. Zimmermann, "ON THE MEASUREMENT OF A WEAK CLASSICAL FORCE COUPLED TO A QUANTUM MECHANICAL OSCILLATOR. I. ISSUES OF PRINCIPLE," *Rev. Mod. Phys.*, vol. 52, pp. 341–392, 1980. DOI: 10.1103/RevModPhys.52.341.

[123] A. A. Clerk, "Quantum-limited position detection and amplification: A linear response perspective," *Physical Review B*, vol. 70, no. 24, Dec. 2004. DOI: 10.1103/physrevb.70.245306. [Online]. Available: https://doi.org/10.1103%2Fphysrevb.70.245306.

[124] W. M. Haynes, Ed., *CRC handbook of chemistry and physics, 92nd edition*, 92nd ed. Boca Raton, FL: CRC Press, Dec. 2011.

[125] D. Carney, A. Hook, Z. Liu, J. M. Taylor, and Y. Zhao, "Ultralight dark matter detection with mechanical quantum sensors," *New J. Phys.*, vol. 23, no. 2, p. 023 041, 2021. DOI: 10.1088/1367-2630/abd9e7. arXiv: 1908.04797 [hep-ph].

[126] M. C. Digman, C. V. Cappiello, J. F. Beacom, C. M. Hirata, and A. H. G. Peter, "Not as big as a barn: Upper bounds on dark matter-nucleus cross sections," *Phys. Rev. D*, vol. 100, no. 6, p. 063 013, 2019, [Erratum: Phys.Rev.D 106, 089902 (2022)]. DOI: 10.1103/PhysRevD.100.063013. arXiv: 1907.10618 [hep-ph].

[127] M. Clark *et al.*, "Direct Detection Limits on Heavy Dark Matter," *Phys. Rev. D*, vol. 102, no. 12, p. 123 026, 2020. DOI: 10.1103/PhysRevD.102.123026. arXiv: 2009.07909 [hep-ph].

[128] R. Harnik, Z. Liu, and O. Palamara, "Millicharged Particles in Liquid Argon Neutrino Experiments," *JHEP*, vol. 07, p. 170, 2019. DOI: 10.1007/JHEP07(2019)170. arXiv: 1902.03246 [hep-ph].

[129] S. A. Usman *et al.*, "The PyCBC search for gravitational waves from compact binary coalescence," *Class. Quant. Grav.*, vol. 33, no. 21, p. 215 004, 2016. DOI: 10.1088/0264-9381/33/21/215004. arXiv: 1508.02357 [gr-qc].

[130] X. Wang, Y. Jin, S. Schmitt, and M. Olhofer, "Recent advances in bayesian optimization," *ACM Computing Surveys*, 2022. arXiv: 2206.03301 [cs.LG].

[131] J. Buchner, "Nested sampling methods," 2021. arXiv: 2101.09675 [stat.CO].

[132] J. Buchner, "UltraNest - a robust, general purpose Bayesian inference engine," *The Journal of Open Source Software*, vol. 6, no. 60, 3001, p. 3001, Apr. 2021. DOI: 10.21105/joss.03001. arXiv: 2101.09604 [stat.CO].

[133] G. Ashton *et al.*, "Nested sampling for physical scientists," *Nature*, vol. 2, 2022. DOI: 10.1038/s43586-022-00121-x. arXiv: 2205.15570 [stat.CO].

[134] A. W. van der Vaart, *Cambridge series in statistical and probabilistic mathematics: Asymptotic statistics series number 3*, en. Cambridge, England: Cambridge University Press, Jun. 2000.

[135] D. Foreman-Mackey, "Corner.py: Scatterplot matrices in python," *The Journal of Open Source Software*, vol. 1, no. 2, p. 24, Jun. 2016. DOI: 10.21105/joss.00024. [Online]. Available: https://doi.org/10.21105/joss.00024.

[136] P. F. De Salas, S. Gariazzo, O. Mena, C. A. Ternes, and M. Tórtola, "Neutrino Mass Ordering from Oscillations and Beyond: 2018 Status and Future Prospects," *Front. Astron. Space Sci.*, vol. 5, p. 36, 2018. DOI: 10.3389/fspas.2018.00036. arXiv: 1806.11051 [hep-ph].

[137]  R. M. Neal, "Slice sampling," *The Annals of Statistics*, vol. 31(3), pp. 705–767, 2003. arXiv: physics/0009028 [physics.data-an].

[138]  M. Betancourt and M. A. Girolami, "Hamiltonian monte carlo for hierarchical models," 2013. arXiv: 1312.0906 [stat.ME].

[139]  C. Rover, R. Meyer, and N. Christensen, "Modelling coloured residual noise in gravitational-wave signal processing," *Class. Quant. Grav.*, vol. 28, p. 015 010, 2011. DOI: 10.1088/0264-9381/28/1/015010. arXiv: 0804.3853 [stat.ME].

[140]  J. Manley, M. D. Chowdhury, D. Grin, S. Singh, and D. J. Wilson, "Searching for vector dark matter with an optomechanical accelerometer," *Phys. Rev. Lett.*, vol. 126, no. 6, p. 061 301, 2021. DOI: 10.1103/PhysRevLett.126.061301. arXiv: 2007.04899 [quant-ph].

[141]  N. Choudhuri, S. Ghosal, and A. Roy, "Contiguity of the Whittle measure for a Gaussian time series," *Biometrika*, vol. 91, no. 1, pp. 211–218, Mar. 2004, ISSN: 0006-3444. DOI: 10.1093/biomet/91.1.211. eprint: https://academic.oup.com/biomet/article-pdf/91/1/211/582804/910211.pdf. [Online]. Available: https://doi.org/10.1093/biomet/91.1.211.

[142]  P. J. Brockwell and R. A. Davis, *Time series: Theory and methods* (Springer Series in Statistics), en, 2nd ed. New York, NY: Springer, May 2009.

[143]  C. Walck, *Hand-book on statistical distributions for experimentalists*. Dec. 1996.

[144]  S. Algeri, J. Aalbers, K. Dundas Morå, and J. Conrad, "Searching for new phenomena with profile likelihood ratio tests," *Nature Rev. Phys.*, vol. 2, no. 5, pp. 245–252, 2020. DOI: 10.1038/s42254-020-0169-5. arXiv: 1911.10237 [physics.data-an].

[145]  J. W. Foster, N. L. Rodd, and B. R. Safdi, "Revealing the Dark Matter Halo with Axion Direct Detection," *Phys. Rev. D*, vol. 97, no. 12, p. 123 006, 2018. DOI: 10.1103/PhysRevD.97.123006. arXiv: 1711.10489 [astro-ph.CO].

[146]  E. Gross and O. Vitells, "Trial factors for the look elsewhere effect in high energy physics," *Eur. Phys. J. C*, vol. 70, pp. 525–530, 2010. DOI: 10.1140/epjc/s10052-010-1470-8. arXiv: 1005.1891 [physics.data-an].

[147]  G. Carleo *et al.*, "Machine learning and the physical sciences," *Rev. Mod. Phys.*, vol. 91, no. 4, p. 045 002, 2019. DOI: 10.1103/RevModPhys.91.045002. arXiv: 1903.10563 [physics.comp-ph].

[148] K. J. Worsley, A. C. Evans, S. Marrett, and P. Neelin, "A three-dimensional statistical analysis for cbf activation studies in human brain," *Journal of Cerebral Blood Flow & Metabolism*, vol. 12, no. 6, pp. 900–918, 1992, PMID: 1400644. DOI: 10.1038/jcbfm.1992.127. eprint: https://doi.org/10.1038/jcbfm.1992.127. [Online]. Available: https://doi.org/10.1038/jcbfm.1992.127.

[149] J. M. Bardeen, J. R. Bond, N. Kaiser, and A. S. Szalay, "The Statistics of Peaks of Gaussian Random Fields," *Astrophys. J.*, vol. 304, pp. 15–61, 1986. DOI: 10.1086/164143.

[150] O. Vitells and E. Gross, "Estimating the significance of a signal in a multi-dimensional search," *Astroparticle Physics*, vol. 35, no. 5, pp. 230–234, Dec. 2011. DOI: 10.1016/j.astropartphys.2011.08.005. arXiv: 1105.4355 [astro-ph.IM].

[151] V. Ananiev and A. L. Read, "Gaussian Process-based calculation of look-elsewhere trials factor," Jun. 2022. arXiv: 2206.12328 [stat.ME].

[152] R. J. Adler, J. E. Taylor, *et al.*, *Random fields and geometry*. Springer, 2007, vol. 80.

[153] P. Billingsley, *Probability and Measure (Wiley Series in Probability and Statistics Book 938)*, Kindle Edition. Wiley, Jan. 20, 2012, p. 963. [Online]. Available: https://lead.to/amazon/com/?op=bt&la=en&cu=usd&key=B00711B7AS.

[154] I. Tyurin, "New estimates of the convergence rate in the Lyapunov theorem," *arXiv e-prints*, arXiv:0912.0726, arXiv:0912.0726, Dec. 2009. DOI: 10.48550/arXiv.0912.0726. arXiv: 0912.0726 [math.PR].

[155] Y. Liu, J. Li, S. Sun, and B. Yu, "Advances in gaussian random field generation: A review," *Computational Geosciences*, vol. 23, pp. 1011–1047, 2019.

[156] E. T. Jaynes, *Probability Theory: The Logic of Science*, Kindle Edition, G. L. Bretthorst, Ed. Cambridge University Press, Apr. 10, 2003, p. 758. [Online]. Available: https://lead.to/amazon/com/?op=bt&la=en&cu=usd&key=B00AKE1Q40.

[157] A. Aguilar-Arevalo *et al.*, "Characterization of the background spectrum in DAMIC at SNOLAB," *Phys. Rev. D*, vol. 105, no. 6, p. 062 003, 2022. DOI: 10.1103/PhysRevD.105.062003. arXiv: 2110.13133 [hep-ex].

[158] I. Andreoni *et al.*, "Probing the extragalactic fast transient sky at minute time-scales with DECam," *Mon. Not. Roy. Astron. Soc.*, vol. 491, no. 4, pp. 5852–5866, 2020. DOI: 10.1093/mnras/stz3381. arXiv: 1903.11083 [astro-ph.HE].

[159] K. M. Hambleton *et al.*, "Rubin Observatory LSST Transients and Variable Stars Roadmap," Aug. 2022. arXiv: 2208.04499 [astro-ph.IM].

[160] J. P. Nolan, *Univariate Stable Distributions: Models for Heavy Tailed Data (Springer Series in Operations Research and Financial Engineering)*, Hardcover. Springer, Sep. 13, 2020, p. 348, ISBN: 978-3030529147. [Online]. Available: https://lead.to/amazon/com/?op=bt&la=en&cu=usd&key=3030529142.

[161] D. A. Abraham, "Detecting signals with known form: Matched filters," in *Underwater Acoustic Signal Processing: Modeling, Detection, and Estimation.* Cham: Springer International Publishing, 2019, pp. 457–619, ISBN: 978-3-319-92983-5. DOI: 10.1007/978-3-319-92983-5_8. [Online]. Available: https://doi.org/10.1007/978-3-319-92983-5_8.

[162] E. Petroff, J. W. T. Hessels, and D. R. Lorimer, "Fast radio bursts at the dawn of the 2020s," *Astron. Astrophys. Rev.*, vol. 30, no. 1, p. 2, 2022. DOI: 10.1007/s00159-022-00139-w. arXiv: 2107.10113 [astro-ph.HE].

[163] L. Lyons, "Discovering the Significance of 5 sigma," Oct. 2013. arXiv: 1310.1284 [physics.data-an].

[164] R. J. Barlow, "Practical statistics for particle physics," *CERN Yellow Rep. School Proc.*, vol. 5, M. Mulders and J. Trân Thanh Vân, Eds., pp. 149–197, 2020. DOI: 10.23730/CYRSP-2021-005.197. arXiv: 1905.12362 [physics.data-an].

[165] I. Asimov, *In joy still felt.* Doubleday Books, Jan. 1980.